

DEPARTMENT OF PHYSICS
UNIVERSITY OF JYVÄSKYLÄ
RESEARCH REPORT No. 13/2018

**EXPERIMENTAL STUDIES ON CARBON
NANOTUBES AND GRAPHENE
FUNCTIONALIZED VIA PHYSICAL
ADSORPTION WITH CELLULOSE AND
AVIDIN.**

**BY
DONGKAI SHAO**

Academic Dissertation
for the Degree of
Doctor of Philosophy

*To be presented, by permission of the
Faculty of Mathematics and Science
of the University of Jyväskylä,
for public examination in Auditorium FYS-1 of the
University of Jyväskylä on December 18, 2018
at 12 o'clock*

Jyväskylä, Finland
Dec 2018

Preface

The work reviewed in this thesis has been carried out during the years 2014-2018 at the Department of Physics at the University of Jyväskylä.

First of all, I would like to give my special thanks to my supervisor Professor Markus Ahlskog for guidance throughout the work. I have really enjoyed this study and working period as a student, an apprentice, an employee, a co-author, and a friend.

I would also like to thank all the collaborating people who give me really strong support for my researches. Dr.Jussi Toppari, Dr.Vesa Hytönen, Dr.Kosti Tapio, Dr.Sanna Auer are specially thanked for the chimeric-avidin related and DNA actuator works. Prof.Jorma Virtanen, Dr. Alexander Volodin, Dr.James Lloyd-Hughes, Mr.Hannu Pasanen, Mr.Zhuoran Geng, Dr. Peerapong Yotprayoonska, Mr. Ville Saunajoki, Mr.Veijo Kangas, Dr.Maria Burdanova, Mr.Connor Mosley et al for the carbon nanotube / hemicellulose work.

In Nanoscience Center, I found I could always get really useful help from researchers with different educational background. I would like to thank Dr.Matti Hokkanen, Dr.Olli Herranen, Dr. Andreas Johansson, Dr.Davie Mtsuko, Dr.Kimmo Kinnunen, Mr.Tarmo Suppula, Dr.Satu Mustalahti, Dr.Boxuan Shen, Dr.Yaolan Tian, Dr.Xi Chen et al for their kindly help and useful discussions. Mr. Joonas Jokivartio helped me with this phd thesis's language checking.

Finally, I would like to share my happiness and delights with all my family members for your encouragement, support and tolerance.

Financial support from the Academy of Finland is gratefully acknowledged.

Jyväskylä, 2018

Dongkai Shao

Acronyms

CNT	Carbon nanotube
MWNT	Multiwalled carbon nanotube
DWNT	Doublewalled carbon nanotube
SWNT	Singlewalled carbon nanotube
CNT/hc	Carbon nanotube and hemicellulose complex
b-AuNP	biotinylated gold nanoparticle
Chi-AVD	chimeric avidin
HOPG	Highly oriented pyrolytic graphite
DCE	1,2- dichloroethane
AFM	Atomic force microscope
SEM	Scanning electron microscope
THz-TDS	Terahertz time-domain spectroscopy
KPFM	Kelvin probe force microscope
BSe	Backscattering electrons
SE	Secondary electrons

Abstract

Dongkai, Shao

Experimental studies of nanocarbon hybrids with hemicellulose and avidin: Structure, conductivity and optical properties

Jyväskylä: University of Jyväskylä, 2018.

(Research report/Department of Physics, University of Jyväskylä,

ISSN 978-951-39-7623-1 (paper version)

ISBN 978-951-39-7624-8 (electronic version)

diss.

In this Thesis I have experimentally studied structural, electronic, and optical properties of hybrids of nanocarbon materials, carbon nanotubes (CNT) and graphene, and certain biomacromolecules. The latter are especially xylan, a type of hemicellulose, and avidin, an important protein.

Complexes of CNT with hemicellulose are attractive because the hybrid material is soluble in water. The conductive transport properties of thin films of CNT/hemicellulose have been systematically studied with different experimental tools. These are low temperature DC conduction measurements, Kelvin probe microscopy, and optical conductivity measurements at terahertz frequencies. The results clearly indicate that the CNT/CNT junctions rather than the defects along the CNTs play the key role in the CNT/hc transport mechanism of the thin films. Furthermore, we tested one application of the CNT/hc thin films as transparent conductive thin film (TCF), which combine high conductivity with low adsorption in the visible light region. The results are quite close to the best pure CNT thin films, but still well below the figure of merit of the indium tin oxide which is the most widely used TCF material.

The other major research topic in the Thesis is on structural properties of proteins physically adsorbed on carbon nanomaterials. We have experimented with physical adsorption of chimeric avidin on different surfaces, such as silicon, highly oriented pyrolytic graphite, graphene, and suspended multiwalled CNTs. The deposition results are dramatically different between silicon and nanocarbon materials. We observed that the topography difference between graphite (or graphene) and CNTs have significant effect on chi-avidin deposition. Furthermore, we investigated

the functionality of avidin after surface adsorption, with respect to its excellent binding capability in the solution phase of biotin.

Keywords carbon nanotube, graphene, surface functionalization, avidin, hemicellulose, electronic property

Author's address	Dongkai Shao Nanoscience Center, Department of Physics University of Jyväskylä Jyväskylä, Finland
Supervisor	Professor Markus Ahlskog Department of Physics University of Jyväskylä Jyväskylä, Finland
Reviewers	Dr. Ville P. Jokinen Academy researcher Department of Chemistry and Materials science Aalto University Espoo, Finland Dr. Mark Baxendale Reader in nanotechnology Centre for Condensed Matter and Materials Physics School of Physics and Astronomy Queen Mary University of London London, United Kingdom
Opponent	Professor. Patrick Wagner Dept. of Physics and Astronomy Katholieke Universiteit Leuven Leuven, Belgium

List of Publications

The main results of this thesis have been reported in the following articles:

- A.I** D,SHAO. P,YOTPRAYOONSAK. V,SAUNAJOKI. M,AHLSKOG. J,VIRTANEN. V,KANGAS. A,VOLODIN. C,HAESENDONCK. M,BURDANOVA. C,D,W.MOSLEY AND J,LLOYD-HUGHES., *Conduction properties of thin films from a water soluble carbon nanotube/hemicellulose complex*. *Nanotechnology*.**29** (2018) 145203-145212.
- A.II** D,SHAO. K,TAPIO. S,AUER. J,TOPPARI. V,HYTÖNEN AND M,AHLSKOG, *Surface characteristics control the attachment and functionality of (chimeric) avidin*. *Langmuir* (In press) [43].
- A.III** K,TAPIO. D,SHAO. S,AUER. J,TUPPURAINEN, M,AHLSKOG. V,HYTÖNEN AND J,TOPPARI., *DNA-nanoparticle actuator enabling optical monitoring of nanoscale movements induced by electric field*. *Nanoscale*.**10**(2018) 19297-19309.

Author's contribution

This thesis is a compilation of three journal articles, as well as three additional written chapters.

In **A.I**, the author did sample fabrication of CNT/hc thin films, electrical transport measurements and data analysis, and participated in the writing process.

In **A.II**, the author conducted all the experiments with sample fabrication, imaging and data analysis, with some support from Dr. Kosti Tapio, and wrote the first draft of the manuscript. Avidin synthesis was done in the group of Prof. Vesa Hytönen.

In **A.III**, the author contributed to the work of Dr.Kosti Tapio on nanoparticle actuator design and fabrication processes. This included concept proof experiments with dynamic light scattering, IR spectrum measurements, AFM,and SEM experiments, which proved that chi-avidin and biotin-AuNPs linkage can work on a silicon surface. The author also participated in building high electric fields with parallel

capacitor in water, up to 10^7 V/m.

Other work to which the author has contributed:

- B.I** M, HOKKANEN. S, LAUTALA. D, SHAO. T, TURPEINEN. J, KOIVISTOINEN. M, AHLKOG., *On-Chip purification via liquid immersion of arc-discharge synthesized multiwalled carbon nanotubes*. *Applied Physics A*.**122** (2016) 634.

Contents

Preface	1
Abstract	5
List of Publications	9
1 Introduction	9
2 Introduction to the carbon nanotube	13
2.1 Synthesis methods	13
2.2 CNT band structure	14
2.3 Transport properties of a carbon nanotube	17
3 Carbon nanotube/graphene and their complexes with macromolecules	19
3.1 Bio-macromolecules	19
3.1.1 Proteins	19
3.1.2 Cellulose and hemicellulose	23
3.2 Macromolecules on CNT	24
3.2.1 Covalent functionalization of carbon nanotube	25
3.2.2 Non-covalent functionalization of CNT	26
3.2.3 Previous works of avidin adsorption on a surface	27
4 Experimental facilities	29
4.1 Nanofabrication facilities	29
4.2 Modern microscopes	31
4.3 Cryogenics	34
5 Electronic measurement of a single CNT device	37
5.1 Single carbon nanotube backgated FET fabrication	37
5.2 Conductivity measurements setup	40
5.3 Conductivity measurement at different temperatures	41
6 Electronic and optical properties of thin films of carbon nanotube/hemicellulose complex	45
6.1 Preparation of CNT/hemicellulose dispersion and its property	45
6.2 CNT/hc thin film fabrications	47
6.3 Experiment	50
6.3.1 DC measurement: Temperature dependence	50
6.3.2 Kelvin probe atomic force microscope measurement	51
6.3.3 Terahertz conductivity measurement	51

6.3.4	Optical measurement: transmittance from near UV to far IR	52
6.4	Results	53
6.4.1	DC measurement	53
6.4.2	Kelvin probe atomic force microscopy	54
6.4.3	Terahertz conductivity measurement	55
6.4.4	Transmittance of thin film from UV to far IR	56
6.5	Discussions	57
7	Physical and chemical adsorption of proteins to surface	63
7.1	Materials and substrate preparations	63
7.2	Physical adsorption of chi-avidin on different surfaces	65
7.2.1	Physical adsorption of chi-avidins on hydrophilic and hydrophobic silicon surface	65
7.2.2	Chi-avidin physical adsorption on HOPG and graphene surface	67
7.2.3	Chi-avidin physical adsorption on suspended carbon nanotube.	69
7.3	The functionality of chi-avidin after physical adsorption on the surfaces	72
7.3.1	The functionality of chi-avidin on HOPG or graphene	72
7.3.2	Chi-avidin on HOPG with cross-linker	72
7.4	Discussion and conclusions	73
8	Towards a nanoparticle actuator	77
8.1	Concept proof	78
8.1.1	Chi-avidin and b-AuNPs functionality in buffer	78
8.1.2	Chi-avidin/b-AuNPs deposition from buffer	80
8.1.3	The functionality of chi-avidin on silicon surface	81
8.2	Building blocks of the DNA nanoparticle actuator and assembly	83
8.2.1	Assembly of DNA nanoparticle actuator	83
8.2.2	Ultra high electric field in micrometer scale	84
	Appendixes	93
	Appendixes	103
	Appendixes	113

Chapter 1

Introduction

The concepts of nanoscience and nanotechnology were first discussed in 1959 by the American physicist Richard Feynman in his lecture "There's plenty of room at the Bottom" [13]. In this lecture held at Caltech, Feynman described the possibility of direct manipulation of individual atoms and molecules.

From the conceptual point of view, nanotechnology is a research area where at least one dimension is in the range of nanometers (0.1nm to 100nm). After several decades of development, the research on nanoscience and nanotechnology has achieved huge success in both theory and application and is often considered to be one of the most promising areas in the 21st century.

In this thesis, much of the focus is on a particular kind of nanomaterial, the carbon nanotube. With different kinds of experimental methods, I have analyzed the properties of carbon nanotubes in different applications. A large share of CNT applications are related to macromolecules, such as proteins, polysaccharides etc, and this aspect is important in this work. Systematical research on carbon nanotubes began in 1991 after Sumio Iijima's famous paper in Nature [22], but the first observation of this carbon cylindrical structure can be found much earlier dating back to the 1950's [40]. Some promising areas of carbon nanotube research include structural materials (from tennis rackets to possible future space elevators), ultra fine tips for scanning probe microscopy, nanoelectronic devices, sensors, cancer detection and therapy, drug delivery, and more [0, 10, 12]. Even though carbon nanotube research is still very popular, the number of publications on the Web of Science has been overtaken by graphene research since 2014. In Figure.1.1, I list the three new carbon allotropes in nanotechnology, namely 0D-fullerene, 1D carbon nanotube, 2D graphene with numbers of publications of each year with these as the topic. The research on these three materials started almost from the same period. The first publication of fullerene is from 1985, the first publication of graphene starts from 1991 and the first publication of carbon nanotube also from 1991. In the early 1990s to 2000s, the hottest topic for researchers are clearly the fullerene and the carbon nanotube. There are some publications on graphene, but it is not until 2004, that

the first piece of graphene has been isolated by two researchers at the University of Manchester [39]. After that, graphene research boomed, and in 2014, the number of publications on graphene was larger than that on carbon nanotubes on the Web of Science. Most of the publications with carbon nanotubes as topic are in materials science, chemical physics, applied physics, nanoscience and nanotechnology etc., as shown in Figure.1.1(b)¹.

This Ph.d Thesis work is organized as follows: In Chapter 2, I will describe some basic physical properties of carbon nanotubes, including the different synthesis methods, its band structure etc. The theory of transport in a single carbon nanotube is briefly explained. In Chapter 3, physical and chemical functionalization methods of carbon nanotubes are introduced with a short literature review. After that, in Chapter 4, I will introduce some of the experimental facilities and methods (basic nanofabrication, microscopy, low temperature measurement etc) used in the following experiments. Single (multiwalled) carbon nanotube FET measurements at low temperature will be briefly reported in Chapter 5. In Chapter 6, the varied experiments on carbon nanotube/hemicellulose dispersion and its thin film conductivity applications are presented [Publ. I]. In Chapter 7, physical and chemical adsorption of one particular protein, chimeric avidin, with both physical and chemical functionalization on carbon and silicon surface was discussed [Publ. II]. In Chapter 8, I will introduce related work on nanoparticle surface adsorption, connected with a project to manipulate one single DNA strand in a high electric field [Publ. III].

¹Data from Web of Science

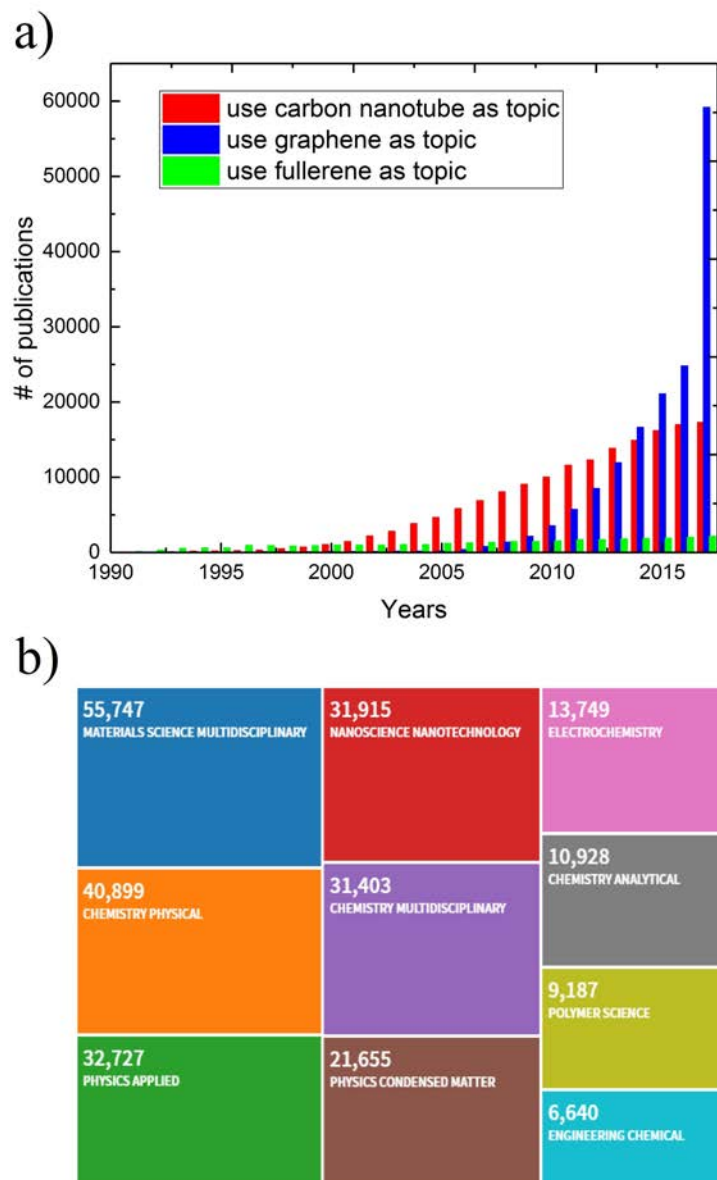


FIGURE 1.1 (a) Number of publications on Web of Science with topic of carbon nanotube, graphene and fullerene for each year. (b) Carbon nanotube research publications in different disciplines

Chapter 2

Introduction to the carbon nanotube

2.1 Synthesis methods

There are several different techniques that have been developed for fabricating CNTs. Commonly used methods include: chemical vapor deposition (CVD), laser ablation and the arc-discharge technique [32].

The arc-discharge technique involves biasing a sharp high purity graphite rod to many thousand volts in a vacuum chamber with inert gas supply. As current discharges from the rod, it vaporizes some of the carbon on it. In this so called arc process, the carbon is locally heated to approximately 4000 K. As the carbon vapor cools down, CNTs are formed. There is no need to use catalyst precursors in the arc discharge method for MWNTs synthesis, while for SWNTs the catalyst precursors must be present. One of the drawbacks of the arc-discharge method of growing CNT is that the final product always contains a lot of amorphous carbon which needs to be removed for real applications.

Laser ablation works with a similar mechanism as the arc-discharge method. Instead of using high voltage to heat through the graphite rod, a focused and powerful laser is used to rapidly heat the carbon and vaporize it. The problem with the laser ablation method is its low yield and the high price of the products.

The CVD method to synthesize CNTs is the simplest and the most popular

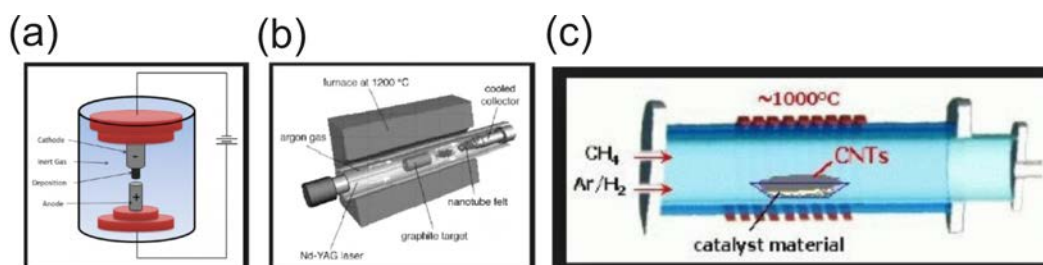


FIGURE 2.1 Three commonly used carbon nanotube synthesis methods; (a) Arc discharge; (b) Laser ablation; (c) Chemical vapor deposition (CVD). Reprint from ¹

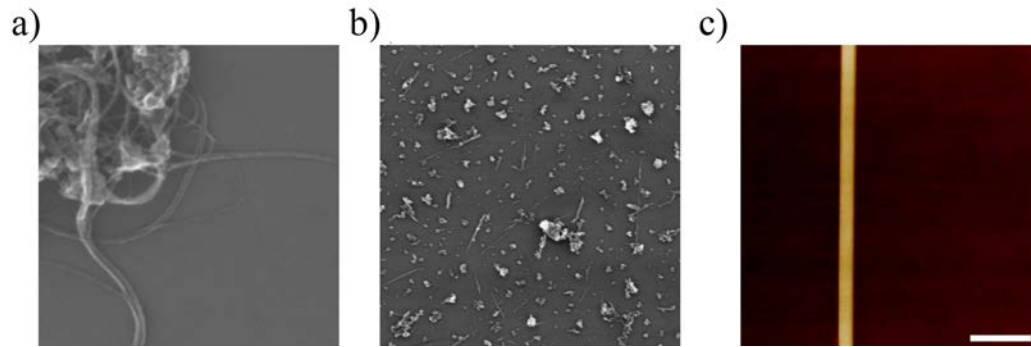


FIGURE 2.2 Comparing different synthesis methods of CNT deposit on silicon surface: (a) SEM image of a typical CVD grown CNTs; (b) SEM image of a typical arc-discharge synthesized MWCNT with a lot of carbon debris; (c) AFM image of an arc-discharge MWCNT after cleaning with nearly defect free outshell, scale bar 100 nm

method to grow CNTs in a laboratory. A CVD system for CNT growth injects a vaporized hydrocarbon compound (methane or ethane) into a high temperature zone in a furnace where a pre-deposited thin film of iron, nickel or cobalt has been deposited. One interesting application of CVD synthesis of CNTs is the possibility to form a highly aligned CNT array (CNT forest).

Comparing with CVD grown CNTs, arc-discharge CNTs usually have better geometry and electronic transport properties. As it is mentioned above, there is no need for metal catalyst for arc-discharge synthesis method for multiwalled carbon nanotubes, therefore it is possible to obtain very high quality of CNT without any metal particles. In figure.2.2, are two typical SEM images of CNTs grown with CVD and arc-discharge methods. From geometrical consideration, CVD grown CNTs generally have less amorphous carbon debris but much more curvature and a lot of defects on its outer shell. On the other hand, arc-discharge CNTs from SEM have better quality, and are more likely to be straight. After removing amorphous carbon, the rest of CNTs have a much better quality (shown in AFM image of 2.2(c)).

2.2 Electronic band structure of a carbon nanotube

A single-walled carbon nanotube is usually regarded as one rolled up sheet of graphene, while a multi-walled carbon nanotube can be treated as multiple concentric single-walled carbon nanotubes. Therefore the honeycomb hexagonal lattice of graphene (Fig.2.3) is the starting point for studies on the band structure of carbon nanotubes. In solid state physics, this structure belongs to the triangular Bravais lattice. Two neighboring carbon atoms (see Fig.2.3 (A), sublattice A and sublattice B), with distance of 0.142 nm, compose its Bravais lattice unit cell. The two Bravais lattice vec-

tors satisfy Equation.2.1.

$$a_{1 \text{ or } 2} = \frac{a}{2}(\pm 1, \sqrt{3}) \quad (2.1)$$

where a is the lattice constant. In a simplest mode of tight-binding model of a graphene honeycomb, the energy dispersion relation of graphene follows Equation.2.2

$$E^\pm(k_x, k_y) = \pm\gamma_0 \sqrt{1 + 4\cos\left(\frac{\sqrt{3}k_x a}{2}\right)\cos\left(\frac{k_y a}{2}\right) + 4\cos^2\frac{k_y a}{2}} \quad (2.2)$$

where γ_0 is the nearest neighbor hopping parameter, and k_x and k_y are the wave vectors in the Brillouin zone.

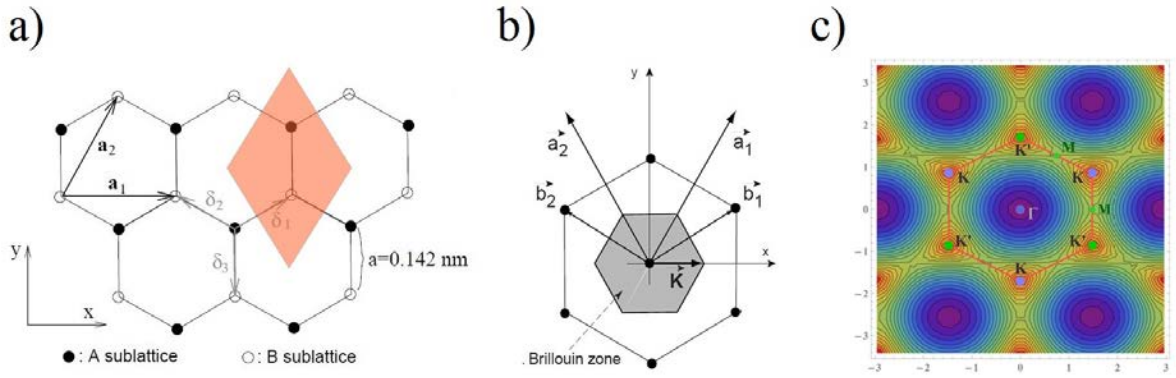


FIGURE 2.3 (A), Honeycomb lattice of graphene. \mathbf{a}_1 and \mathbf{a}_2 are the lattice vectors. [24]. (B), Reciprocal lattice of graphene with 1st Brillouin zone (shaded) [42]. (C), Extended reciprocal lattice of graphene. Figure from Vladimir Gavryushin Mathematica modeling.

A chiral vector \vec{C} with two numbers (n, m which are integers), is used to define a certain carbon nanotube.

$$\vec{C} = n\vec{a}_1 + m\vec{a}_2 = (n, m) \quad (2.3)$$

Based on the chirality, carbon nanotubes can be divided into three types, namely armchair ($m = n$), zigzag ($m = 0$) and chiral CNTs. A nanotube's diameter follows:

$$D = \frac{|D|}{\pi} = \frac{a\sqrt{(n^2 + nm + m^2)}}{\pi} \quad (2.4)$$

For the energy dispersion relationship of a CNT, a small modification to the relationship of graphene in Equation.2.2 is needed. This modification comes from the quantization of the perpendicular wave vector around the tube circumference [35]. In the direction parallel to the CNT axis, electrons are free to move with larger distance (up to 100s nm). The electron wavenumber in the parallel direction k_{\parallel} is effectively continuous. While quantized k_{\perp} is determined by the boundary condition around

the tube circumference as Equation.2.5

$$\pi Dk_{\perp} = 2\pi j \quad (2.5)$$

where j is an integer. Inserting this boundary condition to Eq. 2.2, the energy dispersion relation of the carbon nanotube follows as:

$$E_q^{\pm}(k_y) = \pm\gamma_0 \sqrt{1 + 4\cos\left(\frac{\pi q}{n}\right)\cos\left(\frac{k_y a}{2}\right) + 4\cos^2\frac{k_y a}{2}} \quad (2.6)$$

Let k_y be along the Γ -K direction, at the zone boundary $k_y = \frac{\pi}{a}$, the energy gap becomes $E = \pm\gamma$ (unlike graphene zero energy gap). When $n - m = 3q$, where q is an integral, the carbon nanotube is metallic, otherwise it is semiconducting. For approximation, for unpurified carbon nanotubes, around one third of SWNTs are metallic and the other SWNTs are semiconducting.

Decomposing the wavevector \vec{k} into a component along the tube axis (k_{\parallel}) and a perpendicular vector as (k_{\perp}), and the band structure of carbon nanotube can be approximated by Equation.2.7

$$E(\vec{k}) = \pm \frac{2\hbar v_F}{d} \sqrt{\left(\frac{m-n}{3} + p\right)^2 + \left(\frac{k_{\parallel} d}{2}\right)^2} \quad (2.7)$$

Where, v_F is the Fermi velocity and p is an integer. For a metallic nanotube, the dispersion relation near the Fermi level satisfies:

$$E^{\pm}(\delta\vec{k}) = \pm \frac{\sqrt{3}a}{2} \times \gamma_0 |\delta\vec{k}| \quad (2.8)$$

For semiconducting tubes, this relationship becomes

$$E^{\pm}(k_{\parallel}) = \frac{\sqrt{3}a}{2} \gamma_0 \sqrt{\left(\frac{2\pi}{|C_h|}\right)^2 \times \left(q \pm \frac{1}{3}\right)^2 + k_{\parallel}^2} \quad (2.9)$$

By further simplifying Equation.2.9 we can get the band gap as:

$$E_g = \frac{2d_{cc}\gamma}{\sqrt{3}d} \quad (2.10)$$

Considering that γ , which is the nearest neighbor hopping parameter, varies from 2.5-3.2 eV, from which follows that the band gap of a 1nm wide semiconducting tube is roughly 0.7 eV to 0.9 eV [36].

The unit cell of a CNT contains 2N atoms instead of 2 atoms like in graphene. Of these 2N atoms, a total of N bonding π orbitals and N antibonding π^* orbitals are formed. When at absolute zero temperature, all the electrons are in the valence band

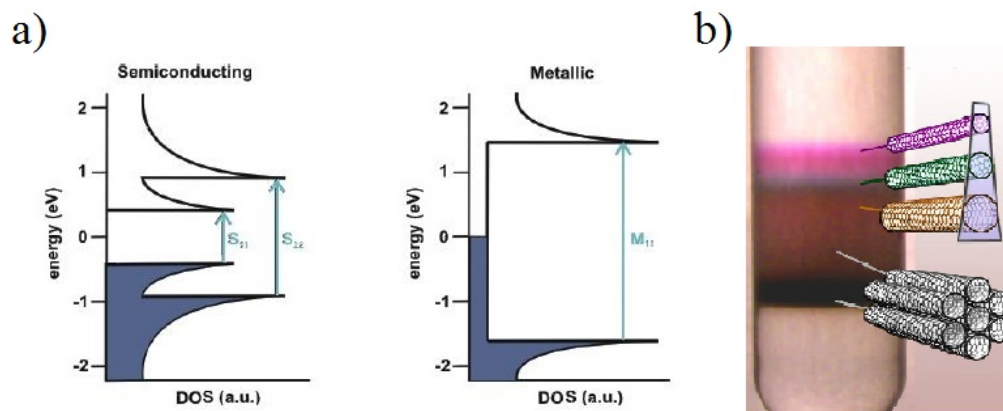


FIGURE 2.4 Schematic representation of the electronic density of states of a semiconducting (left) and metallic (right) SWCNT. (b) Centrifuge tube with a solution of carbon nanotubes, which were sorted by diameter using density - gradient ultracentrifugation [3]

(shown in 2.4 as blue color. So for semiconducting CNTs, at absolute zero temperature, the conductivity is zero for small bias lower than the band gap. For metallic CNT, the conductivity does not depend on the temperature, because there is no band gap at the Fermi surface.

Beside these covalent bonds between neighboring carbon atoms in CNTs, weak interactions, such as the van der Waals force and the $\pi-\pi$ stacking make CNTs easily aggregate into “ropes” or “bundles” (Fig.2.2(a)). How to disperse these aggregated CNT polymers is still a vivid research area in CNT functionalization.

2.3 Transport properties of a carbon nanotube

A short summary of mesoscopic transport theory as discussed in the context of single CNTs, has been given, for example, in Ref [16]. The Landauer formula is generally used for the conductance of a quasi 1D system

$$G(E) = \frac{2e^2}{h} M(E)T \quad (2.11)$$

Where $M(E)$ is the number of subbands contributing to the charge transfer and T is the average transmission probability of each subband. For a mesoscopic system, three different kinds of characteristic lengths are usually used for a semi-classical analysis. The mean free path l_m , the Fermi wavelength λ_F and phase relaxation length τ_ϕ are therefore be introduced. The mean free path is the average distance that electrons can freely travel before they scatter.² The Fermi wavelength λ_F is the

²For a perfect crystalline carbon nanotube, the mean free path should be infinite. However, the perfect crystalline CNT never exists in the real world. For very short channel, it is possible to fabricate

de Broglie wavelength of electrons at Fermi energy and the phase relaxation length is the average length where the electron retains its coherence as a wave. Elastic scattering of electrons (electron with impurity) doesn't contribute for l_ϕ , but only contributes for l_m . However, inelastic scattering contributes for both of them. Only the electrons near the Fermi energy (for simplicity at $E_F \pm kT$) contribute in transport, so the lengths l_m and l_ϕ are scaled by Fermi velocity as follows: $l_m = v_F \tau_m$ & $l_\phi = v_F \tau_\phi$

Transport through the system can be classified into three different regimes: ballistic, diffusive and classical. The relationship between the characteristic lengths determines then the transport regime. The conductance is ballistic when the 1D channel length between contacts is smaller than the mean free path and the phase relaxation length of the channel ($l < l_m$ and l_ϕ). In a situation where there is no scattering center in the channel, the transmission probability T reaches 1. For this case, the CNTs are reported to be 1D ballistic conductors. For metallic CNTs, T at maximum could be 2, because two subbands cross at the Fermi level. For semiconducting CNT, there is only one channel that acts as a conduction channel. So the theoretical maximum conductance for a metallic CNT is

$$G_q = \frac{4e^2}{h} = 2G_0 = 1.549 \times 10^{-4} S, \text{ or } R_q = 6.45 k\Omega \quad (2.12)$$

For a semiconducting CNT at low temperature (where thermal energy is smaller than band gap), the theoretical maximum conductance is

$$G_q = \frac{2e^2}{h} = G_0 = 0.774 \times 10^{-4} S, \text{ or } R_q = 12.9 k\Omega \quad (2.13)$$

A carbon nanotube transistor working in its ballistic transport region with theoretical transport limit of $4e^2/h$ with little Schottky barriers has been made [23].

CNT transistors with length smaller than its mean free path. Thus, it is possible to fabricate a ballistic CNT transistor

Chapter 3

Carbon nanotube/graphene and their complexes with macromolecules

In this chapter, I will briefly introduce some macromolecules and the current knowledge of their complexes with carbon nanotubes / graphene. In this Ph.D. thesis several different kinds of such complexes have been analyzed. Macromolecules of interest here are avidins, a protein and hemicellulose (Section.3.1). The adsorption of macromolecules can generally be divided into two categories, namely physical adsorption and chemical adsorption. For the formation of the CNT/macromolecule complexes, physical adsorption methods are almost exclusively used in this thesis unless specifically mentioned. A brief summary of previous researches of physical and chemical adsorption will be introduced in Section 3.2. Some good examples of previous works related to avidin functionalization on carbon material surfaces are also included.

3.1 Bio-macromolecules

Macromolecules are according to the IUPAC definition: molecules of high relative molecular mass, the structure of which essentially comprises the multiple repetition of units derived, actually or conceptually, from molecules of low relative molecular mass. Typically, biological macromolecules refers to carbohydrates, lipids, proteins and nucleic acids, the four large molecules comprising living things. In this Ph.D Thesis, two specific biomacromolecules, namely chimeric avidin and hemicellulose have been studied.

3.1.1 Proteins

Proteins, from Greek word “proteios” (meaning “first place”), account for more than 50 percent of the dry mass of most cells [18]. Based on their functionalization in organisms, proteins can be divided into enzymatic proteins, structural proteins, stor-

age proteins, transport proteins, hormonal proteins, receptor proteins, contractile and motor proteins and defensive proteins. Clinically, the measurement of certain proteins in blood or urine is widely used as direct evidence of certain disease or health disorder.

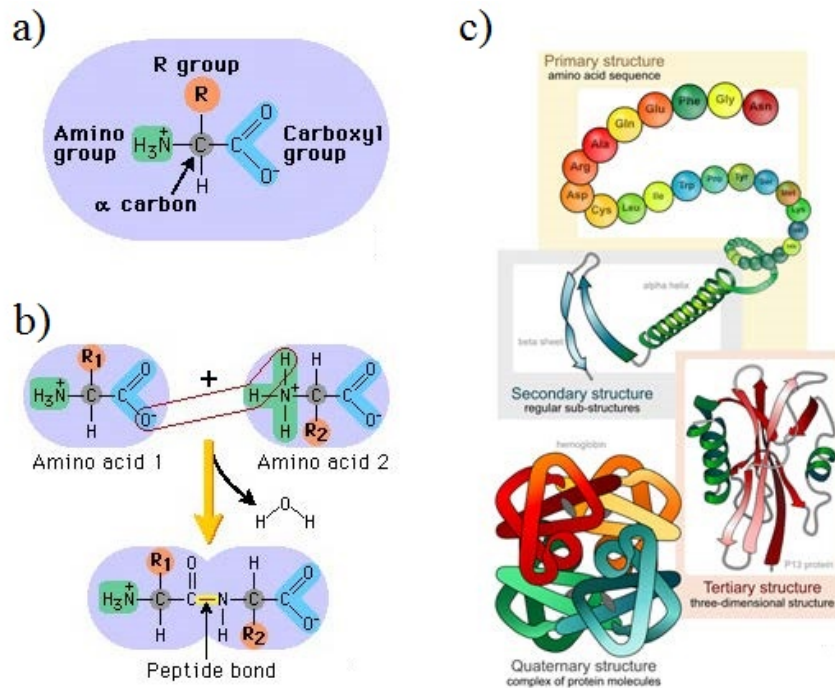


FIGURE 3.1 (A), Components of the amino acid; (B) The peptide bond formation by two amino acids; (C) The four level structure of protein, from primary to quaternary structure. Reprinted from Pearson BioCoach Activity and Wikipedia

From a chemical point of view, all proteins in human body are constructed from a set of 20 different amino acids (see Figure. 3.1(A)). These amino acids are composed of identical amine ($-\text{NH}_2$) and carboxylic acid ($-\text{COOH}$) functional groups, and a variable side chain ($-\text{R}$). In cells, amino acids are translated from messenger ribonucleic acid (mRNA) in ribosomes. To specifically determine one amino acid, it needs three nucleotide bases on mRNA. The translated amino acids join with each other and form a sequence under a dehydration reaction (one amine group and one carboxylic acid group forms one peptide bond). Artificial modification of one protein's amino acid sequence by genetic engineering is possible in laboratory.

This amino acid sequence is called the protein's primary structure. In this sequence, the unbounded amine and carboxylic acid groups at the ends of the backbone peptide chain are called N-terminus and C-terminus. The primary structure of protein will continue to coil or to fold to form either an " α helix" or a " β sheet" (see Figure. 3.1(B)), due to hydrogen bonding between main-chain peptide groups. This is called the protein's secondary structure. Moreover, due to the formation of disulfide bridges, and the tendency of the hydrophobic parts under the weak hy-

drophobic force to hide into the core region, one obtains the protein's tertiary structure. And finally, some proteins consists of more than one polypeptide chain, from which arises the quaternary structure (see Figure.3.1(C)).

Avidin is a protein which can be found in egg white and tissues of birds, reptiles and amphibians [14]. It contains four identical subunits and consists of 128 amino acids while having a combined mass of 67,000 - 68,000 Dalton [30]. The extent of glycosylation ¹ on avidin is high, which gives it a relatively high nonspecific binding property.

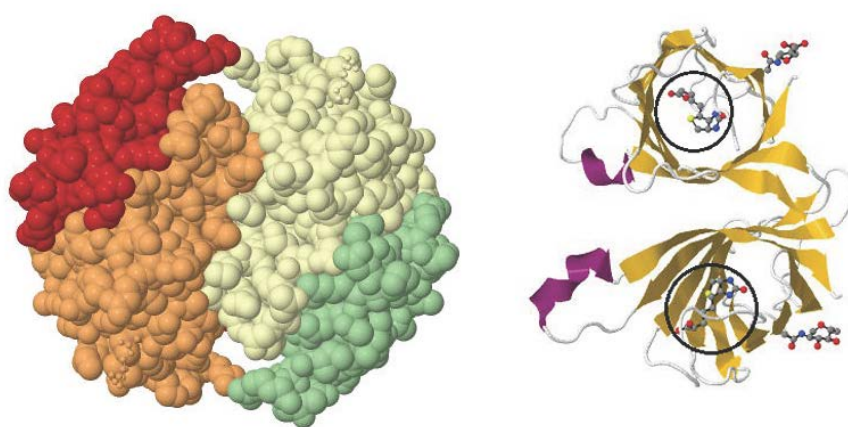


FIGURE 3.2 The three dimensional structure of avidin and biotin. The space filling model (left) shows the structure of four identical subunits. The ribbon diagram (right) displays asymmetric unit consisting of two subunits with eight strands of β barrel structure and biotin molecules (in the black ovals) in the binding pockets².

In biophysics, avidin is famous for its high affinity to biotin (Fig.3.3(A)). Each subunit can bind one molecule of biotin, with a dissociation constant of $K_D = 10^{-15}M$. This property makes it one of the strongest known non-covalent bonding, and widely used as crosslinker. The isoelectric point for avidin (the pH at which a particular molecule or surface carries no net electrical charge) is 10.5. In neutral buffer avidin is positively charged.

Chimeric avidin was used in this Thesis work. It was first assembled in 2004 by Vesa Hytönen et al [20] using E.coli. The name "chimeric" comes from its particular stability against harsh chemical conditions [20]. The molecular mass of chimeric avidin is 52.6 kD and the enthalpy of chimeric avidin-biotin binding is -112.6kJ/mol [33].

¹Glycosylation: reaction with a carbohydrate

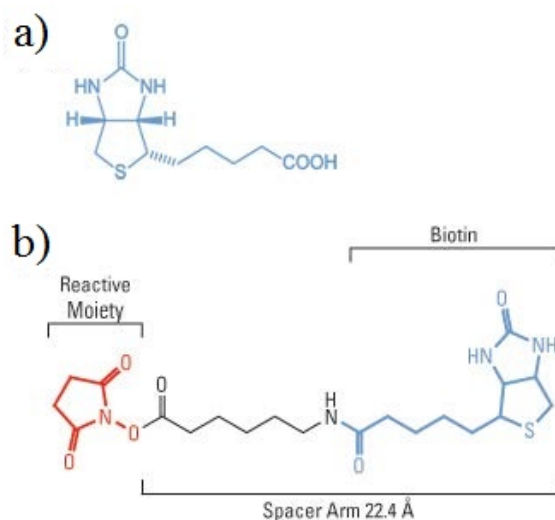


FIGURE 3.3 (A), Molecule structure of biotin; (B) Biotin-LC-NHS conjugation, where biotin molecule (blue) is conjugated to a reactive group (red) either directly or with additional chemical spacer (black) [0].

Biotin (also known as Vitamin B₇, see Fig.3.3(A)), is an essential coenzyme required by all forms of life. It can be synthesized by plants, most bacteria and some fungi. In cells, biotin is involved as an enzyme in the synthesis of fatty acids, isoleucine and in gluconeogenesis etc. In biophysics, biotin is widely used as cross linker or for molecule modification (biotinylation) for the following reasons. Firstly, the interaction between biotin and avidin has an extremely high affinity ($K_a=10^{15} M^{-1}$). Once the binding is formed, it is unlikely to be affected by extreme pH, temperature, organic solvents or other denaturing agents [0]. In addition, biotin is a comparatively small molecule, which does not interfere with its targeting molecule's properties. Thirdly, biotin has a valeric acid side chain (Fig.3.3(A)) which can be used for further conjugation or modification of its spacer arm(Fig.3.3(B)).

Streptavidin is a tetrameric protein, which is isolated from streptomyces avidinii [0]. Previous research shows that it has only 30 percent sequence identity to avidin, but their secondary, tertiary and quaternary structure (see Fig.3.2 are quite similar. Compared to avidin, streptavidin has at least two advantages when choosing a biotin-conjugate binder. The first advantage is that streptavidin has little carbohydrate component on its surface, which could in principle lower the possibility of non-specific binding due to pure hydrophobic interaction. The second advantage is that streptavidin has a mildly acidic isoelectric point of 5.5, and little net charge in neutral buffers.

3.1.2 Cellulose and hemicellulose

Cellulose, $(C_6H_{10}O_5)_n$, is a polysaccharide compound which consists of a linear chain of several hundred to many thousands of $\beta(1 \rightarrow 4)$ linked D-glucose units. It is the most abundant organic polymer on Earth. The cellulose content in cotton fiber is 90 percent, in wood 40-50 percent, and in dried hemp approximately 60 percent.

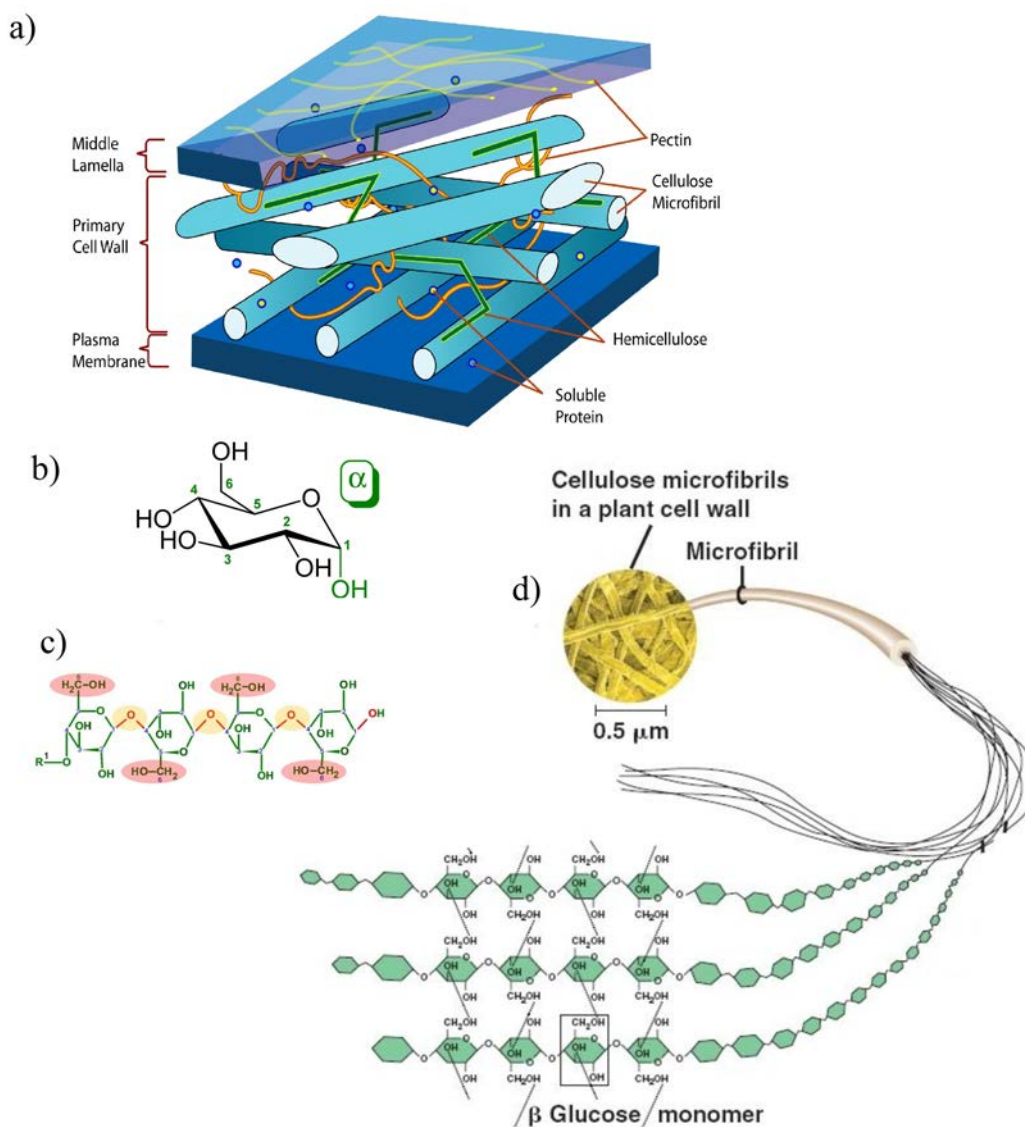


FIGURE 3.4 (a) Section of a cell wall with mixture of cellulose microfibril and hemicellulose; ³(b) chair form of α -D-glucopyranose that is the main component of cellulose; ⁴(c), $\beta(1 \rightarrow 4)$ glycosidic bonds during the D-glucose units condensation; (d), Cellulose microfibrils in a plant cell wall. The interaction between each cellulose chain is mainly from hydrogen bonds⁵. Figure 3.4 (a-c) are reprinted from wikipedia, Figure. 3.4 (d) is reprinted from kerinakay Wordpress

Hemicellulose is also a polysaccharide compound. However, it contains many different sugar monomers instead of pure D-glucose units like cellulose. The sugar monomers in hemicellulose can include xylose, mannose, galactose, rhamnose and arabinose. Unlike cellulose, hemicellulose consists of shorter chains, usually with 500 to 3000 polymer units compared to 7000 to 15000 glucose polymer unit in cellulose. Also, hemicellulose is a branched polymer, while cellulose is an unbranched polymer.

In this Ph.D thesis, the hemicellulose used is so called "nanocellulose" materials. The nanocellulose fiber diameter is below 100nm, usually from 5 nm to 30 nm, and length of several micrometers [2]. From previous studies, nanocellulose is usually used as reinforcement in nanocomposites, due to its high Young's modulus (138GPa in its longitudinal direction) and a very low coefficient of thermal expansion (10^{-7}K^{-1} in its longitudinal direction). Nanocellulose could also be used for optical reinforcement material, as it is suggested that they are free of light scattering, which could be useful in transport resins.

3.2 Physical and chemical adsorption of macromolecules on carbon nanotube and graphene

Macromolecules that interact with different kinds of surfaces and form macromolecule /surface complexes have a lot of useful applications in practice. Depending on the strength and characteristics of interaction, these formation processes can be divided into two categories: namely chemical adsorption and physical adsorption.

Physical adsorption methods based on the relatively weak interaction (hydrophobic interaction, van de Waals force etc) between a macromolecule and substrate's surface, are usually very easy to manipulate for an experiment. However, there are some inevitable drawbacks from its nature. The first obvious one is that they are not as robust as chemical functionalization. The second is that the direct interaction of a macromolecule with a carbon nanotube/graphene could easily induce denaturalization of a macromolecule, for example due to the hydrophobic-hydrophobic interaction.

Chemical functionalization, on the other hand, is based on much stronger chemical bond to link a macromolecule to the surface. Two general approaches are: (a) Direct chemical bond formation between a macromolecule and the surface (for example, a protein with thiol group can directly form sulfur-gold interaction on gold surface), (b) indirect chemical bond with the surface through the "cross linker". Cross linkers are molecules that contain two or more reactive ends with specific functional groups capable of bonding to a macromolecule and a surface. A number of reactive chemical groups have been used in research, such as carboxyl to amine reactive groups, amine reactive groups, sulfhydryl reactive groups, aldehyde reac-

tive groups etc. In practice, chemical functionalization is almost exclusively used in all experiments [41].

One interesting thing of orientation control with chemical cross linker, is that the discussion of it is sometimes ambiguous. Unless there is only one reactive group on the surface of a macromolecule, the chemical cross linker cannot guarantee any orientation preferences for a macromolecule. In that case, the chemical adsorption is still partly non-specific bonding [8,9], and the advantage compared to pure physical adsorption of a macromolecule is limited.

Physical and chemical functionalization methods of CNTs have already been widely researched during the last decade with numerous outstanding experiments and computer simulations.

3.2.1 Covalent functionalization of carbon nanotube

Covalent functionalization of carbon nanotubes use active carbon atoms on CNTs as precursor for silanization, polymer grating, esterification, thiolation, alkylation and arylation process [32]. These active carbon atoms usually come from two following situations: (A) "Stone-Wales" defects, where six membered rings of graphene transfer into the mixture of pentagons and heptagons (see Fig.3.2.1(A)); (B), rehybridized carbon atoms at the capping areas on CNT. From simulation and Raman spectrum, it predicts that these activated carbons typically account for 1-3 percent of the atoms in pristine carbon nanotubes [25].

Some common methods for covalent functionalization of carbon nanotube side-wall include: oxidize to hydroxyl group (-OH) or carboxyl group (-COOH), fluoride to carbon-fluoride bond (C-F), halogenate CNT to C-Cl or C-Br bonds etc. [32]. Focusing on CNT's oxidization (see Fig.3.2.1(B)), common oxidants like piranha solution, KMnO_4 , ozone and reactive plasma have already been used [32]. Scanning electron microscopy images and infrared spectrum (or Raman spectrum) before and after oxidation are routinely used for analysis. However, this method may degrade the CNT's mechanical or electrical properties. It is possible that the CNT's structural integrity has been broken during the functionalization process, which could turn them useless when they are assembled into an electronic circuit.

After oxidation, the next step for molecular binding modification was adding the cross linker. One of the so called "universal" methods for protein immobilization is the NHS-EDC method. This method uses a two-step process with N-ethyl-*N'*-(3-dimethylaminopropyl) carbodiimide hydrochloride (EDAC) and N-hydroxysuccinimide (NHS) to specifically bind with protein's α amino groups [25](Fig. 3.2.1(C)). The reaction mechanism in short can be explained as follows: carboxylic acid groups on the carbon nanotube were first reacted with EDAC, forming a highly active O-acylisourea ester. This intermediate can form a more stable succinimidyl interme-

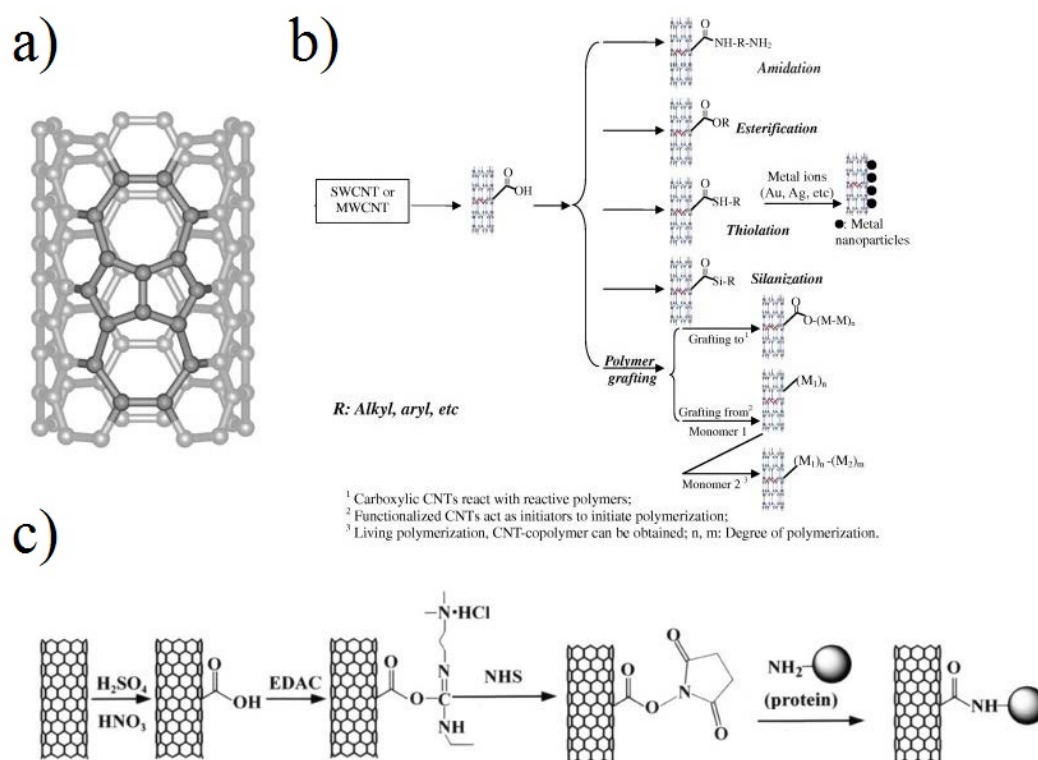


FIGURE 3.5 (A) Stone-Wales defect on the sidewall of nanotube; (B) Strategies for covalent functionalization of CNTs (AL direct sidewall functionalization; B: defect functionalization) [32]. (C) Schematic view of the attachment of proteins to carbon nanotubes via a two-step of dimide activated amidation. Modified from Jiang et al. [25]

diate ester with NHS. The amine reactive NHS ester can function with the primary amine group on a protein to finally form a stable conjugate by amide bonding.

3.2.2 Non-covalent functionalization of CNT

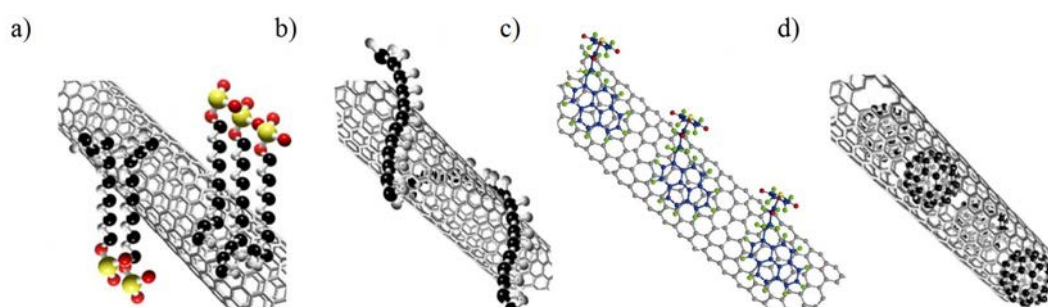


FIGURE 3.6 (A), Noncovalent adsorption of surfactant; (B), Wrapping of polymers; (C) 1-pyrenebutanoic acid succinimidyl ester adsorption of carbon nanotube (modified Figure from Fan et al. ; (D) endohedral functionalization of C_{60} . Figures are reprinted from [32]

Non-covalent functionalization or physical functionalization of carbon nanotubes does not depend on the active carbons or defects on the CNT's structure. So in principle, it will not destroy the conjugated system of the CNTs sidewalls. Physical functionalization (adsorption) on carbon nanotubes can be classified as polymer wrapping (Fig.3.6(B), surfactant adsorption and endohedral methods etc [32]. Some of the promising results for biomolecular detection with physical functionalization, for example, by 1-pyrenebutanoic acid succinimidyl ester was first used by Dai et al [8]. This method can also be thought of as universal method for specific binding with protein's primary amino group [8](see Fig.3.6(C)). For short, 1-pyrenebutanoic acid succinimidyl ester adsorbs on the sidewall of CNT by $\pi - \pi$ binding, and the succinimidyl ester covalently binds with a primary amine group on a protein.

3.2.3 Previous works of avidin adsorption on a surface

Nearly all previous works on adsorption of avidin on surfaces, either macroscopic or nanoscale, use the above mentioned biotin-avidin interaction to accomplish the binding to the surface.

Scanning probe microscopy can give useful information about the conformation change of a single avidin at the molecular level. The research topics of scanning probe microscopy on avidin are mainly: (a) 2D lattice structures on biotin labeled surface; (b) force measurements using biotin labeled AFM tip to analyze the mechanical strength of the avidin-biotin interaction; (c) molecular level single protein characterization. Some interesting and important work related to the protein physical adsorption on carbon material surfaces are shown in Fig.3.7. Fig.3.7(a) shows the analysis of the streptavidin helices formed on MWNT with computed power spectrum of the Fourier transform of a helical array of streptavidin molecules [4]. Fig.3.7 (b) compare with the same carbon nanotube before and after nonspecific ferritin adsorption on a nanotube [9]. Fig.3.7(c), the authors used the AFM to show high magnification surface topographies of streptavidin 2D crystal structure on mica supported lipid bilayer [0]. Despite these works, a systematic experimental study of avidin class physical deposition on surfaces has not been done.

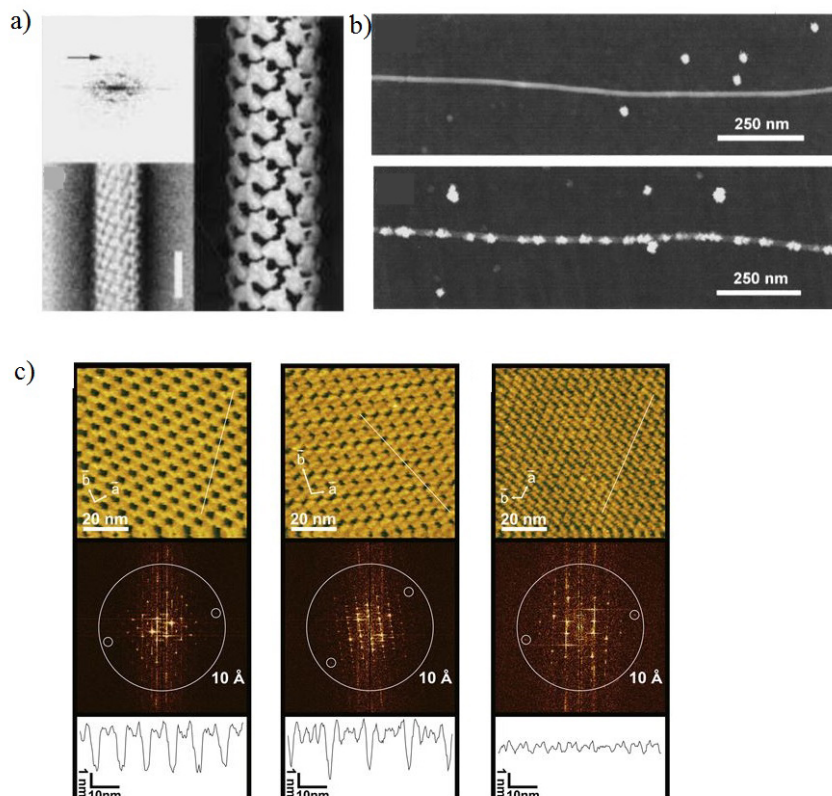


FIGURE 3.7 (a) Analysis of streptavidin helices formed on a MWNTs with helical repeat of 12.8 nm, Reprinted from [4]; (b) An AFM image showing protein A non specifically (chemical) adsorbed on a nanotube [9] ; (c) High magnification surface topographies of streptavidin 2D crystals formed on mica supported lipid bilayer. The space group symmetries of the crystals are (A) type-1 P2, (B) type-2 P2, and (C) type-3 P2. [0]

Chapter 4

Experimental facilities

The research topic in this Ph.D thesis can be described as experimental physics with nanometer scale materials. There are different kinds of experimental facilities that have been used. In principle, all the experiments in the following chapters have these three steps: (1) sample fabrication (mainly done in the cleanroom in NSC with normal nano-microfabrication processes, E-beam lithography, CVD, PVD, RIE etc), (2) sample characterization (with optical microscope, AFM, SEM etc); (3) DC conductivity measurement at low temperature and optical measurements. In this chapter, I will briefly explain some most commonly used methods that I will be talking about in the following chapters.

4.1 Nanofabrication facilities

A cleanroom is a place where the number of particles is being constantly monitored and controlled. The number of particles per cubic meter is a very important factor for both experiments and for real industrial manufacturing as it helps to improve the yields of production. The standards of a cleanroom is also defined by the number of particles per cubic meters. The Nanoscience Center (NSC) of the University of Jyväskylä, has a ISO-5 class cleanroom.

Micro/Nano-lithography is the key technology area of nanometer-scale fabrication. Several different kinds of techniques can be used for these processes, like optical lithography, electron beam lithography (e-beam), nanoimprint lithography, multiphoton lithography, and scanning probe lithography. At industrial level, optical lithography with UV (ultraviolet) or EUV (extreme ultraviolet) is almost exclusively used in any CPU or electronic chip manufacturing. The limitation of optical lithography used in the university or R & D for small company is that it is extremely expensive to have a resolution under 100 nm. Besides, it is not economically favorable to make a photolithography mask for every experiment. In my ph.d thesis, both photo-lithography and e-beam have been used. For micrometer-size structure, I used Karl Suss MA45 UV system, for nanometer size structure, I used Raith Eline

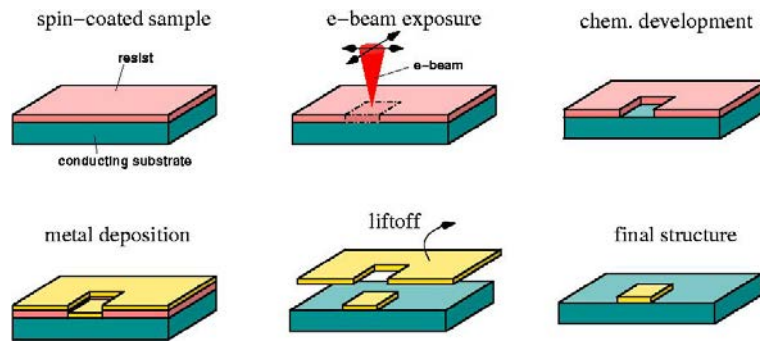


FIGURE 4.1 General process of e-beam lithography. Ontop from left to right: spin coating with resist (PMMA); using electron beam to patterning on the resist; (c) developer to remove the resist that was exposed to the electron beam; (d) metal deposition with PVD; (e) lift off with Acetone and IPA; (f) drying the same for storage or testing;
1

Plus system. The general process of e-beam lithography is shown in Fig.4.1.

The electron beam lithography instrument used in this Ph.D thesis was the Raith Eline. It is in practice a scanning electron microscope (SEM) modified into an e-beam lithography system with high resolution, high beam dose and good spot position control.

TABLE 4.1 Raith Eline's parameters from Nanoscience Center

Properties	Measured
Filament	Schottky thermal field emission source
Beam size	1.8nm 20 keV 3.5nm 1 keV
Beam current range	5 pA- 20 nA
Beam energy	100 eV - 30 keV
Min.feature size	18.2 nm line

After the substrate is spin coated with an electron sensitive resist (polymethmethacrylate PMMA), a high energy electron beam was directed on the resist, resulting in a change in PMMA's solubility. Instead of a mask that is used in photolithography, the patterning of E-beam lithography was based on the software. Patterning can be modified simply with majority of CAD software. Some key specification of Raith e-line was listed in Table4.1

Compared to the optical lithography process, e-beam lithography is a much slower process. The charging effect on the dielectric materials can sometimes induce a cross-talk with two electrons exposing a single spot. So it is usually necessary to have some doping done before doing really small structures.

In this work, ultra high vacuum (UHV) evaporation was used. UHV was supplied by Instrumentti Mattila Oy. This instrument can be used for deposition of met-

als with pressure of 10^{-9} mbar². It should be known that with PVD, the metal thin layer growth can be of high quality, but is still far from epitaxy condition.

4.2 Modern microscopes

Due to the diffraction limit, optical microscopes are often far from the requirement of nanoscale research. In our nanoscience study, we used the scanning electron microscope and the scanning probe microscope.

Scanning electron microscope

A scanning electron microscope (SEM) is a type of microscope that produces images of a sample by scanning the surface with a focused beam of electrons. When the specimen is irradiated with a fine electron beam, secondary electrons are emitted from the specimen surface. An image is obtained when the electron probe raster-scans over the surface and simultaneously detects the secondary electrons.

The interaction of the electrons with specimens can be quite complicated. Fig.4.2 (a) show possible emission of various electrons and electromagnetic radiation from the specimen. Typical electrons that could emit from the specimens are backscattered electrons (BS), Auger electrons, and the secondary electrons (SE). For an SEM, BS and SE are the most commonly utilized electrons for detection.

In the Raith E-line system there are three detectors: one normal Everhart-Thornley secondary electron detector nearly horizontal to the specimen; one backscattered electron detector; and one InLens secondary electron detector (also the default use detector) vertical to the sample (Figure. 4.2(B)). The energy-filtered "In-lens" detector was first built for high resolution low energy backscattered electrons [0]. It is not a single electron detector, but a set of four electron detectors. Among these four detectors, the Annular BSE-detector and the Annular SE-detector are called energy selective BE detectors (EsB detectors); the other two detectors, low angle BSE and high angle BSE detectors are called angular selective BE detectors (AsB detectors)(Fig.4.2(B)). In the Nanoscience Center, the Raith e-Line was equipped with an In-Lens secondary electron detector and a normal secondary electron detector. It was generally found that the In-Len SE detector usually provide a higher resolution and sharper imaging for the majority of the cases of this Thesis work.

Scanning probe microscopy

In the early 1980's G.Binning invented the Scanning probe microscope [6] that provided a new method not only to see but also to manipulate nanoscale objects [7].

²<http://www.instrumentti-mattila.fi/home.html>

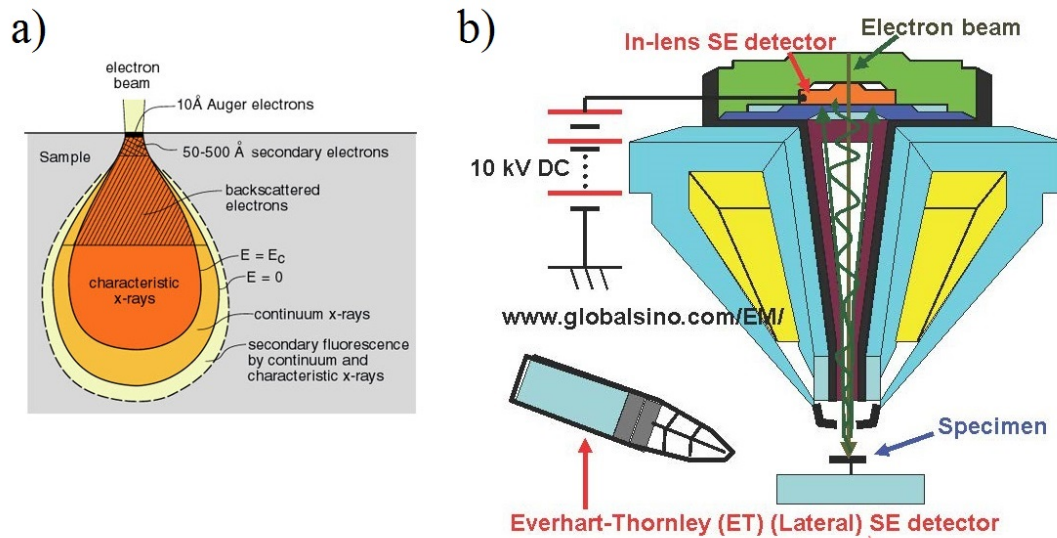


FIGURE 4.2 (A), Generalized illustration of interaction volumes for various electron specimen interaction. Secondary and backscattered electrons are the most widely used detection electrons. ; (B) Position of “in lens” detector and traditional Everhart Thornley detector in the sample chamber. Picture from Practical electron microscopy and database [1]; (C), Casino (Monte Carlo Simulation of electron trajectory in solids) model, with 5nm gold sphere (yellow), 2nm thickness native silicon oxide, and 50 nm thickness of silicon; (D) and (E) Simulation results of electron trajectories, red ones are backscattered electrons.

Generally the scanning probe microscopy (SPM) family can be divided to scanning force microscopy (more commonly atomic force microscopy (AFM)), scanning tunneling microscopy (STM), and Near field scanning optical microscopy (SNOM), based on the detection mechanism. STM is the first manufactured scanning probe microscope that could see an individual atom, however, the problem is that it requires the subject to be conductive. The AFM that was developed several years later overcame this limitation and right now is the most widely used SPM technology in the world.

Two fundamental components of a scanning probe microscopy are the tip and the feedback system. The tip that is on the end of a cantilever that is usually made of silicon or silicon nitride is the point, where SPM interacts with the sample. The feedback system controls the SPM system through a piezo element in an attempt to set a constant error signal to defined a “setpoint”. In AFM, there are three widely used setpoints, which also define three widely used imaging modes. They are the vertical deflection setpoint (contact mode), the amplitude setpoint (tapping mode) and the peakforce setpoint (peakforce tapping mode). The contact mode which usually works in the repulsive force part (Fig.4.3(b)), is the only mode in the AFM that could give an atomic scale resolution. The problem with the contact mode is that the AFM tip is almost all the time in contact with the sample surface, which leads to a tip wear

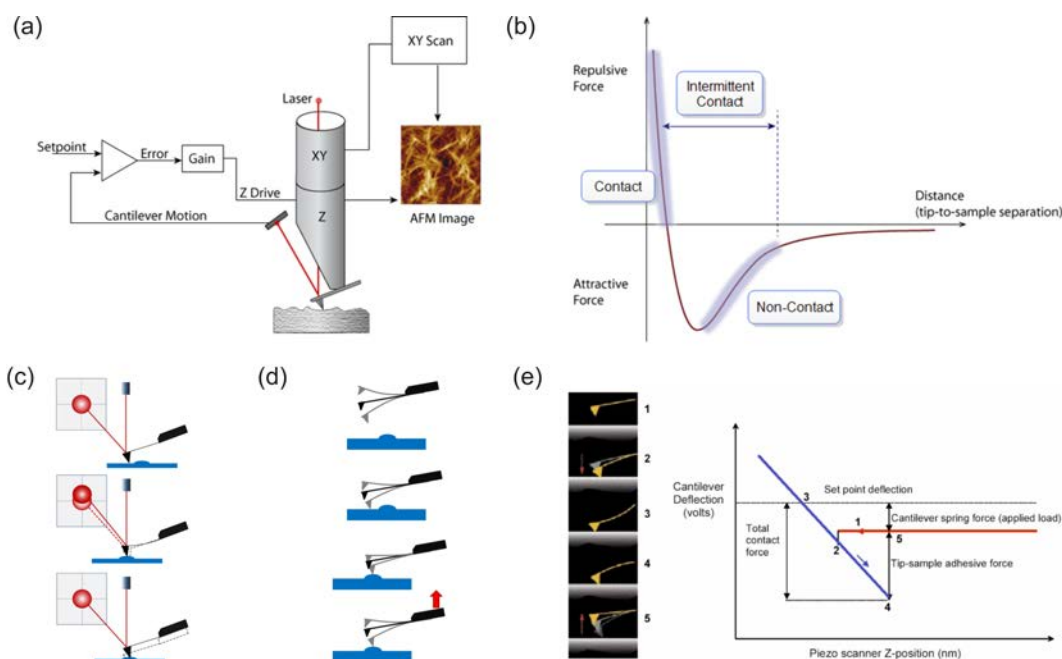


FIGURE 4.3 (a) General AFM operation structure with feedback loop; (b) The force between AFM tip and sample surface; (c) operation principle of Contact mode; (d) operation principle of tapping mode; (e) operation principle of Peakforce Scanasyst

and possibly sample damage. Tapping mode, with a amplitude setpoint, working with both repulsive and attractive force curve, is generally much better with sample damage. It is one of the most commonly used methods for soft materials such as biomaterials like DNA, proteins etc. Peakforce tapping mode, in principle, is more close to the traditional force volume method. The difference between peakforce tapping mode and force volume methods, are mainly: (a) much faster frequency from 0.01kHz to 2 kHz; (b) instead of using linear ramping function, a sinusoidal ramping function has been used to guarantee the smallest interaction between the AFM tip and the substrate.

Modern AFM is not only a microscope, it can also be used to measure different kinds of surface properties with quantitative results. For example, with Bruker Icon QNM (quantitative nanoscale mechanism), researchers can easily obtain the mechanical properties such as materials' Young's modulus, deformation, adhesion and dissipation. Electronic potential can also be measured with Kelvin probe force microscopy (KPFM) and Tunneling atomic force microscopy (TUNA) etc.

Since most of the analyzed objects used in this Ph.D thesis are soft materials or biomolecules, tapping mode or peakforce mode have been used in general. The facilities shown in this ph.d thesis have mostly been obtained from Bruker Icon and some from old Dimension 3100.

4.3 Cryogenics

“Cryogenics is defined as that branch of physics which deals with the production of very low temperatures and their effects on matter”[An introduction to cryogenics] When the temperature is below 120 K it is operationally defined as cryogenics. There are a lot of useful applications of cryogenics in daily life, for example, liquid natural gas (LNG), liquid oxygen and nitrogen used in chemical and metallurgical processes, and cryogenic liquid propellants of rocket engines etc.

For experimental physics and condensed matter physics, cryogenics is also very important technology for measurements. One obvious benefits to do the experiment at low temperature: the thermal noise from phonons could be neglected, and the band gaps becomes more clear because the Fermi tail of electrons becomes very sharp.

Some low temperature phenomena with their characteristic temperatures are shown in table.4.2.

TABLE 4.2 Characteristic temperatures of low energy phenomena

Phenomenon	Temperature [K]
Debye temperature of metals	~ 100
High temperature superconductors	~ 100
Low temperature superconductors	~ 10
Ballistic transport of metals	10
Cosmic microwave background	2.7
Superfluid helium 4	2.2
Bolometers for cosmic radiation	1
Low density atomic Bose-Einstein condensates	$\sim 10^{-6}$

The simplest way of cooling is to immerse the sample into a cryogenic fluid. This makes use of its latent heat of vaporization. The good things with latent heat of vaporization methods are: (a) they are standards methods with well know calibration equilibrium temperature; (b) the temperature of the sample is very stable as long as it is immersed in the cryogenic fluid; (c) without mechanical cooling system, there is little noise from cooling pumping system. Two generally used cryogenic liquids are, liquid helium (4.2K) and liquid nitrogen (77K).

Another cooling system that was used in this ph.d thesis was Cryogenic probe station from Janis Research. The cooling mechanism of cryogenic probe station is based on Gifford-McMahon technology, which makes it possible to cool the sample down to $\sim 9.5\text{K}$ in our test. The advantage of cryogenic probe station is that all the cryogen is stored in a close loop. So no cryogenic liquids are lost in the measurement. However, the mechanical vibration from a cryogenic pump could be a problem when using normal tip probes.

In a measurement below liquid helium temperature, A He^3/He^4 dilution refrigerator was used in collaboration with other groups. The lowest temperature in

this work we reached is around 80 mK (0.08K). One concern about He³/He⁴ dilution refrigerators is that the He³ that is produced in a nuclear reaction is extremely expensive.

Chapter 5

Electronic measurement of a single CNT device

The electronic properties of a single carbon nanotube device was one of the most exciting research areas. It was also often considered as the driving force of carbon nanotube electronic applications [0]. Some researchers believed that carbon nanotube could be a possible replacement for traditional silicon based metal oxide semiconductor field effect transistors (MOSFET). One of the key reasons why a lot of reviews and journals are cited is the photo lithography's resolution limit. However, due to the development of sub-5 nm lithography technology in silicon industry, it seems that carbon nanotubes will not very likely replace silicon in the very near future.

In this chapter, I will introduce some of the fabrication experiments and measurements of a few single multiwalled carbon nanotube (MWNT) devices. For electronic measurement, we treat the MWNT device as a back gate field effect transistor (FET). Entities, such as named using conventional semiconductor jargon, are the drain-source current (I_{ds}), the gate voltage (V_g) etc.. These particular measurements are a minor side topic in my ph.d study, however, but the fabrication and measurement techniques are important for the work on CNT/hemicellulose that will be introduced in the next Chapter.

5.1 Single carbon nanotube backgated FET fabrication

MWNT materials in the shape of powders were obtained from commercial vendors or from the S.Iijima group at NEC/Japan. They were first made into dispersion with 1,2 dichloroethane (DCE) and were used for single MWNT backgated FET fabrication. These MWNTs are often semiconducting due to their modest diameter [38].

The concentration of the MWNT dispersion is from 1mg/ml to 0.1 mg/ml. Initially, most of the CNT were deposited in the bottom of the storage bottle. The dispersion was slightly agitated which would break the majority of the larger powder grains, after which the dispersion was transferred into a bath sonicator. Usually

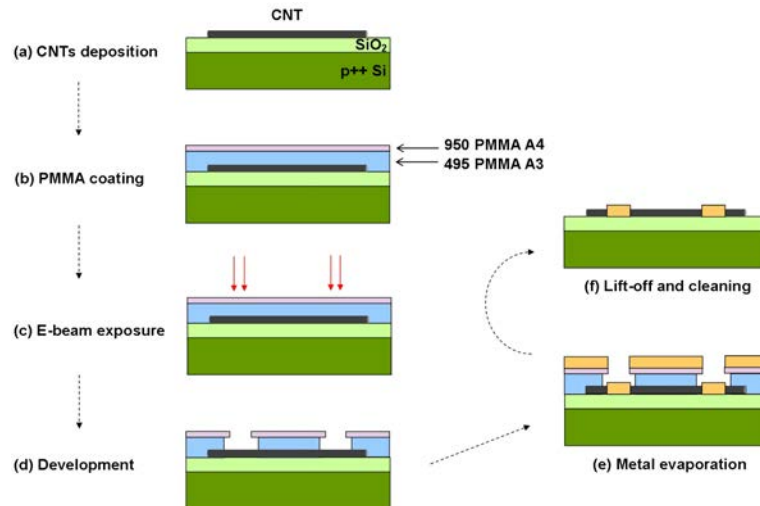


FIGURE 5.1 Backgated CNT-FET fabrication processes with routine processes used in our group. Reprint from [0]

the MWNT-DCE dispersion does not need very long sonication period. 30 mins to 2 hours is often enough. The dispersion can then be stored in room temperature for longer periods.

Standard backgated CNT-FET sample fabrication processes have been used in this thesis. The substrate used in the following experiments have 300/600 nm thermally grown silicon oxide with highly doped silicon as back-gate. The substrates were cut into 0.5 mm × 0.5 mm pieces, so they could fit into the chip carrier of low temperature measurement.

Two metal layers were fabricated with e-beam lithography for this experiment. The first layer consisted of bonding pads, larger electrode structures, and AFM markers for locating suitable MWNTs for measurement. The second metal layer were microelectrodes that directly connect the chosen MWNTs with the larger electrode structures of the first metal layer.

Commercial positive e-beam resists (PMMA) were used as masks for e-beam patterning. In order to form the undercut, which helps the lift-off process, a double layer of PMMA were generally used. The first layer was PMMA (poly(methylmethacrylate)) A3 495 dissolved in anisole, and the second layer PMMA A2 950. The resists were spin coated on the substrate with 3000 rpm for the first layer and 6000 rpm for the second layer. After each spinning the sample was baked on a hot plate for 2 mins to solidify the resist. The benefit of two layers of resist is to help combine the best e-beam resolution with good development.

For the first metal layer, 28 bonding pads and AFM markers were patterned as shown in Fig.5.2(A). The patterning was performed with Raith eline ebeam writer with 20 kV acceleration voltage and 500 micrometer writing fields. The aperture size used in the patterning of large bonding pads and 28 electrodes on the first layers were 120 μm. For smaller AFM markers (shown in Fig.5.2(A) red square) the

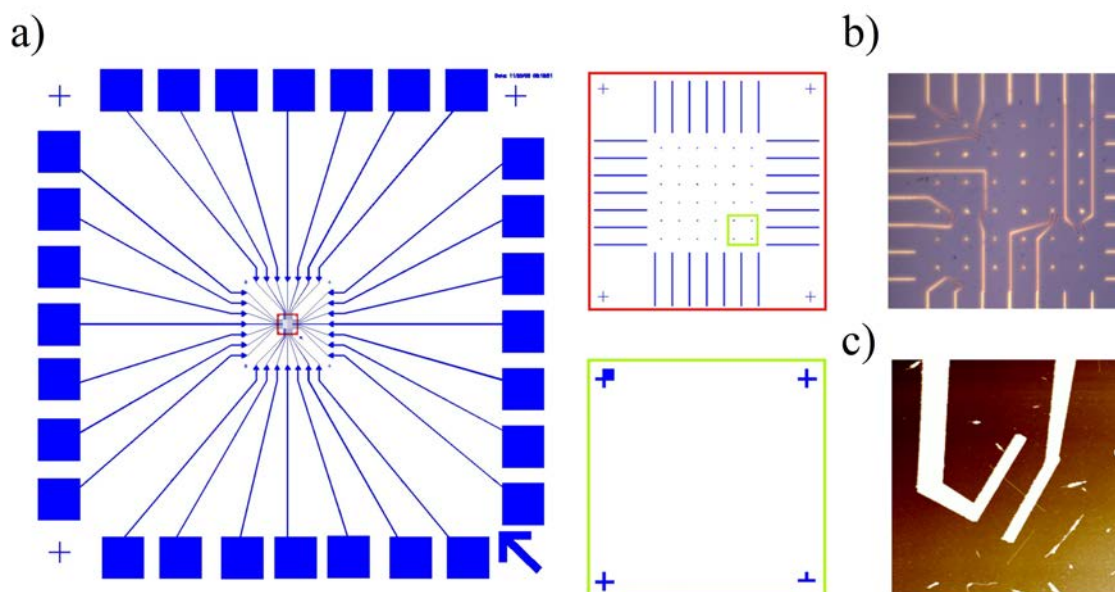


FIGURE 5.2 (A) Electron beam lithography mask used for a single MWNT carbon nanotube FET electrodes, inside of the red square show the inner electrode for second layer deposition; AFM marker inside the green square is 7 micrometer times 7 micrometer; (B) optical microscope image of real CNT-FET device after second layer deposition, on one chip, there are totally 7 single CNT-FET devices; (C) AFM image of a single MWNT CNT-FET device with scanning size of 2.5 micrometer

aperture size was $30 \mu\text{m}$. After ebeam lithography, the exposed patterns were then developed in 1:3 of MIBK (methylisobutylketone): IPA (isopropanol) for 45 s. After rinsing with pure IPA, the sample was dried with nitrogen air gun for additional RIE cleaning. This additional RIE cleaning is generally helpful to improve the yields of sample fabrications, as some large PMMA might not be that easily removed during the development process. The recipe for extra light PMMA cleaning was: 30 s, 50 sccm oxygen flow in 40 mTorr pressure, 30 Celsius, 60 W with Oxford Instruments Plasmalab80 Plus RIE. The evaporation was done with UHV (Cry-torr 8, Telamark TT10) evaporator with liquid nitrogen cooling system. For the first layer patterns, 30 nm gold with additional 5 nm Ti sticking layer was used.

Carbon nanotubes were then deposited on the substrate with spinning method. The amount of the carbon nanotube materials on the substrate depended on the density of CNT/DCE dispersion and spinning speeds. After carefully choosing the spinning speed and concentration of the CNT solution, it is possible to have around 10's of CNTs on $45 \mu\text{m} \times 45 \mu\text{m}$ AFM location area (Fig.5.2(A) red square).

On the $45 \mu\text{m} \times 45 \mu\text{m}$ location areas, there are 6×6 AFM markers with separation of $7 \mu\text{m}$ of each other. The pre-spin CNT were then located with AFM (Veeco Demension 3100 and Bruker Icon) using the tapping mode or peakforce mode. The scanning size of the Bruker Icon is large enough for a single frame scanning of all the CNTs. This gives some advantage in the second layer patterning.

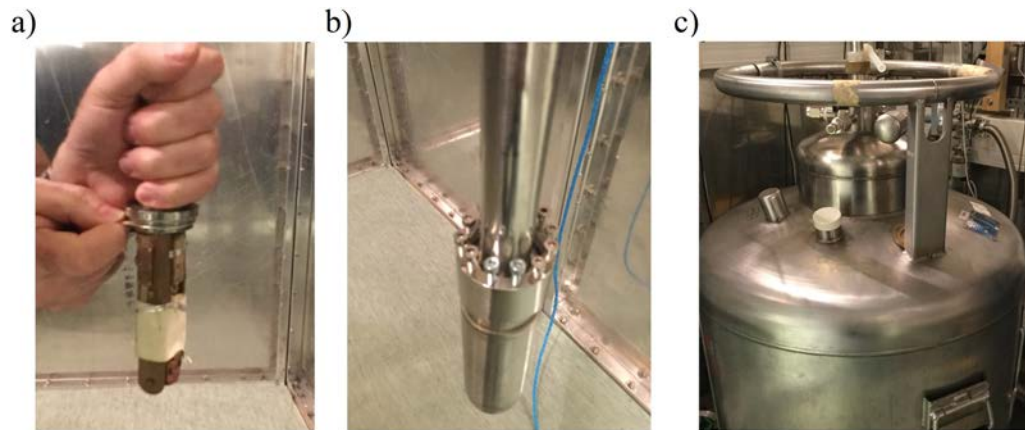


FIGURE 5.3 Low temperature measurement setup: (a) vacuum sealing with indium; (b) vacuum can and cryostick for low temperature measurement; (c) cryostick in liquid helium tank for low temperature

Second layer patterning was done with the similar processes as the first layer deposition. Since much smaller patterning features were needed (30 nm patterning line etc), 6.5 or 10 μm size aperture of electron beam was generally used. The working area for patterning was also shrunk to 100 μm . For second layer patterning, RIE treatment is a must, since undeveloped PMMA on the surface of CNT can easily break the Schottky contact of the electrode pads to CNT. For metallization of the second layer patterning, Pd layer is considered to be the best for CNT contact due to the similar working function. However, Pd layer has a poor affinity to silicon oxide, which significantly reduces the yield of the manufacturing processes. So in this experiment, Au or Au with Ti sticking layer were adopted. AFM images of the backgated CNT-FET devices are shown in the Fig.5.2(B-C).

5.2 Conductivity measurements setup

The sample was attached into a 28 channel chip carrier with varnish and aluminum measurement wires were attached to it with a wire bonder. The bonded sample was then transferred into a homemade dipstick in vacuum inside a EM shielding room.

The measurement setup with two terminal measurements for CNT-FET is shown in Fig.5.4. The voltage supplies used in these experiments were two programmable DC voltage sources (Yokogawa 7651), one for source-drain and the other one for gate voltage control. The input and output signals were measured with a 18 bit data acquisition (DAQ) device (National Instruments PXI 1031 M) and controlled via Lab-View through optical fiber. Stanford SR570 I/V preamplifier was used as a current amplifier for DC current measurement. Lakeshore Standard Curve 10 Thermometer which was inside the measurement vacuum can, was constantly measuring with a 4 probe measurement system or resist bridge for temperature measurement. For the

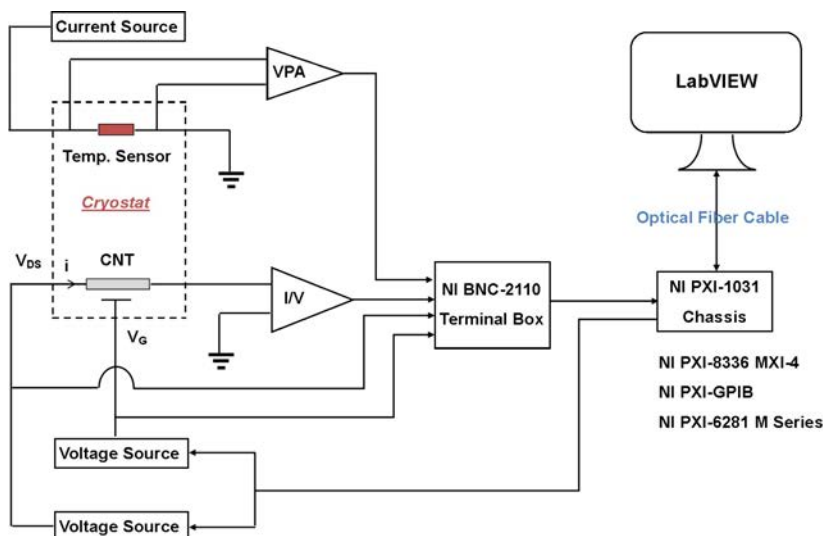


FIGURE 5.4 Schematics of the DC measurement setup used for the CNT devices. Source-drain voltage and gate voltage are controlled by LabView software. VPA and I/V stand for voltage- and current preamplifiers, respectively. Reprint from [0]

two DC voltage sources, the maximum voltage supply is 30V.

5.3 Conductivity measurement at different temperatures

As was discussed in Chapter 2, MWNTs can show either metallic or semiconducting behavior depending on the outer shell chirality (and also diameter). For metallic MWNT, where the Fermi level is in between the conduction band and valence band, the electric field has little effect on its conductivity. The conductivity of a semiconducting MWNT, on the other hand, could be strongly modified with an electric field from a nearby gate electrode, provided that the bandgap is larger than the thermal energy. This could be seen in a CNT as a field effect transistor, or CNT-FET.

In a CNT-FET, one has two electric fields associated with electron transport; the drain-source biasing electric field (V_{ds}) and the electrostatic gating field (V_g). The bias voltage (V_{ds}) yields electron propagation along the nanotube, which also defined the chemical potential between the left and right side of the device. The gating voltage acts to lower or raise the band gap edges of a semiconducting nanotube with respect to the Fermi level of the metal contacts. The negative gating voltage (Fig.5.5(b) p-type), tend to align the Fermi level with the valence band, therefore promoting hole conductivity. On the hand, positive gate voltage (Fig.5.5 (b) n-type), tend to move the conduction band towards the Fermi level thereby promoting electron injection leading to n-type behavior.

Fig.5.6 shows typical I_{ds} - v_{ds} relationship of a CNT-FET with zero gate voltage at different temperatures. For a metallic CNT (Fig.5.6 (a)), at room temperature, there is linear I_{ds} and V_{ds} relationship, as pure resistor following ohm's law. How-

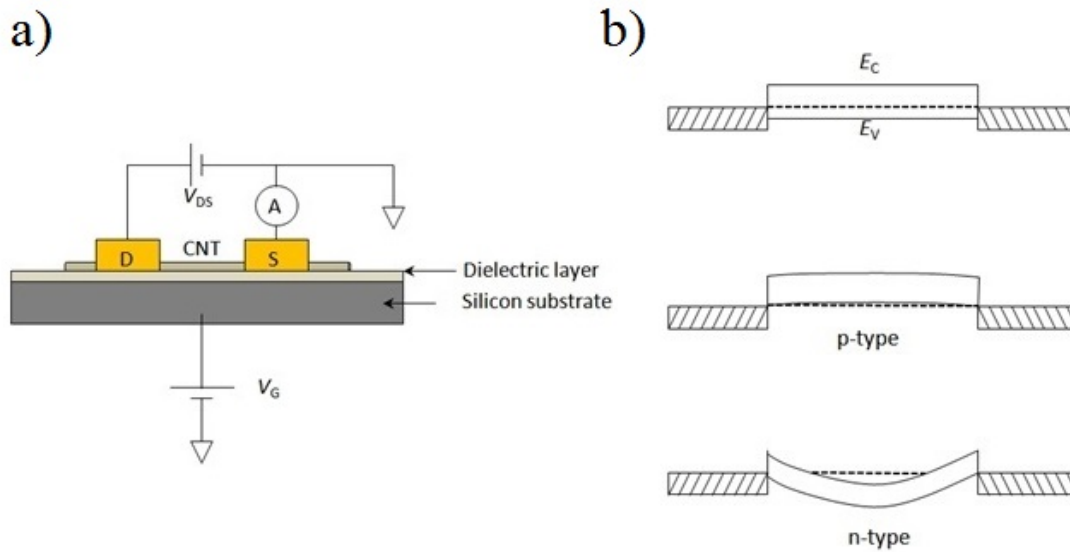


FIGURE 5.5 CNT-FET. (a) Schematic of a CNT-FET device. A CNT is connected to source (S) and drain (D) microelectrodes. The gate electrode is connected to the doped silicon, in a so called backgate configuration. (b) An energy diagram of a semiconducting CNT between the S- and D-electrodes, and under the influence of positive and negative gate voltages. Reprinted from [37]

ever, it is easy to see that at low temperature, there are some non-linear behavior at I_{ds} and V_{ds} figure. At room temperature, the conductance of this metallic MWNT is $3.9 \times 10^{-5} S$ which is about twice the conductance quantum ($2 G_0$). This experiment indicates that electrons pass through the source to drain channel with nearly ballistic behavior.

For a semiconducting MWNT (Fig.5.6(b)), we can clearly see non-linear I_{ds} and V_{ds} behavior. As there is a band gap between the conduction band and valence band, the gate voltage can set the semiconducting CNT into a "on state" or an "off state". The band gap might not be easy to see at room temperature (as it is shown in Fig.?? (b)) due to the Fermi tail. Another possible explanation is from our sample fabrication, as we used backgated field effect design, the measurement band might not be at the same level as the band gap (as it is shown in Fig.??(b), where band gap for 295K and 77K are not at $V_g = 0$).

Fig.5.6 shows typical i_{ds} - v_g relationship with constant bias v_{ds} at different temperatures. For metallic CNT (Fig.5.6(c)), the gate voltage has little effect on the electron transport behavior from room temperature to liquid helium temperature. A weak I_{ds} - V_g relationship peak could be seen at liquid nitrogen or liquid helium temperatures, but the on/off ratio is very small (in the same magnitude of order).

On the other hand, a semiconducting CNT (Fig.5.6(d)) has a much stronger behaviour at different temperatures. The on/off ratio is more than 4 orders of magnitude larger. One of the drawbacks of the backgated CNT-FET is that the off V_g is not necessary at 0 bias. This, however, shows no properties of the band gap of the

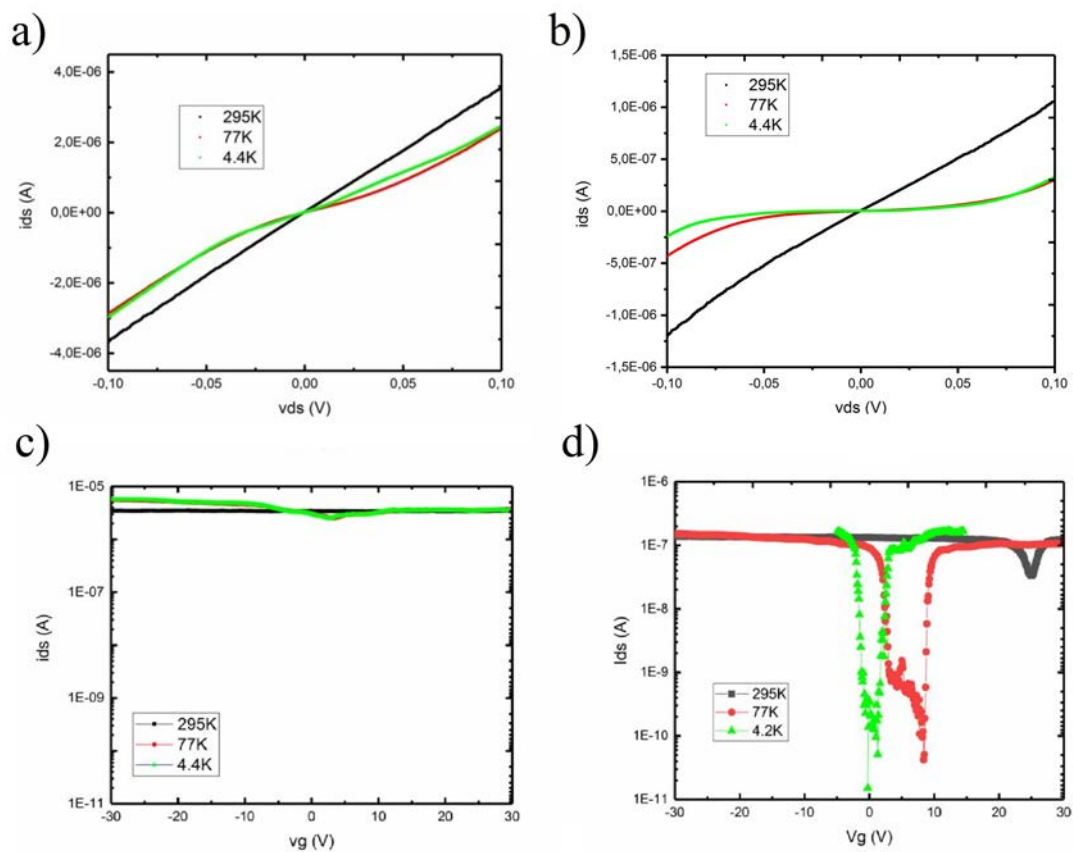


FIGURE 5.6 Conduction data that has been measured at the three indicated temperatures; a-b) I_{ds} vs. V_{ds} relationship at $V_g = 0$ of (a) metallic MWNT, and (b) semiconducting MWNT; c-d) I_{ds} vs. V_g relationship ($V_{ds} = 0.1$ V) of (c) metallic MWNT; (d) semiconducting MWNT.

44

channel.

Chapter 6

Electronic and optical properties of thin films of carbon nanotube/hemicellulose complex

Carbon nanotube/hemicellulose mixtures are usually regarded as composites, where cellulose forms the host matrix and CNTs as filler material to enhance the electrical and thermal conductivity. Here I describe a new material made of double walled carbon nanotubes and hemicellulose (CNT/hc), where the function of the hemicellulose (xylan) is to enable dispersibility in water of the CNTs. The CNT/hc complex forms a very stable dispersion after sonication, which can stand at best for several years if stored properly. Different measurements, low temperature conduction, Kelvin probe, THz conductivity, dynamical light scattering, UV to Far-IR range optical spectrometry etc., have been used to systematically analyse its conductive and optical properties.

6.1 Preparation of CNT/hemicellulose dispersion and its property

Double wall carbon nanotube/hemicellulose dispersion (CNT/hc) was prepared following the patent of XYNAC Inc. The DWNT materials were purchased from Unidym Co. (USA) ¹, with an average length of 2 μm , diameters in the range 2 - 3 nm, and purity of > 50 wt%. The commercially obtained xylan, that is the hemicellulose (hc), was an extract from beech tree ².

CNT/hc dispersion was prepared as follows: (a) 100 portions of DWNT and 1 portion 2-propanol mixture in 100 portions pure water; (b) sonication 1 min with 300W finger sonicator; (c) 100 portions of Xylan added into the DWNT dispersion

¹Unidym Inc, Sunnyvale, CA, USA

²Symrise Bio Actives GmbH, Hamburg, Germany

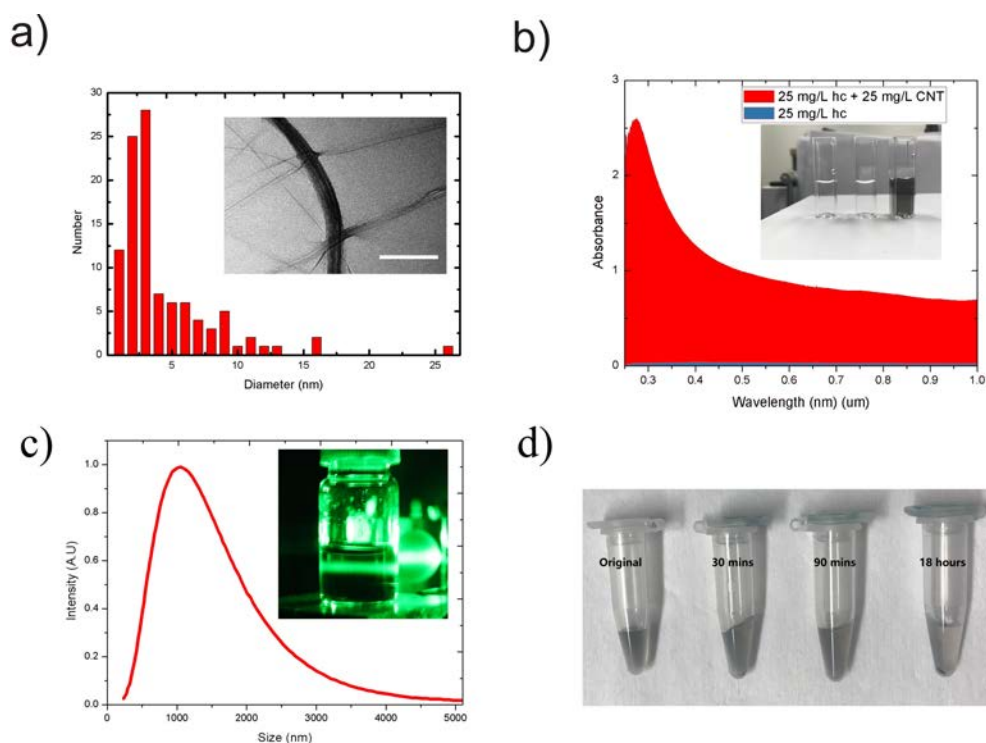


FIGURE 6.1 (a) Diameter statistics of individual or bundles of CNT/hc as measured with AFM; Inset: TEM image of individual and bundles of CNT/hc, scale bar 100 nm; (b) Absorption spectrum of 25mg/L pure hemicellulose and 25 mg/L CNT/hc, Inset: optical image of pure water, hemicellulose, hemicellulose + CNT (c), Dynamic light scattering of CNT/hc solution with average particle size of 1.2 micrometer, Inset: Tyndall effect with clear light pass with 520 nm laser; (d) CNT/hc dispersion centrifuged for 10 mins, 30 mins, 90 mins and 18 hours with 2000g. [0]

by 4 times, each 25 portions. The separation time of adding Xylan is 4 mins, with continued finger sonication.

The diluted dispersion exhibited no sign of re-deposition at +4 °C for several years. The exact properties of hemicellulose in the dispersion is still unknown or under debate. Some theory predicts that hemicellulose chain is wrapped along the CNTs while some other models treat the hemicellulose as an ordinary dispersant.

We used different methods (Dynamic light scattering, centrifugation, Tyndall effect with green color laser, AFM, SEM, TEM etc.) to analyze the properties of the solution.

Fig.6.1 shows some basic properties of the CNT/hc dispersion. Fig.6.1 (a) shows statistics as measured with AFM, of the diameter of individual CNTs complexed with hc. It clearly shows that most CNT/hc complex have a diameter smaller than 5 nm, which could very likely be individual CNTs with hc wrapping. For an individual complex, some diameter are larger than 5 nm, which are likely bundles of CNT/hc tubes. This is also confirmed by the TEM analysis, which is shown in Fig.6.1 (a)-Inset. Fig.6.1 (b) shows the absorption spectrum of 25mg/L hemicellu-

lose with and without 25 mg/L DWCNT. This clearly shows that for same amount of CNT and hemicellulose, the majority of the absorption in the UV to near-IR range comes from the CNT component. Fig.6.1 (c) shows the DLS experiment. The result implies that the hydrodynamic radius of the particles in the dispersion is around 1 to 2 micrometer sizes, which prove that CNT/hc dispersion should be considered as a colloid instead of a solution. This is also proved in the inset by the Tyndall effect, where a very clear laser path could be observed. Fig.6.1 (D) shows a series of centrifuge experiment with 2000 g acceleration. Clear re-deposition only happen after 1 hour centrifugation, which in another way, prove the stability of the CNT/hc dispersion.

6.2 CNT/hc thin film fabrications

Many different measurements, that required different kinds of samples, have been undertaken (in those that were performed abroad, the author has mainly participated in the planning and sample fabrication). Information on the different fabricated samples is given in Fig. 6.2. More details of the measurements and samples of each kind will be described below.

Macroscopic CNT/hc thin film for DC measurement (Case (a) in Fig. 6.2)

Macroscopic CNT/hc thin film was made by low speed spinning or drop-dry casting the dispersion on pieces of silicon with four point measurement electrodes first fabricated. These electrodes were of 30 nm Au with 5 nm titanium as sticking layer, and were made with normal e-beam lithography. The silicon used was commercially purchased with 300 nm silicon oxide as insulation layer. The silicon substrate was highly doped, and could be used as backgate electrode at low temperature.

Before drop-dry casting, we found that it is helpful to first hydrophilize the silicon oxide surface with O₂ plasma treatment to improve the homogeneity. The thickness of the thin film was measured by AFM on a sharp edge which was cleaned by a wet cotton stick (shown in Fig.6.3(a)). With drop dry casting, the density of the CNT/hc thin film is high and is therefore continuous.

CNT/hc thin film on microelectrodes - DC meas. and KPFM ((b) in Fig. 6.2)

Microelectrodes for 2 point measurement, shown in Fig. 6.4, were fabricated with e-beam lithography. With normal deposition the microelectrodes were coated by a continuous CNT/hc film and such samples were used for KPFM measurements. With fast spinning of the CNT/hc dispersion on silicon surface, one can deposit micron size CNT/hc network fragments on microelectrodes, with only few CNTs. Using the fastest spinning speeds (usually above 6000 rmps) and dispensing small amounts of dispersion was necessary for successful fabrication of individual tubes

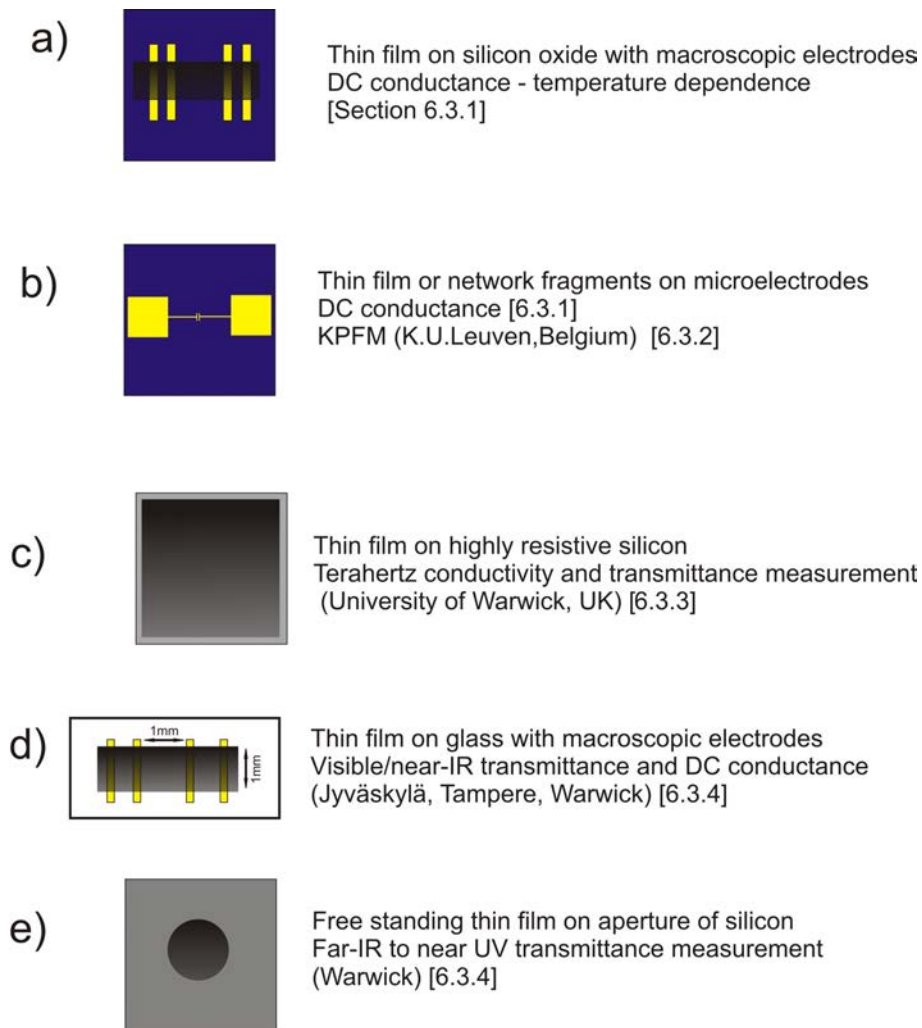


FIGURE 6.2 Schematic illustration of fabricated CNT/hc thin films samples, and the measurements on them indicated. In parentheses location, if not at the Univ. of Jyväskylä. In square brackets is indicated section of the corresponding experiment.

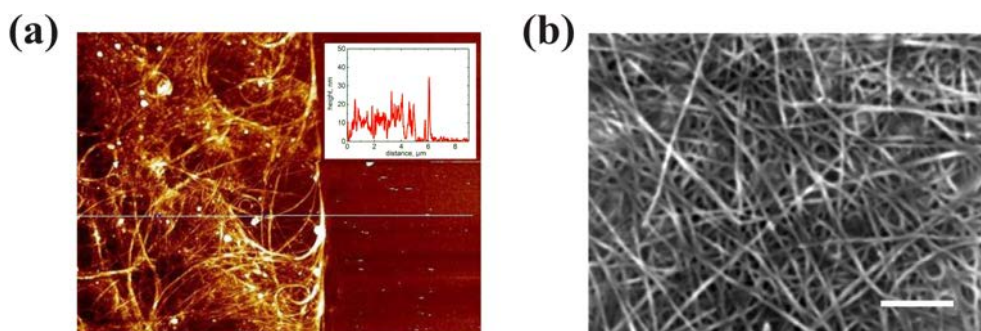


FIGURE 6.3 (a) AFM image of spin coated CNT/hc films, where the sharp edge has been created as explained in the text. The inset shows height profile data across the edge along the line superimposed on the AFM image. (b) SEM images of macroscopic CNT/hc thin film. Scale bar 200 nm.

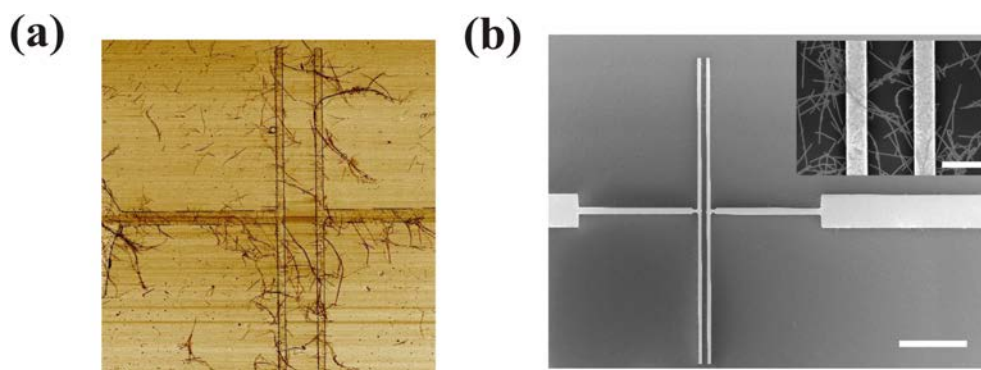


FIGURE 6.4 (a) AFM and (b) SEM image of microelectrode structure for measuring CNT/hc network fragments. Scale bar 10 μm . Inset: Close-up electrodes with tubes visible. Scale bar 3 μm

and fragments of CNT networks. AFM and SEM images of CNT/hc thin films of network fragments on silicon oxide are shown in Fig. 6.4.

CNT/hc thin film on high resistive silicon for Thz measurement ((c) in Fig. 6.2)

Terahertz frequencies conductivity measurement was done on plain Si substrate, on which CNT/hc was drop-dry deposited. The Si substrate was highly resistive float-zone silicon [11], which does not absorb Thz radiation. The thickness of the CNT/hc films used were 130 nm, 470 nm and 1170 nm.

Optical measurement on CaF₂ and glasses ((d) in Fig. 6.2)

For optical measurement, CNT/hc thin film samples were prepared on glass microscope slides (Thermo Scientific Menzel-Glaser). For 4-Probe measurement electrodes with 1 cm separation were prepared with vacuum deposition systems. The electrodes consisted of 5 nm thick titanium layer and 120 nm gold layer, where titanium acted as adhesive between gold and glass.

The CNT/hc thin films were prepared with 2 different methods: spray-coating and vacuum filtration.

In spray-coating, the solution was sprayed on the substrate with an airbrush while the substrate was heated on a hotplate at 200 Celsius.

In vacuum filtration, the vacuum was used for sucking the solution through a filter, whereby CNT/hc forms a thin film on the filter. Mixed cellulose ester (MCE) filters from Merck Millipore, with 25 nm pore size and 25 mm diameter, were used. The CNT/hc thin films with a bit of moisture could be easily peeled off by lowering them into water at 45 degree angle (Fig.6.5(a)). The water interface peeled off the CNT/hc film, leaving it floating on the surface from where it was collected on a glass substrate. Some membrane particles could also be found under CNT/hc thin films. Another method used to collect CNT/hc thin film after filtration was to dissolve

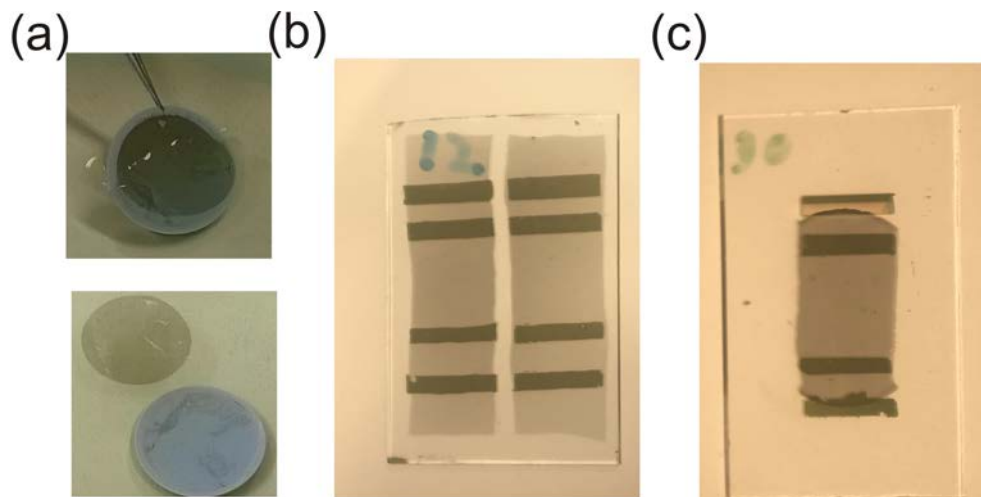


FIGURE 6.5 (a) Removal of CNT/hc thin film off the filter membrane with water and the thin film was then floating on the surface; (b) Prototypes of CNT/hc thin films with spraying and vacuum filtering

the filter while pressing it and the CNT/hc film against the substrate, which is a common method for transferring vacuum filtered films. However, we found that yields of successful CNT/hc thin films was low: CNT/hc thin films were more likely to tear during the dissolution processes.

We also prepared CNT/hc thin films samples on CaF₂ windows for infrared spectrum measurement. The cleaning and deposition methods were similar to visible light CNT/hc thin film.

Free standing thin film for optical measurement ((e) in Fig. 6.2)

One “free standing” sample on a 4 mm aperture was prepared for the whole range (Thz to UV) test. The “free standing” CNT/hc thin film was first prepared with droplet-dry method on silicon substrate. This substrate was then dipped into 1M concentration NaOH solution, which left a loose packaged CNT/hc thin film floating on the solution. As soon as the exfoliation process was achieved the film was immediately transferred into deionized water and soaked for 1h. After that the film was cut and gently stretched on the aperture (with 4 mm in the diameter). One piece of the same film was put on the Si substrate for the thickness measurement.

6.3 Experiment

6.3.1 DC measurement: Temperature dependence

The low temperature conductivity was measured as explained in Chapter 5.2. For the measurements we used a 4K He-bath cryostat with the sample inside a closed

vacuum can. To measure our sample at subKelvin temperatures ranging from 0.08 K to 4K, a home-built plastic He₃ and He₄ dilution refrigerator (PDR) was used. The resistance of the sample and thermometer were measured with a Picowatt AVS-47 resistance bridge with an excitation of 50 μ V with four probes method. A resistive heater was directly attached to the sample mount to sweep the sample temperature slowly from 80 mK to 4.2K.

For very low conductance (sub-kelvin) measurement, a so called "Double lock-in measurement" method was used. A small sine wave form excitation voltage with about 1.1 Hz frequency has been fed into the sample, and the response voltage and current across the sample are measured by using lock-in technique with four terminal method through two Stanford Research System SR830 lock-in amplifiers. During the experiment, the sample is measured first with cryostat self-cooling from 4.2K to about 400mK, and then measured again with the cryostat slowly heating up to 1.5K by using the on stage heater.

High temperature resistance measurement from 295K up were made in a home-made vacuum chamber (10^{-3} mbar) with Labfacility element 14 platinum resistance thermometer. The heater used in this experiment was AZ5W1R5% cement resistor with DC power supply HY3005D-2. The resistance of the sample and thermometer was measured with the Picowatt AVS-47 resistance bridge.

6.3.2 Kelvin probe atomic force microscope measurement

The KPFM measurements were done in K.U. Leuven, Belgium (Dr. A. Volodin), using an Agilent 5500 Scanning probe microscope, on the microelectrode structures shown in Fig. 6.4. The principle of KPFM was briefly explained in the facility chapter. Very quickly summarized, when a conducting AFM tip (Pt/Ir coating in our case) gets close to the conductive sample, they form a capacitor. This capacitor is very sensitive to the surface potential changes (contact potential difference CPD), by adjusting the tip to sample voltage to the contact potential difference, one can obtain a surface potential map which corresponds to the surface functions between the two subjects on the surface. These experiments were done in a so called single pass double frequency mode [34]. The bias between the tip and the sample used here was 1.5 V. A probe with evaluated tip apex radius of $7 \text{ nm} \pm 2 \text{ nm}$ was used from PPP-EFM probes (Nanosensors) with Pt/Ir conductive coating. All measurements were carried out under dry N_2 atmosphere. During the measurements a voltage of $\pm(1 - 6) \text{ V}$ is applied between the CNT-hc device electrodes.

6.3.3 Terahertz conductivity measurement

Terahertz conductivity measurement on macroscopic CNT/hc thin films can yield information on intra-tube and along CNT tube conduction processes. Terahertz time-domain spectroscopy was used to measure the THz radiation transmitted through

the CNT/hc films by the collaborating group at the University of Warwick, UK. The complex, frequency-dependent conductivity $\sigma(\omega) = \sigma_1(\omega) + i\sigma_2(\omega)$ of the CNT-hc films was calculated from

$$\sigma(\omega) = \frac{1 + n_s}{Z_0 \delta} \left(\frac{1}{T(\omega)} - 1 \right) \quad (6.1)$$

where n_s is the refractive index of the silicon substrate, Z_0 is the impedance of free space, δ is the thickness of the film and $T(\omega)$ is the experimental complex transmission [31]. The effective conductivity of the CNT-hc film was obtained over a frequency range from 0.2 THz to 2.5 THz, limited by the bandwidth of the THz pulses detected. Transmission spectra were also obtained from 6.0 THz to 20.0 THz using a commercial FTIR to better constrain the absorption of the CNT-hc films.

6.3.4 Optical measurement: transmittance from near UV to far IR

These experimental facilities for the optical transmittance measurements of CNT/hc samples are listed in Tab. 6.1. Besides by the author, work was done by M.Sc. Hannu Pasanen (University of Jyväskylä and Tampere University of Technology), and M.Sc. Maria Burdanova at University of Warwick.

TABLE 6.1 Instruments used for transmittance experiment of CNT/hc thin film

Wavelength (nm)	Instruments
250-1500	UV-Vis-NIR spectrophotometer Lambda 1050
370 - 1100	Cary 8454 UV-Vis Diode Array system
700- 1160	Nicolet Magna IR -760 ESP FTIR (with white light source, Si detector with CaF2 beamsplitter)
850- 3571	Nicolet Magna IR -760 ESP FTIR (with Ever-Glo white light source, MCT-A detector with quartz beamsplitter)
7500-30000	TDTS setup with photoconductive antennas, Ti:sapphire laser
75000-2000000	Fourier transform infrared spectroscopy (FTIR, Bruker)

6.4 Results

6.4.1 DC measurement

The temperature dependent conductivity of macroscopic samples with thickness (8 nm to 40 nm) is shown in Fig.6.6(a). At room temperature, the conductivity of thick CNT/hc films is quite high up to 2×10^3 S/cm. The conductivity drops very quickly when they are cooling below 50 K. For macroscopic samples, we did not observe any non-linear drain current response at liquid helium temperature, which therefore is Ohmic as in a normal resistor. The thickness of CNT/hc samples affect their conductivity and dependence on temperature and humidity (Table.6.2.). As is shown in the table, we use conductivity ratios from the temperature and humidity dependences to characterize the measurement results. It clearly shows that in general, thinner CNT/hc thin films have stronger temperature and humidity response.

We also did several sub-Kelvin measurements of the macroscopic samples. As it is shown in Fig.6.6(a)-Inset, the conductivity of AJ2 sample drops from 1.6 k Ω (at room temperature) to 36 M Ω (at 0.3K). There difference of resistance is larger than 20000 times, which clearly indicates very low conductivity at absolute zero temperature.

TABLE 6.2 Relative resistance dependence on sample thickness and their thermal and humidity stability

Sample name	Sample thickness ³	$\sigma_{300K} / \sigma_{4.2K}$	$\sigma_{90\%} / \sigma_0$ ⁴
AM2	8 nm	16.3	6.1
AJ1	12 nm	13.7	1.9
AM3	12 nm	8.4	1.9
AM1	20 nm	4.6	1.9
AF1	20 nm	3.8	2.2
AF2	40 nm	4.6	unknown
AN1	100 nm	unknown	1.9

At liquid helium (4.2K), the network fragment samples with only a few CNT connecting across microelectrodes (Fig.6.6(b)), clearly show some non-linear behavior (Fig.6.6(b)). A clear gate effect on the transport of these mesoscopic samples (Fig.6.6(b)-black figures), is similar with a single CNT field effect transistor response with a semiconducting tube.

Fig.6.6 (c) shows a measurement of the stability of the CNT/hc thin film at higher temperature in vacuum. As shown in the inset, the sample was repeatedly heated up to ~ 140 Celsius for 15 mins, and allowed to cool down for another 15 mins. In total 50 cycles were done in 25 hours. The resistance of the samples was recorded by a resist bridge that was connected to the computer. In the resistance and heat cycling relationship analysis (Fig.6.6 (c)), it clearly shows that at first few cycling, the resistance increased from 2.6 k to 5.3 k after 4 cycles, after which the

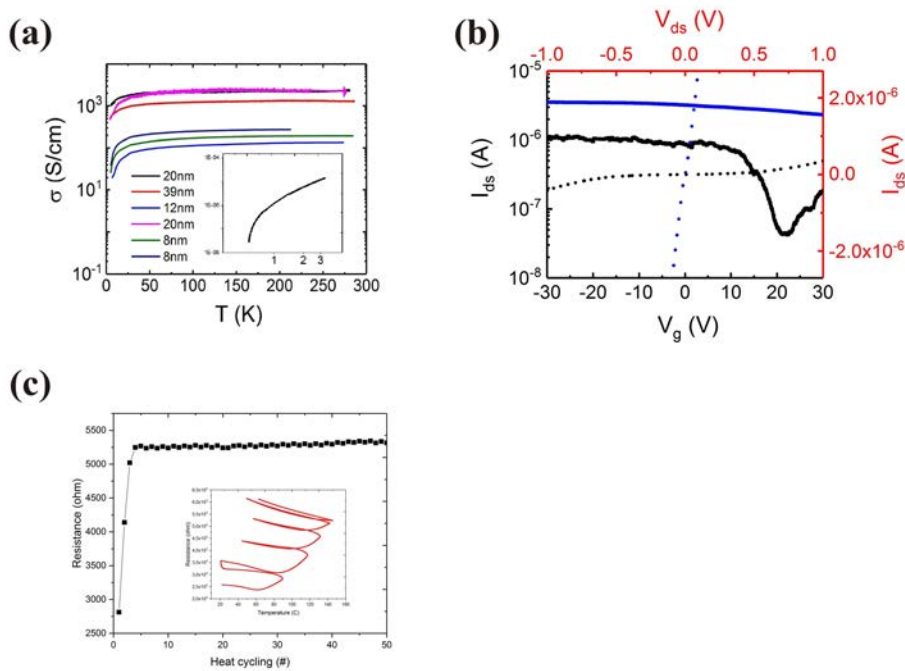


FIGURE 6.6 (a) Temperature dependence of conductivity of CNT-hc films with different thicknesses. Inset: 0.3 K data in log scale of the 12 nm sample. (b) Low temperature ($T = 4.2$ K) measurements of I vs V_{ds} (top and right axis, red color) and I vs V_g (bottom and left axis) of two typical CNT-hc network fragments. Electrode separations were $3 \mu\text{m}$ (black line) and $5 \mu\text{m}$ (blue line). (c) CNT/hc heat annealing process (in set) and temperature stability with high temperature for 50 heat cycles (25 hours) in vacuum.

resistance becomes stable with a slight increase during 25 hours. A careful analysis of the heating process with resistance (shown as the inset of Fig.6.6 (c)), indicate a complex processes of the heating annealing, where the resistance slightly drops and then increases. It clearly shows in the first few cycles, that the resistance and temperature curves do not overlap, which could indicate some structural modification of the CNT/hc thin film itself. After 5 cycles, the resistance and temperature curves become one curve, with resistance lowering with temperature increasing. This is a good indication that even at higher temperature that the CNT/CNT junctions are still the dominant factor for the transport conductivity.

6.4.2 Kelvin probe atomic force microscopy

The Kelvin probe atomic force microscope could measure the topography and electrical potential maps of the CNT/hc surface at the same time. From the topography of CNT/hc images (Fig.c and 6.7(a)), it clearly shows that with hydrophilic treatment assist method, it is possible to fabricate a uniform CNT/hc thin film. The average length between the crossings of CNTs is around 0.6 micrometers.

For the electron potential measurement, it can be better understood if we sepa-

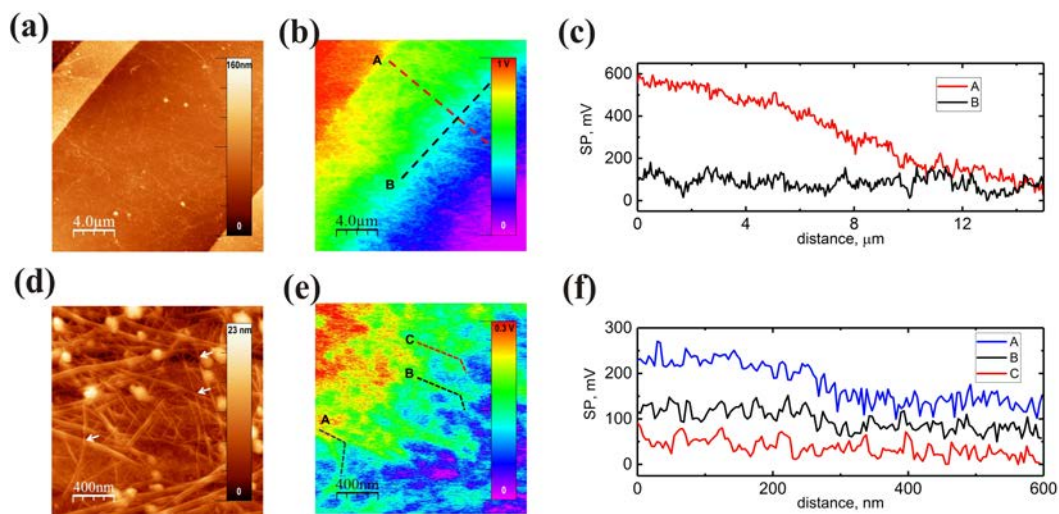


FIGURE 6.7 $20 \times 20 \mu m^2$ AFM topography (a) and KPFM surface potential (SP) images of the CNT-hc device in the current carrying state (b). Local surface potential profiles (c) taken across the dashed lines. The profile curves have been vertically offset for clarity; Higher resolution $2 \times 2 \mu m^2$ AFM topography (d) and KPFM surface potential images of the CNT-hc device in the current carrying state (e). The profile curves have been vertically offset for clarity. Local surface potential profiles (f) taken across the dashed lines in (b). The white arrows in (a) indicate the (tube-tube) contacts at which the potential drops occur.

rate the discussion into two, the large scale (20 μm , Fig.6.7(b)), and the small scale (2 μm , Fig.6.7(e)). On the large scale, the potential drop perpendicular to the electrode (red line in Fig.6.7(c)) is almost linear. The potential drop parallel to the electrodes (black line in Fig.6.7(c)) could be neglected. This phenomenon could be simply understood by 2D isotropic properties with homogeneous CNT distribution in different directions.

On the other hand, on the small scale KPFM measurement, which give some hint for conductivity mechanism about CNT/hc thin film. Fig.6.7 (e,f) clearly suggests that most of the voltage drop happens on the CNT-CNT junctions. Along one individual CNT, the potential drop is much smaller (Fig.6.7(c)). The measurements strongly suggest that at the microscopic level the voltage drop in crossed current-carrying CNTs concentrates to the tube-tube contacts.

6.4.3 Terahertz conductivity measurement

Figure 6.8 a) and b) shows the complex conductivity $\sigma(\omega)$ of the films with the thicknesses 130 nm and 470 nm, respectively. The real conductivity σ_1 (blue points) at

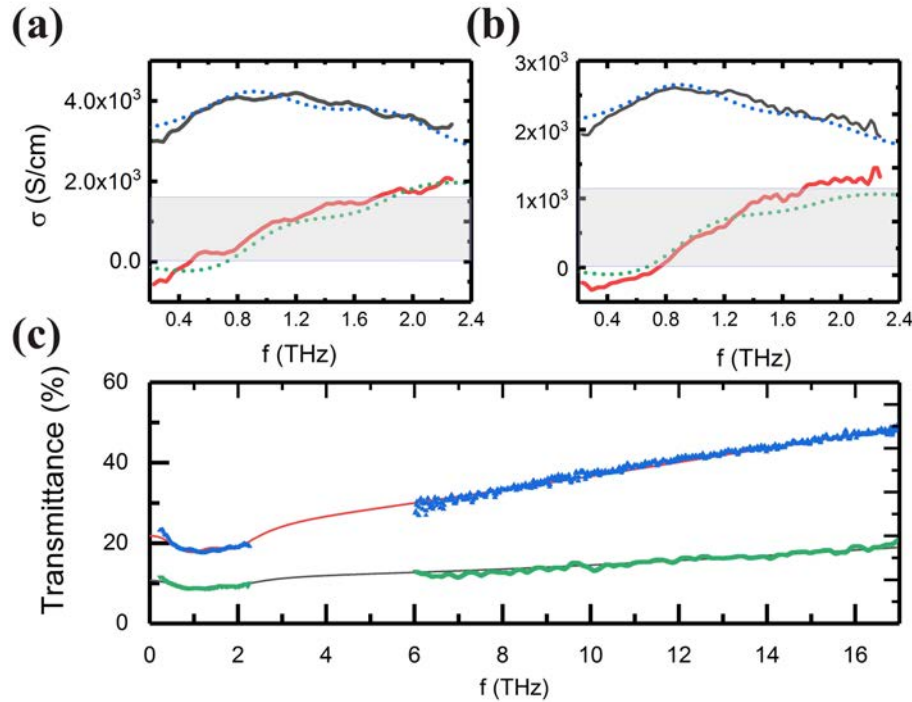


FIGURE 6.8 (a) Real (black lines) and imaginary (red lines) conductivity of a 130nm CNT-hc film. (b) Similarly, for the 470nm film. The dashed lines are fits as described in the text. The blue shaded areas show the contributions of the Drude term to the real part of the conductivity. (c) Measured (blue and green points) and modelled (red and black lines) amplitude transmission spectra from THz-TDS (left) and FTIR (right).

room temperature for the 130nm film has a weak frequency dependence, with a broad resonance peak. The DC limit to σ_1 is around 2000 S/cm, in agreement with the DC conductivity result of Fig.6.3.

6.4.4 Transmittance of thin film from UV to far IR

In order to understand the relationship between transmittance and different electromagnetic wavelengths, a wide spectrum (0.29 μm to 300 μm range) was measured with different methods on different samples. From Fig.6.9(a), we can clearly see that on large scale, generally, the transmittance of CNT/hc sample increases as EM frequency increase. This has been observed quite often for pure CNT thin films. [REF]. The maximum transmittance happened at 3 μm wavelength, with transmittance almost 97 percent. Above that the transmittance started decreasing. Most EM energy is lost under 3 μm range, with two mechanisms. The first one is the plasmon resonance along the axial of the CNTs, and the second one is the energy absorption of E11 and E22 transmission (Fig.6.9 (a) and (b))⁵.

⁵E11 and E22 are the 1st and 2nd optical band-to-band transitions.

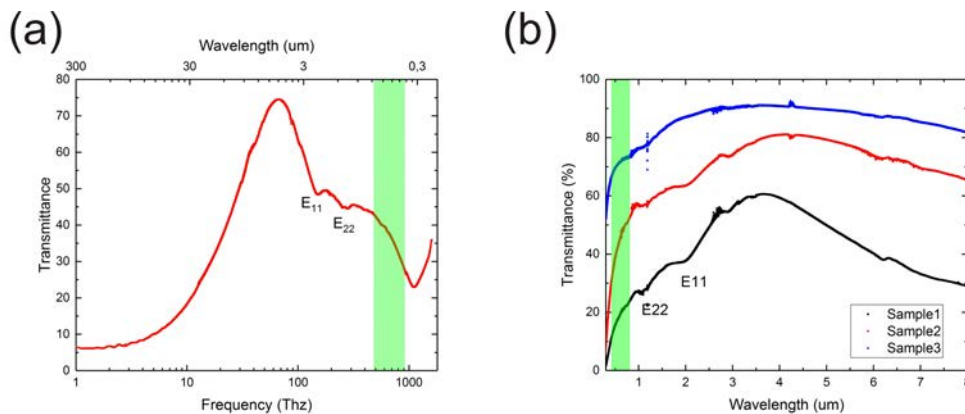


FIGURE 6.9 (a) CNT/hc thin film transmittance at different wavelength. For UV to Near IR range, thin sample (around ~ 20 nm) and thick sample (~ 500 nm) was prepared on CaF₂. For FTIR and terahertz time domain spectroscopy, our old published data on high-resistivity float zone silicon, with thin sample (~ 100 nm) and thick sample (~ 500 nm) [0]. (b) Transmittance fraction of EM spectrum in UV/Vis/Near-IR range, with highlighted red and blue color in visible light range. Blue color indicates the fraction of transmittance, red color indicates the absorption or reflection part of the EM in visible light range

6.5 Discussions

Some basic aspects of the mechanism behind the conductivity measurements could be understood by considering the CNT-CNT coupling as a hetero- or homojunction. These are semiconductor terminologies which describe the possible junctions formation when two semiconductors pieces (by different doping) connect. For analysis of CNT thin film transport, the definition is related to the bandstructure. In principle, of unsorted single walled CNTs, 2/3 are semiconducting (S), and 1/3 are metallic (M). From two CNTs, three possible junction types are Metal-Insulator-Metal (MIM), Metal-Insulator-Semiconductor (MIS) and Semiconductor-Insulator-Semiconductor (SIS), where the insulator could be the vacuum, or in our case, the insulating hemi-cellulose. The MIM (CNT-) junction is clearly a homojunction, and the MIS-junction a heterojunction. For SIS junction, it is more complicated, as the band gap of a CNT is dependent on its chirality, and is difficult to estimate. However, for simplicity, we can treat all these junctions as heterojunctions, where the MIM homojunction is regarded as a heterojunction with zero band gap.

In the DC measurement of macroscopic samples, what we see is the statistical behavior of CNT intrinsic resistances and CNT-CNT junctions. The resistance of thin films can therefore generally be separated into the intrinsic resistance of CNT and the resistance from CNT/CNT junctions as:

$$\rho_T = \rho_{int} + \rho_{junctions} \quad (6.2)$$

where ρ_{int} means the intrinsic resistance along one CNT [0], and $\rho_{junctions}$ defined as the average barrier of an CNT/CNT junctions. The behavior of junctions become more clear when we consider the microscopic CNT/hc thin film, or network fragments (Fig.6.3 (b)) and Fig.6.7 (e)). As the density of CNT/hc decrease, there could be only few CNT/hc pathways across the electrode. At room temperature or higher temperature, the Fermi energy is higher than average CNT-CNT junction barriers, so they are all in the conduction states. For low temperature measurement, the thermal energy of an electron could be much lower than the semiconducting-metal junction barrier, leading to blocked conduction paths.

The intrinsic resistance of one CNT, which depends on its chirality is too complicated to have an exact equation for all situation. In most case, for a CNT network, Kaiser et al. [27, 28] have argued that it is sufficient to simplify the intrinsic resistance, for example, as electron-phonon interaction. The intrinsic resistance could be then written as:

$$\rho_{int} = A \exp\left(-\frac{\hbar\omega_0}{k_B T}\right) \quad (6.3)$$

where, acoustic phonon with frequency of ω_0 is used [0,0,5]. For the CNT/CNT junctions, one of the most widely accepted model for pure CNT-thin film analysis is the so called "Thermal fluctuation assisted tunneling (TFIT)" model [0], which in this case would be a mechanism of thermally assisted hopping (tunneling) over the CNT-CNT junction [27, 28].

$$\rho_{junction} = B \exp\left(\frac{T_b}{T + T_s}\right) \quad (6.4)$$

T_b and T_s are characteristic average barrier height and width. These two terms show opposite behavior when the temperature increases. The TFIT model assumes that the DC electron transport in CNT thin film could be simplified to several conducting paths with different conduction levels. It is interesting to see that the resistance/temperature relationship is opposite for the two terms. The first term which deals with the electron-phonon interaction, the resistance increases with a temperature increase in general. The second term deals with electron hopping/tunneling through the barriers and decreases with temperature increase as electron with higher energy has higher possibility to pass through the barrier. So, for pure CNT thin films with low average energy barriers, the characteristic of resistance and temperature relationship could be a convex curve with inflection point under 300K [0]. However, this is not the case for our CNT/hc thin film. We did not observe clearly convex of resistance/temperature relationship up to 500K, which in principle, guarantee that the energy barrier is the dominant mechanism for CNT/hc transportation. This makes good sense in some way, first comparing with the pure CNT thin film, since CNT/hc thin films might have higher energy barriers as hemicellulose could form

an insulating layer in the CNT junctions. Second, we use relatively high quality CNT materials, where the defects should be lower than in industrial bulk materials.

For a good quality CNT thin film, the TFIT term Eq. 6.4 is the dominant factor for the conductivity. Considering for a thin film with very low conductivity at absolute zero temperature, Eq. 6.4 could be simplified to the Arrhenius equation:

$$\rho = B \exp\left(\frac{-E_a}{k_b T}\right) \quad (6.5)$$

However, it should be noticed that a carbon nanotube thin film that is composed of unsorted chirality CNTs, that it is prohibitively difficult to find an exact solution even for the simplest situation [0]. The difficulties come from different aspects: (a) different chirality CNTs have different density of state, and there different band gaps; (b) it is difficult to estimate the wetting on the CNT-CNT intramolecular junctions; (c) it is difficult to estimate contact resistance between CNT/electrodes; (d) in real case it is rarely the case to find defect free CNT to have a ballistic transport region through the whole CNT, for an exact solution, the electron-phonon and electron-impurity interactions must be taken into account etc.

The KPFM measurements (Fig.6.7), clearly show that the most significant electron potential drops at the CNT/CNT junctions at room temperature with a concrete relationship between the morphology and potential maps. From the topography AFM analysis, the average distance between the crossing of the CNTs is around 0.6 μm . The measurements strongly support the idea that at the microscopic level, electronic potential drops at the CNT/CNT junctions, while the potential drop along the CNTs is less significant. These results support the assumptions of the TFIT model (in Eq.6.4). We also found that there are two types of voltage drops in the CNT/CNT junctions: a pronounced voltage drop and a relatively low level voltage drop. For the first significant voltage drop, which could correspond to the insulating hemicellulose layer between the CNT/CNT junctions. While for the second relatively low level potential drop, it could be caused by the homojunction, without hemicellulose between the two CNTs. From the KPFM measurement data, we can judge that high conductivity in the composite CNT-hc is dominated by the low intertube resistance and low resistance along the CNTs.

The THz measurements of macroscopic thin films yield further information on the intra-tube conduction processes, and intertube conduction. the experimental data of Fig. 6.8 was analyzed by fitting with the following model:

$$\sigma(\omega) = \frac{\sigma_D}{1 - i\omega\tau_D} + \sum_j \frac{A_j(-i\omega + 1/\tau_j)}{(-i\omega + 1/\tau_j)^2 + (v_F q_j)^2} \quad (6.6)$$

where the first term corresponds to long-range, percolative transport, for instance via CNT bundles or adjoining unbundled CNTs. The second term contains a sum over all possible plasmon wavevectors q_j , which in the single plasmon ap-

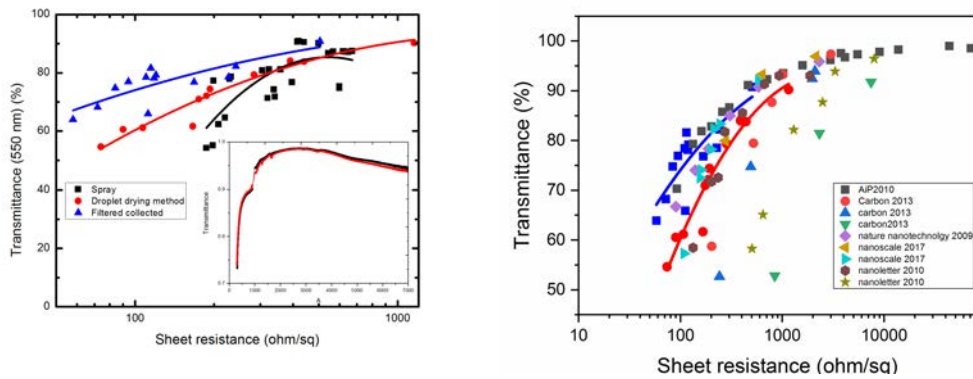


FIGURE 6.10 (a) Sheet resistance versus transmittance at 550 nm wavelength with data fitting by different fabrication methods, Inset: transmittance of DWCNT-CNT/hc thin film sample in IR range (b) comparison of our results with other undoped single-walled carbon nanotube TCFs published in recently years.

proximation, namely that $q_j = \pi/L_j$, amounts to a sum over all possible lengths L_j . The amplitude term A_j represents the relative number of CNTs with that particular active length, and an average over all possible orientations. The excellent fit of the model to the data supports the picture of relatively smooth intra-tube conduction and low resistive but overall dominating intertube junction resistances.

From low temperature DC measurement, KPFM, and THz conductivity measurement, we have used different methods to systematically analyze the conductivity properties of CNT/hc thin films. Comparing with the resistance coming from the defects or phonons interacting with the electrons along the DWNT, the CNT/CNT junctions seem to be the dominant mechanism for the CNT/hc transport properties. This mechanism is supported by the all the experiment results as we have discussed above.

Compared with other pure CNT thin film, we observed very high transmittance accompanied with good conductivity at visible light range (Fig.6.10(a)) with normal incident light structure. Comparing with the recently published best pure CNT TCFs (Fig.6.10(b)), the vacuum filtering method and droplet dry method have shown similar or even better performance.

Conclusions

The water dispersed CNT/hc complex is a high conducting new material that has similar conductivity properties as pure CNT materials. It is relatively easy to fabricate for measurement homogeneous thin films with droplet drying, spinning, spraying and vacuum filtering methods. From KPFM, THz and model fitting for low temperature measurement, it is confirmed that for CNT/hc thin film, the resistance is mainly from the CNT-CNT junctions, while the resistance drop along one CNT could be neglected for most cases. For transparency conductivity thin film analysis,

it clearly shows that the transmittance of CNT/hc thin films have strong dependency on the electromagnetic wavelength. For full range EM analysis, the transmittance of CNT/hc thin films increases with wavelength decrease due to the complex conductivity increase. In the visible light and UV range, some EM are adsorbed by the CNT inside of the thin film.

We also made one possible application of CNT/hc thin film as transparent conducting thin film. Compared with the most pure CNT thin films, the CNT/hc still shows very good figure of merit. Considering the fabrication simplicity and the environmental friendliness, this new CNT/hc materials could be a candidate material.

Chapter 7

Physical and chemical adsorption of proteins to surface

As was briefly introduced in the Chapter 3, avidin adsorption on a solid surface plays a key role in many biotechnology applications etc. In general, it is almost exclusively resorted to chemical adsorption with covalent cross linker due to the robust chemical bonding cross linker. In contrast, the study of avidin like protein with physical adsorption on solid surface, even though very important, is poorly understood. Some key problems of this research area are the possible denaturalization on different surfaces, and the functionality after deposition.

In this chapter, I will present a series of experiments about chi-avidin (one in avidin family) on different kinds of surfaces with physical adsorption. In the first section, I will give some basic introduction of materials and surface treatment. The solid surface used in this experiment included HOPG, graphene, Si/SiO₂, carbon nanotube etc. In the second part, I will show some experimental results of chi-avidin physical adsorption on hydrophilic or hydrophobic surfaces. The interesting finding of chi-avidin physical adsorption is double layer aggregation on carbon materials surface, that turns out also to be very important for their functionality. The functionality of chi-avidin after adsorption are tested with 5 nm biotin-gold nanoparticles that will be explained in the third section, and also in Chapter 8.

7.1 Materials and substrate preparations

Chimeric Avidin (Chi-Avd) was first assembled in 2004 by Vesa Hytönen et al [21] using E.coli. Two batches of chi-avidin have been used in the following experiments, which were received from the group of V. Hytönen at University of Tampere. The first was 100 uM chi-avidin in 50 nM NaPO₄ buffer [080212NK-ChiAVD 117y 181110], and the other 100 uM in water [ChiAVD 117y 181110 Juha]. The results showed very similar results for these two batches.



FIGURE 7.1 (a) 5 nm biotin gold nanoparticles from Cytodiagnosics; (b) SEM image of b-AuNPs on silicon oxide with RIE treatment. Scale bar of 200 nm

5 nm biotin gold nanoparticles (b-AuNPs) were purchased from Cytodiagnosics. The original concentration of b-AuNPs is 4.5 μM , with size dispersity less than 15 percent. For each particle, the average surface area is 78 nm^2 , with $0.5/\text{nm}^2$ biotin density on surface, on average there are around 40 biotin molecules on each AuNP. 5 kDa polyethylene glycol (PEG) chains were used as spacer arm, this give an average Flory radius of 4.2 nm (Contour length of 31 nm).

Highly oriented pyrolytic graphite (HOPG) used in this experiment is a commercial product from Goodfellow. The fresh HOPG surface is made by scotch taping method. What left could be considered as a stack of highly ordered graphene layers.

The single layer graphene used in this experiments were commercial products of Graphenea Inc, on 300 nm thickness silicon nitride surfaces. Thermal annealing in Carbolite CTF/12/64/550 tube furnace in nitrogen condition at $400 \text{ }^\circ\text{C}$ for 5 hours was used to remove the polymers on top.

Precut $8 \text{ mm} \times 8 \text{ mm}$ pieces of silicon wafer were cleaned by removing small particles by blowing with a carbon dioxide gas gun, and then washing with acetone and IPA. The Si pieces were rendered hydrophilic or hydrophobic with reactive ion etching (RIE-Plus Oxford Instruments). The hydrophilic treatment was 2 mins (50 sccm O_2 , 300W, 13.56 MHz, $30 \text{ }^\circ\text{C}$), and the hydrophobic treatment 2 mins (50 sccm CHF_3 , 5 sccm O_2 , 300W, 13.56 MHz $30 \text{ }^\circ\text{C}$), The contact angle of HOPG and hydrophobic treatment silicon is similar of 84 and 86 degree respectively.

Physical adsorption of avidin were done by incubation (figure. 7.2). After appropriate conditioning of the substrate, a small droplet (usually 50 μL) of avidin solution was placed on it. The washing steps included three 1 min dd- H_2O immersions and 3 times of 1000 μL pipette blowing. The sample was then dried with a nitrogen air gun.

For preparation of the samples, phosphate-buffered saline (PBS) buffer were used for all experiments involving ChiAvd and biotinylated gold nanoparticles. The recipe of PBS buffer we used is 0.8g/L NaCl, 0.2g/L KCl, 1.4g/L $\text{Na}_2\text{HPO}_4 \times 2\text{H}_2\text{O}$, 0.2g/L KH_2PO_4 . Deionized water was used made from Milli-Q ultrapure water system.

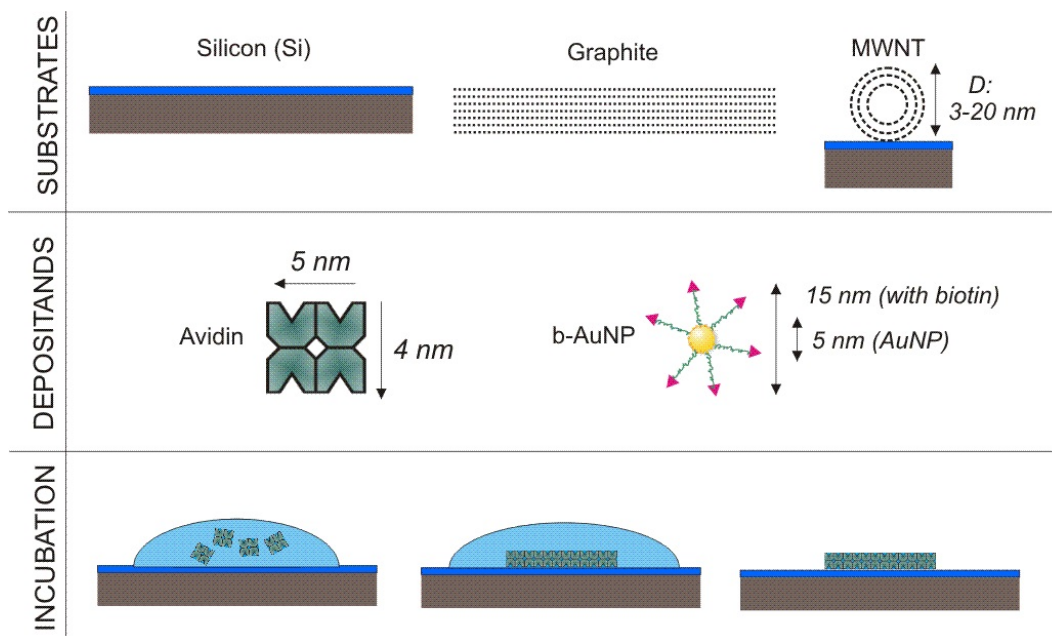


FIGURE 7.2 The essential elements of the experiments: First row: The substrates used for physical protein adsorption. Second row: the protein we study is Avidin. Biotinylated gold nanoparticles (b-AuNP) are used to test the functionality of avidin with respect to its ability to bind biotin. Third row: A scheme for the simplest incubation technique of avidin on a surface, which is some of three mentioned above. A droplet of a solution of avidin is placed on a substrate, and allowed to stand there for a predetermined time. Physisorption of avidins takes place during this time, after which the droplet is blown away.

7.2 Physical adsorption of chi-avidin on different surfaces

7.2.1 Physical adsorption of chi-avidins on hydrophilic and hydrophobic silicon surface

Physical adsorption of chi-avidin prefer to form randomly separately isolated clusters or self assembled monolayer on silicon surface. The density of chi-avidin on the silicon surface depended on the concentration of the original chi-avidin solution and incubation time (Fig.7.3(a)). The hydrophilic or hydrophobic treatment does not have significant influence on the concentration of chi-avidin density (Fig.7.3(b)).

The highest density we found of chi-avidin on silicon surface is around 6500 units per square at $\text{pH}=7$ buffer with physical adsorption (Fig.7.4(a)). This is about 20 % of the highest reported chemical adsorption density on biotin functionalized surface (2800 Ru) [0]. One possible explanation for this phenomenon is that Chi-avidin in $\text{pH}=7$ PBS buffers bears a net positive surface charge ($\text{pI}=9.5$ $\text{pH}=7$ buffer), causing net repulsion.

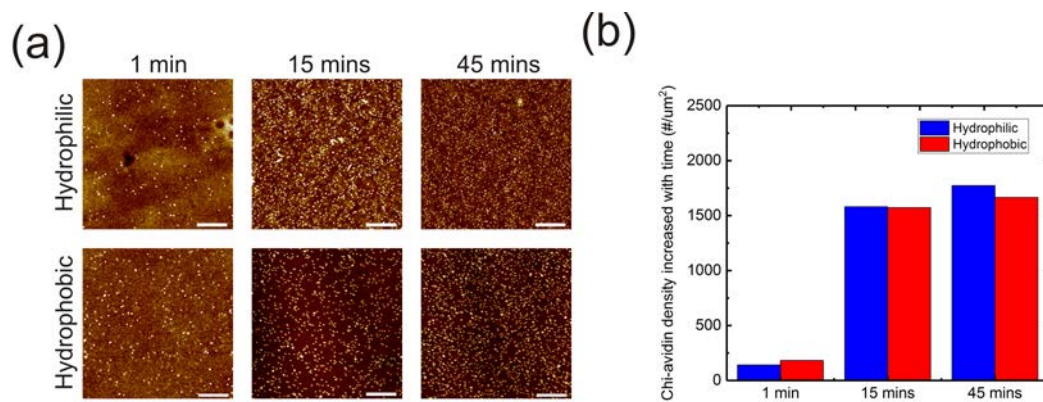


FIGURE 7.3 (a) 0.1 μM Chi-avidin incubation on hydrophilic/hydrophobic treatment silicon surface with different incubation time. The incubation period is labeled on the figure above, with incubation time from 1 min, 15 mins to 45 mins, the scale bar are 200nm. (b) The density of Chi-avidin (Numbers per micrometer square) is displayed as a function of incubation time. On hydrophobic or hydrophilic silicon surface, there is very little difference with the same incubation time.

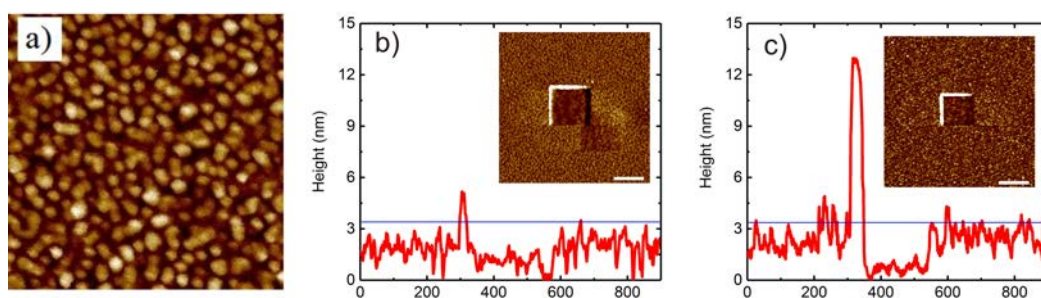


FIGURE 7.4 (a) Dense avidin deposition on silicon, scanning size of 200 nm, the density of chi-avidin is around 6500 units per micrometer square; (b-c) Cross section of self assembled chi-avidin on hydrophilic and hydrophobic treatment silicon with height data.

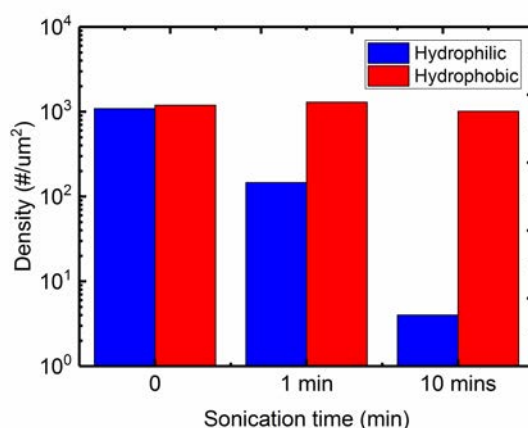


FIGURE 7.5 To evaluate the attachment strength, the density of avidin is shown as a function of bath sonication, on hydrophilic and hydrophobic surface that initially had a high density concentration.

The measuring height of individual globular clusters (which is very likely to be separated individual chi-avidins) is around 2.5 to 3 nm (Fig.7.4(b-c)). This number is clearly lower than that measured with crystallographic data (5nm x 5nm x 4nm). However, it should be noticed that for XRD crystallography supports highly extended shape of the protein in its natural state. While, on silicon surface, they are partially collapsed.

Even though the hydrophilicity of silicon surface treatment has little effect for the density of chi-avidin physical adsorption on silicon surface, we found that affinity of chi-avidin strongly depends on the surface treatment method, which have been widely known for other proteins. This was tested with simple bath sonication (Fig.7.3). The graphic of Fig.7.3 shows that the density of chi-avidin on hydrophobic surface keeps constant for 10 mins bath sonication, while on hydrophilic surface, the density drops very quickly. This phenomenon could also be supported by cross section (Fig.7.4(b-c))experiment with so called “peakforce mode”. Peakforce mode has been briefly explained in Chapter 4, that determines the maximum force between the AFM tip and sample in contact. We found that the chi-avidin incubation on hydrophobic treatment silicon could be only be totally removed by 30 nN peakforce, while on hydrophilic surface a 14 nN force was sufficient.

7.2.2 Chi-avidin physical adsorption on HOPG and graphene surface

The very different chi-avidin patterns on HOPG or graphene surface is shown in Fig.7.6 comparing with physical adsorption on silicon surface. One obvious different from topographic point of view is that chi-avidin has a strong tendency to ag-

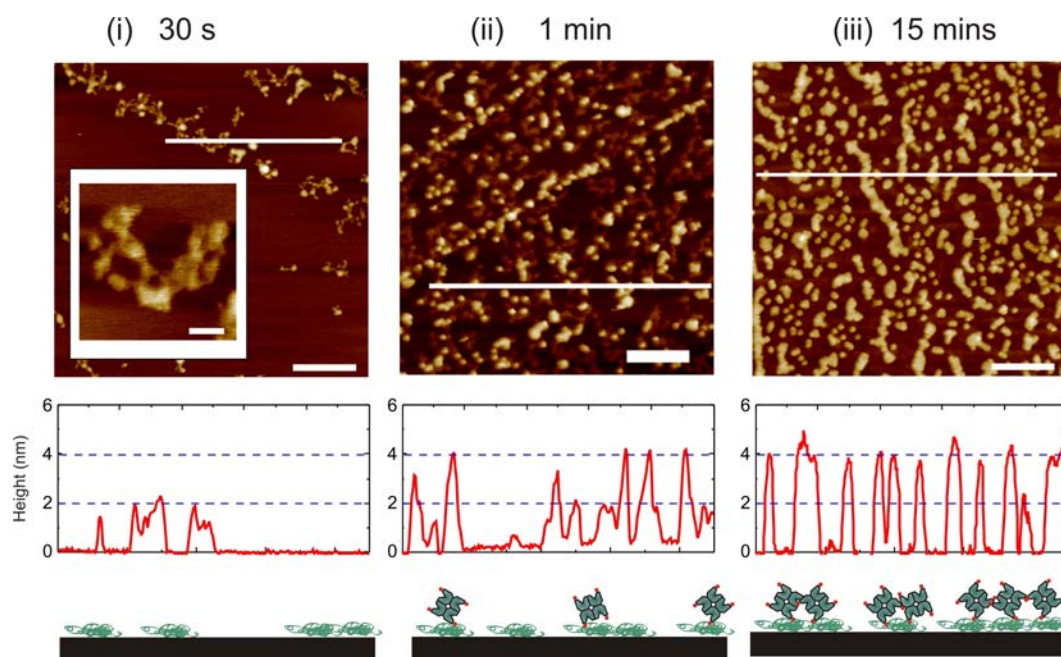


FIGURE 7.6 Avidin deposition on HOPG. The uppermost AFM images show the deposited avidin, after incubation from 1 μ M solution for three different times. These times are indicated above the figures. Scale bars are 100nm (i) has closer image as inset, with scale bar of 20nm. Below the AFM images is topographical height data extracted from them along the lines. Lowest is a schematic illustration of the suggested model for pattern formation by the avidins

glomerate, or to form clusters, on HOPG or graphene surface. Fig.7.6 shows avidin after incubation from 1 μM solution on HOPG, in samples with different incubation times, and with AFM profile height data. These three images were taken from the same sample, with time sequence. After the shortest 30s incubation, shown in the first image (i), the avidins have formed separated irregular or slightly chain-like clusters. Some of these clusters appear to form linear assemblies, which most likely correspond to the omnipresent single layer fault lines of a HOPG surface. The same phenomenon has been observed with other proteins [26]. A closer image of a typical avidin cluster is shown in the inset of figure.7.6(i). The height of these irregular clusters is around 1.5 to 2 nm, which is lower than the individual avidin height on Si.

Figure.7.6(ii) shows the avidin patterns after a longer, 1 min incubation. There is a crucial difference to the previous figure: the pattern is essentially similar, but from the AFM height data, we can see that besides the 2nm height, a second height level of around 4 nm appears. Our interpretation is that a second layer of avidin starts to form on top of the first deposited (mono-)layer, already slightly chain-like in appearance. In this case, the second, which we call a double layer, has not fully covered the first monolayer. In the third, 15 min incubation, all avidin structures are now around 4-5nm in height, corresponding to the double layer type. In Figure 7.6-lowest we give one possible explanation about the chi-avidin physical adsorption.

The irregular patterns forms on top of HOPG with chi-avidin could be simplified into two different categories: which we called them as "chain structure" (Fig.7.7(a-b)) and "widening irregular patterns" (Fig.7.7(c-d)). Interestingly, both "chain structure" and "widening irregular patterns" could be either in form of monolayer, or double layer. For monolayer situation, the height of irregular patterns is around 1.5 to 2.5 nm, and after second layer deposition, the height increased to 5 to 6 nm. We have not the ability to fully control the formation of these two different irregular patterns. The size of the empty regions is in the 10-100 nm range. This is, however, clearly excluding any possible explanation with water droplet patterns (which is in micrometer scale).

7.2.3 Chi-avidin physical adsorption on suspended carbon nanotube.

Next, we move to arc-discharge MWNTs, which give us the opportunity to study deposition on curved graphite. While the material contains amorphous carbon debris, the tubes themselves are of high quality, and by searching one can find in selected locations MWNTs with few impurities within a micron scale area. Figure.7.8(a) show an MWNT of diameter 10 nm before deposition. The AFM images reveal a smooth tube surface mostly absent of impurity particles or other deficiencies.

Figure.7.9 shows two suspended MWNTs of diameter 16 nm and < 20 nm,

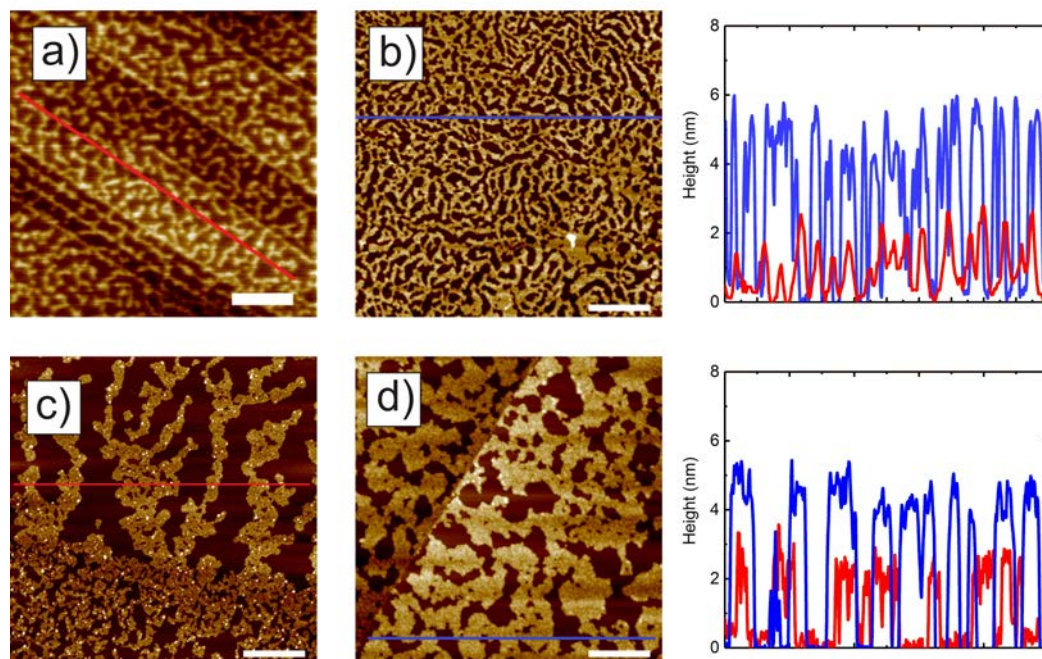


FIGURE 7.7 Two different irregular patterns often observed on HOPG. Above: single layer chain structure (a) and double layer chain structure (b) with their height data. Below: widening irregular patterns with single layer (c) and double layer (d). The scanning bar is 200 nm.

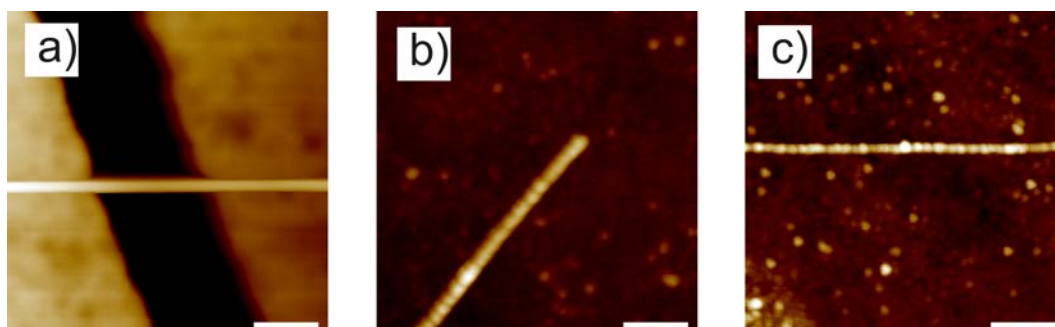


FIGURE 7.8 AFM images of avidin deposition on MWNTs. a) Suspended MWNT before deposition. $D = 10$ nm. b) Avidin on MWNT with $D = 5$ nm. c) Avidin on MWNT with $D = 3$ nm

after avidin deposition. Besides occasional differences, we did not observe any clear-cut evidence for different deposition of avidin on a suspended section compared to the non-suspended parts. We conclude that possible effects of the suspension are masked by complicated local effects beyond our control. A most interesting result is the character of the avidin depositions, observed in these larger diameter MWNTs. The deposits have the form of stripes that are roughly perpendicular to the tube axis.

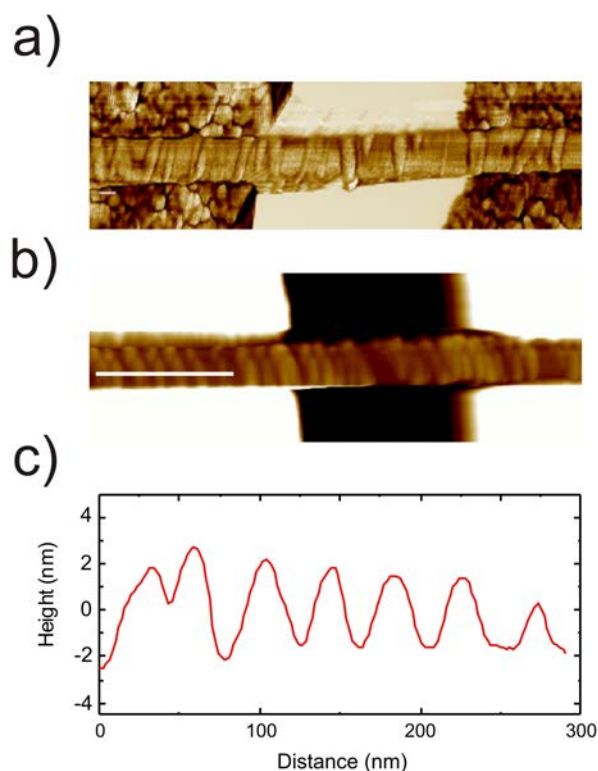


FIGURE 7.9 AFM images of avidin deposition on suspended MWNTs (stripes perpendicular to tube axis). a) MWNT $D = 16$ nm b) MWNT $D = 17$ nm c) height profile along the line in b)

Figure.7.8(b,c) show in tubes of smaller diameter, that the deposits are still present but their stripe-like character, as observed with the AFM, gradually vanishes. Besides the self-evident fact, that there is not space for multiple proteins to link up into chains across the smallest tubes, it is to a large extent understandable as a technical imaging issue. The tip radius is typically around 10 nm and the tip apex is of course not truly spherical, and is therefore unable to discern the real geometry of the avidin deposition around the curvature of smaller diameter tubes. The height is measured as 2-5 nm, and we did not find a visible transition from single layer to double layer structures. Despite this inaccuracy, it is clear that the height corresponds to that on graphite. The separation between the stripes varies but is in the range 20 - 40 nm. Figure.7.9(b) demonstrates that the deposits can sometimes be

very regularly spaced.

7.3 The functionality of chi-avidin after physical adsorption on the surfaces

We tested the functionality of the avidin deposits, or the ability of the surface bound avidins to bind biotinylated gold nanoparticles (b-AuNP) via the biotin coupling. Some possible denaturalization process could eliminate the functionality after deposition. The functionality testing of chi-avidin is done with commercial 5nm biotinylated gold nanoparticles (b-AuNPs) via a standard biotin coupling. In this Chapter, I report on test with graphite surfaces. Further experiments are presented in the next chapter.

7.3.1 The functionality of chi-avidin on HOPG or graphene

The functionality of chi-avidin on HOPG or graphene is more complicated and less ambiguous than that of incubation on silicon surface. As it is discussed in the Section. 7.2.2, the chi-avidin on HOPG could form either self assembly monolayer or double layer with ("chain structure" or "widening irregular patterns"). We will demonstrate the functionality results separately. Negative control experiment, and one chemical functionalization method of chi-avidin deposition method will also be shown in this section.

The first and the second columns of figure.7.10 shows results of deposition of b-AuNP on the mono- and double layers, respectively. In a single column, above is an AFM-image with a height data profile, and below these a SEM-image. It is strikingly clear that on the presumed unfolded/denatured single layer chain structure (first column), there is little affinity to b-AuNPs, as especially the SEM images reveal (figure.7.10(i))the absence of any gold particles. As opposed to this, the double layer structure (second column) attracts efficiently b-AuNPs. The third column contains images of a double layer made from biotin-blocked avidin (figure.7.10-iii). The affinity for b-AuNP is negligible, which then confirms the avidin-biotin linking as the mechanism behind the affinity to the double layer.

7.3.2 Chi-avidin on HOPG with cross-linker

Besides that, we also did one experiment on chemical deposition chi-avidin on HOPG surface (Fig.7.11). The chemical cross linker used in this experiment is 1-pyrenebutanoic acid succinimidyl ester, which has been widely used in carbon nanotube functionalization, to form covalent bonding with the amino group on the proteins. The other side of the 1-pyrenebutanoic acid succinimidyl ester cross linker, is the weak pi-pi interaction on the graphene hexagons carbon structure.

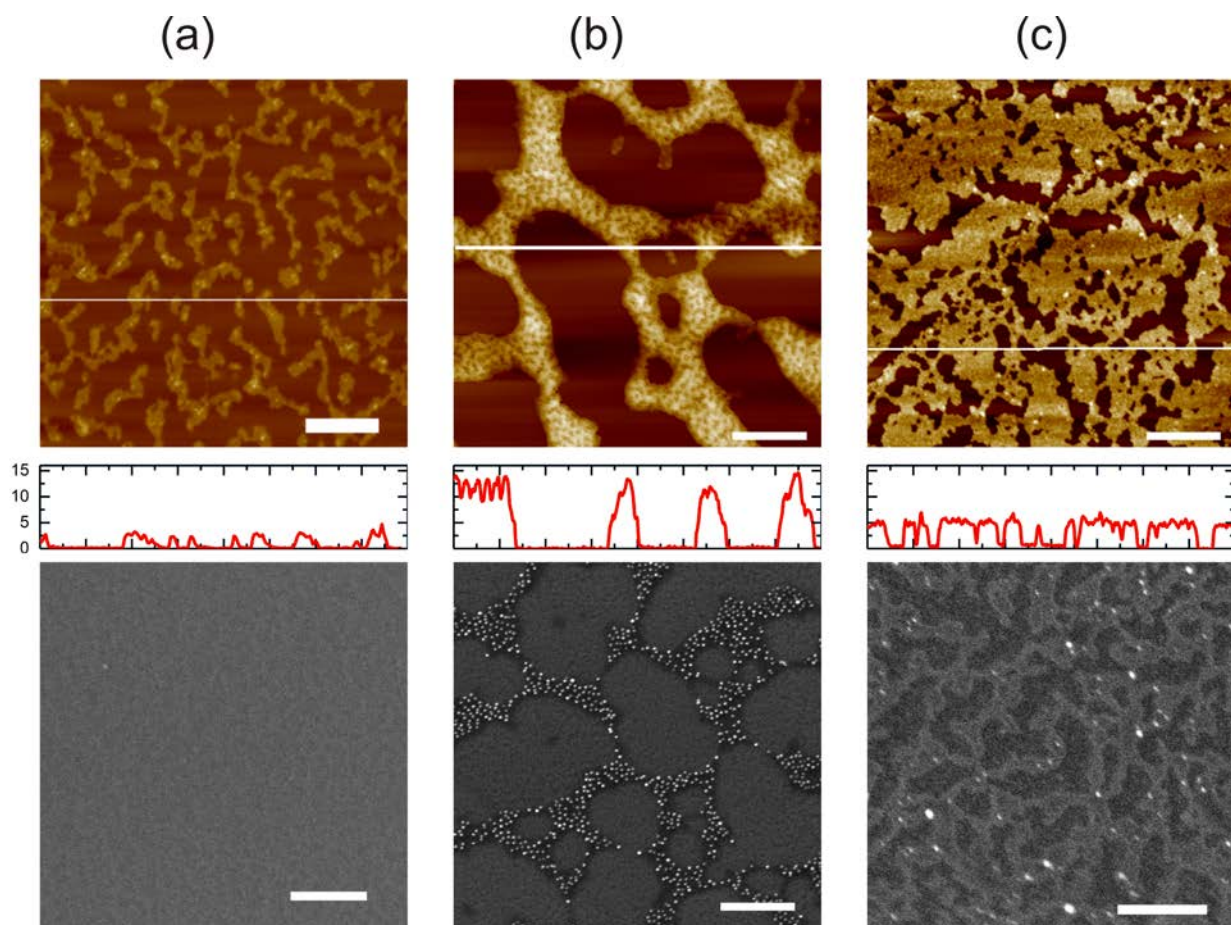


FIGURE 7.10 Testing functionality of three different Avidin layers on HOPG by incubation with b-AuNP and subsequent imaging. For each case, on top is an AFM-image and below it a height profile. Lowest is a SEM-image. (a) avidin monolayer; (b) avidin double layer; (c) d-biotin blocked double layer. Scale bar 200 nm.

The AFM image of chi-avidin on HOPG with chemical cross linker (Fig.7.11), clearly show that the deposition of chi-avidin on HOPG is very different with chemical cross linker or with physical adsorption. We did not observe any significant chain structure, or widening irregular patterns that usually shown in the physical adsorption. What is shown in the AFM image of chemical functionalization chi-avidin deposition is a smooth layer which is very similar with physical adsorption on silicon or so. The density of chi-avidin is difficult to count exactly with AFM. One possible estimate is 32,500 per micrometer square. From SEM image, we can estimate the binding b-AuNPs of chi-avidin is around 1200 per micrometer squared reference.

7.4 Discussion and conclusions

In this chapter, we have demonstrated that physical adsorption of chi-avidin occurs in very specific and different ways depending on the characteristic surface. On

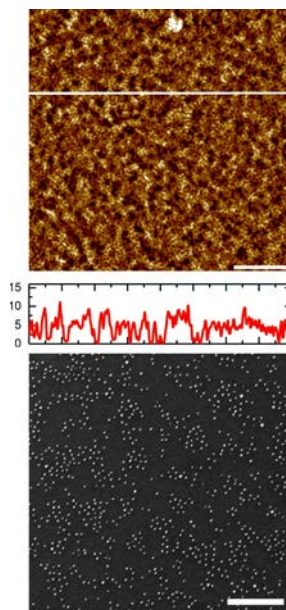


FIGURE 7.11 Chemical functionalization of chi-avidin with its functionality, above AFM and below SEM images. The scanning bar of 200 nm.

silicon or silicon oxide surface, physically deposited chi-avidin more easily forms isolated globular clusters. From the height data and topography data (Fig.7.3 (a)), we conclude that they are chi-avidin tetramers. The measured height ~ 2.5 nm, is clearly lower than their solution phase crystallographic data. However, this is a very common phenomenon for large protein (MW > 50kDa) on surface. We did not observe an obvious different height of chi-avidin on hydrophilic/hydrophobic-treated silicon (Fig.7.4). However, we found that hydrophilicity seems to strongly affect the affinity of chi-avidin on the silicon surface (Fig.7.3 (b)), a result which is in agreement with previous publications [REF...]. In this work, the avidin monolayer has at saturation coverage a density of around 6,000 per micrometers (500 Ru). This is about 20 % of the highest reported chemical adsorption density of avidin on biotin functionalized surfaces (2800 Ru) [0]. A possible explanation could be that avidin in PBS bears a net positive surface charge ($pI=9.5 > pH=7$ buffer), causing interprotein repulsion.

On graphite, the results are very different. Instead of globular clusters, chi-avidin show strong tendency to form irregular patterns either as chain structure or in widening irregular patterns (Fig.7.6). Further investigation points to a two stepped formation process, where the deposition of the first layer is strongly accompanied by denaturation and protein unfolding and this layer having a small height. Seemingly this first layer is strongly adhering to the next avidin still in the solution phase, leading to the formation of the bilayer structure (figure.7.6(a)). The exact formation mechanism is still unknown, but some similar behavior have been published in proteins such as ezrin [17] and fibrinogen [15].

On chi-avidin deposition on MWNTs, we observe clearly strip-like deposition patterns, which are perpendicular to its axis. In previously published works, mostly chemical adsorption methods have been used. However, there are at least two reports of TEM high resolution imaging of proteins on MWNT surface, despite that TEM imaging of proteins is seriously hampered by the low visibility as they consist of light atoms. Balavoine et al. [4] reported of streptavidin on MWNTs while Ling et al. [29] reported of a recognition protein (C1q) on the MWNT. Both works are on arc-discharge MWNTs as in our case.

Finally, our results demonstrate a very specific behavior of avidin as on graphite the double layer exhibits capture of b-AuNP while the monolayer doesn't. The result was well confirmed by the blocking of the biotin sites in the double layer so that no b-AuNP was adsorbed. One possible explanation suggest that the first avidin layer is unfolded, and represents protein which has lost the biological functionality.

Conclusions

In this research we used chi-avidin, a class of avidin family which have been widely used in biotechnology, to do experimental study of physical adsorption on two different surfaces, like HOPG, graphene, and Si/SiO_x. We observed very different physical adsorption mechanism on different surface, which is first time in this class of protein. Moreover, we used biotinylated gold nanoparticles to test the functionality of these proteins, which indicates that the different adsorption mechanism has strong influence on the functionality of the protein. What's more interesting, we found that physical adsorption of chi-avidin could have similar or even better affinity to b-AuNPs, that could pave a new road to new biosensors and immune analysis devices.

Chapter 8

Towards a nanoparticle actuator

From the very beginning of the nanotechnology era, researchers have the dream to manipulate a single atom or a single molecule [Feynman]. This was the stated goal of a Research project within the Programmable Materials program, OMA (Ohjelmoitavat Materiaalit) of the Academy of Finland, of which my Thesis was part of. The research work described in the previous chapters was motivated by a goal of fabricating single protein devices controlled by a local electric field, which could be executed, for example, from a CNT. In this chapter, I will describe some further experiments with avidin and its functionality on a surface. Moreover, I present very briefly experiments with DNA, with which some electric field control, or a nanoactuator, eventually was demonstrated.

For the demonstration of the nanoactuator, the biomolecule to be actuated with the electric field is covalently linked to a gold nanoparticle, and the movement of the biomolecule and nanoparticle is detected via a distinct optical feature, the localized surface plasmon resonance (LSPR). The LSPR is the collective oscillation of electrons in the gold nanoparticle in resonance with a specific wavelength of incident light. Even atomic scale motion of the nanoparticle can be detected as the peak shift in visible light range due to the change of the dielectric constant around it.

One candidate for the biomolecule and nanoparticle pair was the avidin linked to b-AuNP. This was discussed already in Chapter 7. Below I present some additional experiments focused on the problem of demonstrating the linking of avidin and b-AuNP in different settings. Due to practical difficulties these did not lead to a nanoactuator demonstration, and DNA was used instead. In Section 8.2, I will briefly talk about the DNA actuator assembly procedure [Publ. III].

8.1 Concept proof of high selectivity of b-AuNPs and avidin interaction on surface

The avidin-biotin interaction has been widely used in biotechnology with its extraordinarily high affinity. However, most of these applications were done in buffer condition or on surface with chemical cross linkers. Very limited information with concrete evidence is known about avidin-biotin interaction when avidin is first deposited on the surface with physical adsorption (as with graphite surface in section 7.3). In this chapter, I will demonstrate avidin b-AuNP linking in different settings. In chapter 8.1.1 I will give a strict experimental proof of the avidin b-AuNPs in buffer condition with different optical measurement like dynamic light scattering (DLS) and visible light adsorption. Next, I will give some statistic analysis of avidin b-AuNPs complex in buffer condition by spinning it on the silicon surface (Chapter 8.1.2). In the end (Chapter 8.1.3), I will proof that with physical adsorption on silicon oxide surface, chi-avidin still have reasonable functionality, which setup on a strong foundation for nano-particle actuator research (Chapter 8.2).

8.1.1 Chi-avidin and b-AuNPs functionality in buffer

We repeated the standard concept proof of avidin-biotin linkage in buffer. There is plenty of information about the avidin-b-AuNPs interaction in buffer condition, which could be used to check that the interaction works in our case.

Dynamic light scattering concept proof

The first method used was Dynamic light scattering. We measured the hydrodynamic radius of pure chi-avidin, pure 5nm b-AuNPs and their mixture in HEPE buffer (with number ratio of 4:1) at room temperature with Malvern system. A hydrodynamic radius is calculated from diffusion coefficient following the equation.8.1.1

$$R_H = a = \frac{k_B T}{6\pi\eta D} \quad (8.1)$$

For simplicity, we treat these molecules or clusters as spherical rigid balls. The hydrodynamic radius of these molecules, therefore, could account for their real radius as approximation.

From Fig.8.1(a) and (b), it clearly shows that the hydrodynamic radius of chimeric avidins and 5nm b-AuNPs are around 5nm and 15 nm in HEPE buffer with a single peak respectively. For the complex of chi-avidin and b-AuNPs (Fig.8.1 (C)), two peaks instead of single peak with radius of 11nm and 800 nm could be easily distinguished.

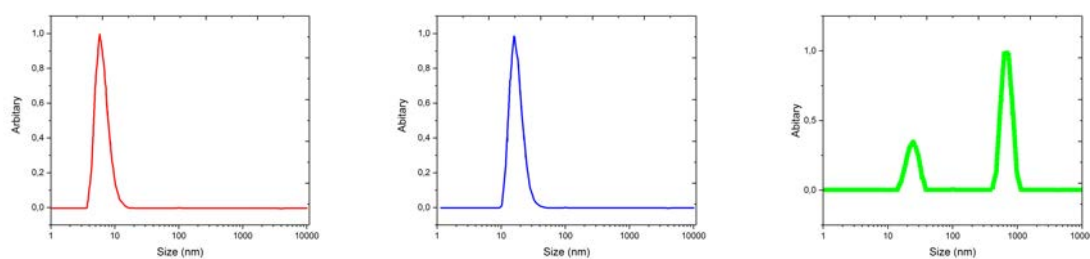


FIGURE 8.1 DLS experiment of (a)chimeric avidin and (b) 5nm -b-AuNPs in HEPE buffer. (c) mixture of chi-avidin and b-AuNPs in HEPE buffer with number raito ~ 4 to 1. (128 nM to 40 nM)

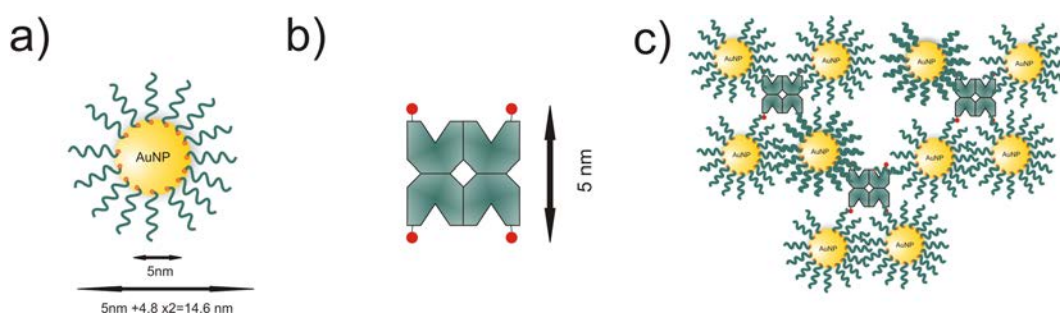


FIGURE 8.2 The size of particles in buffer condition: (a) 5 nm b-AuNPs with 5 nm gold shell as a core, and 5000 Da PEG linker of total radius of 15nm; (b) tetramer of chimeric avidin in buffer of size of $5nm \times 5nm \times 4nm$; (c) For each chimeric avidin, there are four biotin anchoring point with maximum four gold particle binding. However, for each gold particles, there could be more than one chi-avidin binding.

The explanation of these DLS peaks are straightforward. For 5 nm b-AuNPs (Fig.8.2(a)), the gold core sphere size is 5nm, with 5 kDa PEG linker of Flory radius (end to end distance) of $4.8nm$ ¹. Therefore the hydrodynamic radius of b-AuNPs should be around $5nm + 4.8nm \times 2 = 15nm$ which is the same as what we measured in the DLS.

Chimeric avidin is more complicated, from the crystallographic structure, the size of a chimeric avidin tetramer is $5nm \times 5nm \times 4nm$, and a monomer is $2.5nm \times 2.5nm \times 4.5nm$. So based on the experimental observation, chimeric avidin are likely to be tetramers in the buffer (Fig.8.2(b)).

The first peak in Fig.8.1 (c) could be the excessive b-AuNPs that does not bind to chimeric avidin. The second peak with larger diameter could indicate the average size of chimeric avidin and b-AuNPs in HEPE buffer. For each chimeric avidin, there are four biotin anchoring points with maximum four b-AuNPs binding. However, for each b-AuNPs, there could be more than one chi-avidin binding. For DLS experiment, the hydrodynamic radius could only give an average size of these complexes.

¹https://figshare.com/articles/PEGlinkers_and_properties/1234939

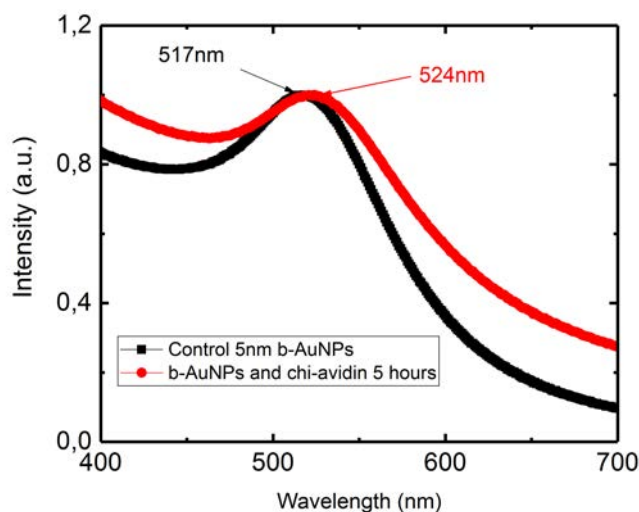


FIGURE 8.3 Vis spectrum of 5nm B-AuNPs, before (black) and after (red) conjugation to chimeric avidin. The red shift of the LSPR peak is around 7 nm.

Visible light adsorption proof

When chi-avidin used in this experiment binds with a gold particle, we can detect the LSPR peak shift in visible light range. 5 nm b-AuNPs that is diluted in the water, with a LSPR peak of 517 nm has been first measured. This peak is in agreement with the Cytodiagnostic spherical standard gold nanoparticles' peak SPR (515 to 520nm). After 5 hours chi-avidin incubation, the adsorption LSPR red shifts to 524 nm from the spectrum. The adsorption peak also broaden, with a slight peak intensity decrease. The mechanism behind the red shift of the spectrum could be explained by the increase of the local refractive index at the gold nanoparticle shift.

8.1.2 Chi-avidin/b-AuNPs deposition from buffer

Several droplets of the chimeric avidin and b-AuNPs mixing solution (used in DLS experiment) was spilled on the hydrophilically treated silicon oxide with AFM markers. This allowed to perform AFM and SEM imaging at exactly the same location and thus the same deposited avidin-b-AuNP complex.

Let's consider the most complex situation in buffer conditions. In buffer, there could be three different components: (a) isolated chi-avidin without b-AuNPs binding; (b) isolated b-AuNPs without chi-avidin binding; (c) complex of chi-avidin and b-AuNPs. For the complex of chi-avidin and b-AuNPs (condition (c)), it is very easy to distinguish by AFM and SEM due to different lateral dimensions. Isolated chi-avidin and isolated b-AuNPs could not easily be distinguish by AFM, as they are all isolated clusters with similar height around 3-5 nm. To distinguish isolated b-

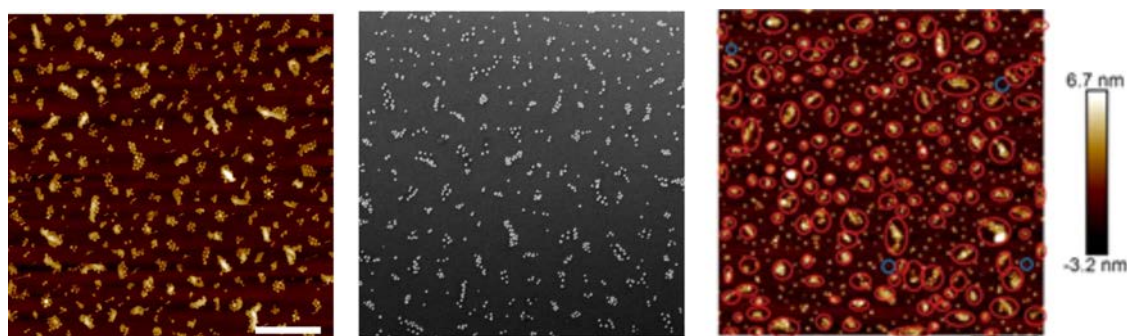


FIGURE 8.4 (a)AFM and (b)SEM image of the chimeric avidin and b-AuNPs conjugated solution on silicon, with the same scanning areas. The scanning bar is 100 μm (C), Color indication of b-AuNPs clusters (in red circles), and isolated gold b-AuNPs (blue circle), the rest particles on AFM without any circles are the isolated chimeric avidins. Scanning bar of 200nm.

AuNPs and chi-avidin, SEM could be very useful. As it is shown in Fig.8.1.2(b), gold particles with much heavier atom component, looks shiny in SEM. For proteins that are composed of majority of light element, look blurry or dark in SEM images.

TABLE 8.1 Statistic of b-AuNP and chi-avidin deposition from HEPE buffer. Estimation from AFM and SEM from Figure 8.1.2.

Name	number (per square micrometer)
isolated chi-avidin	4
isolated b-AuNPs	387
Chi-avidin and b-AuNPs complex	145

From Table.8.1 and Fig.8.1.2, it is clearly shown that b-AuNPs have strong affinity to chi-avidin in buffer condition. There are lot of isolated b-AuNPs which does not bind to chi-avidin, which give the smaller hydrodynamic radius peak in DLS experiment (Fig.8.1 (c)). For each chi-avidin and b-AuNPs complex, it is composed of several b-AuNPs and chi-avidin. In reality, most of the b-AuNPs form a complex with chi-avidin. With all these experiment, we have full confidence that b-AuNPs have strong affinity in buffer condition as it should be.

In principle, it is possible to have one to one avidin-biotin interaction, with a monovalent version of avidin [19], which could be very interesting for certain biotechnology applications.

8.1.3 The functionality of chi-avidin on silicon surface

The SEM images (Fig.8.5) clearly show that on hydrophobic/hydrophilic silicon surface, the chi-avidin deposit have some good affinity to catch the b-AuNPs. The density of b-AuNPs on hydrophobic/hydrophilic silicon surface that is covered with

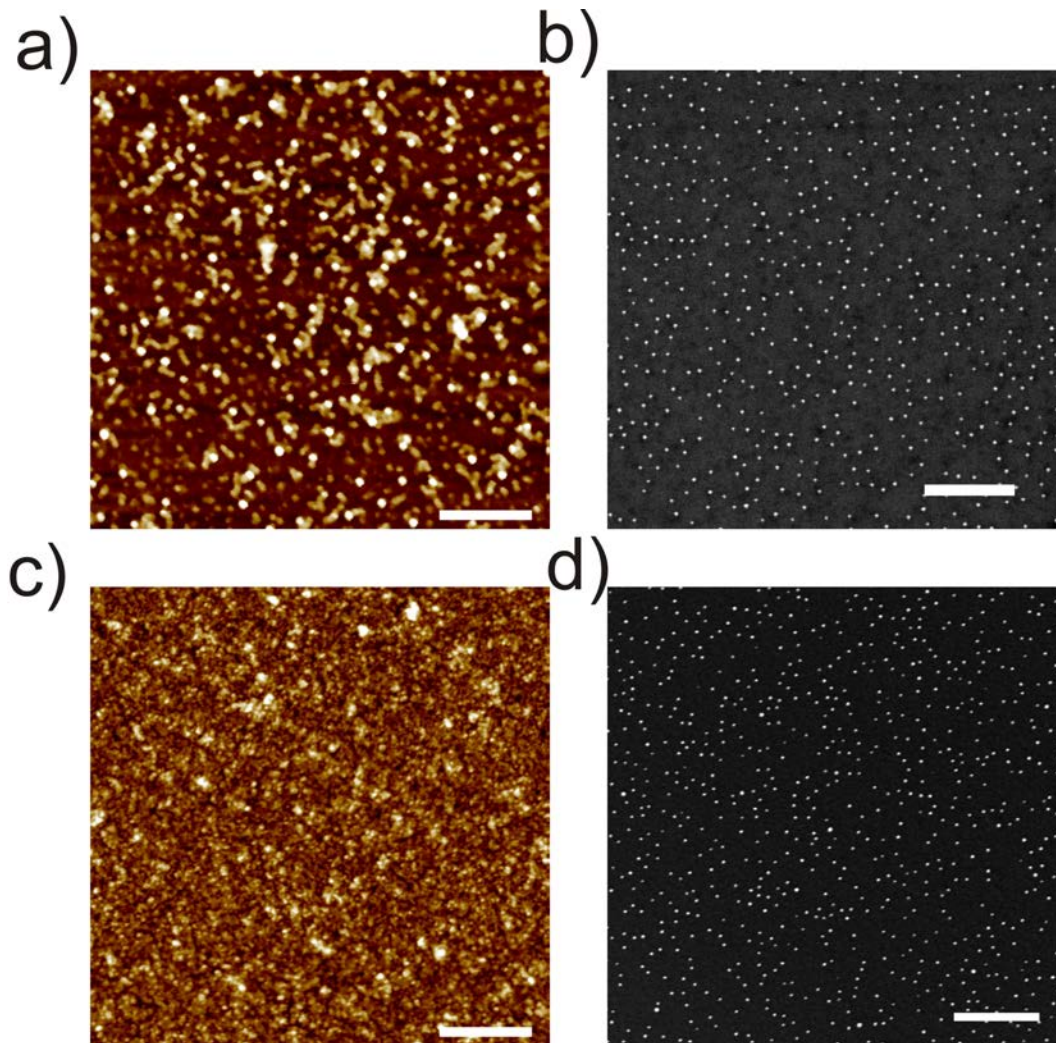


FIGURE 8.5 a) AFM and b) SEM images of silicon surface (hydrophilic) with density of $6500 / \mu\text{m}^2$ Chi-avidin deposition after separate incubation with 5 nm b-AuNPs. The AuNPs are “shiny” in the SEM image. Scale bar 100nm. c) and d) are similar experiment with silicon surface with hydrophobic treatment.

chi-avidin is very similar, around 700 b-AuNPs per square micrometer. Considering the density of chi-avidin on pure silicon is around 6500 per square micrometer, it is easy to calculate that around 9/10 chi-avidin physical adsorption on silicon lose its functionality.

Other interesting observation is that on AFM image (Fig.8.5(a) and (c)), we can clearly see the re-deposition of chi-avidin on hydrophilic surface, which could not be observed on hydrophobic surface. One possible explanation of this re-deposition mechanism is the low affinity of chi-avidin deposition on hydrophilic surface (Fig.8.6). In buffer condition, b-AuNPs could have affinity to several different chi-avidins (proved in the Section 8.1) on the surface. When the surface was dried in air, the PEG armlength of b-AuNPs pull over the chi-avidin inward. For hydrophobic sur-

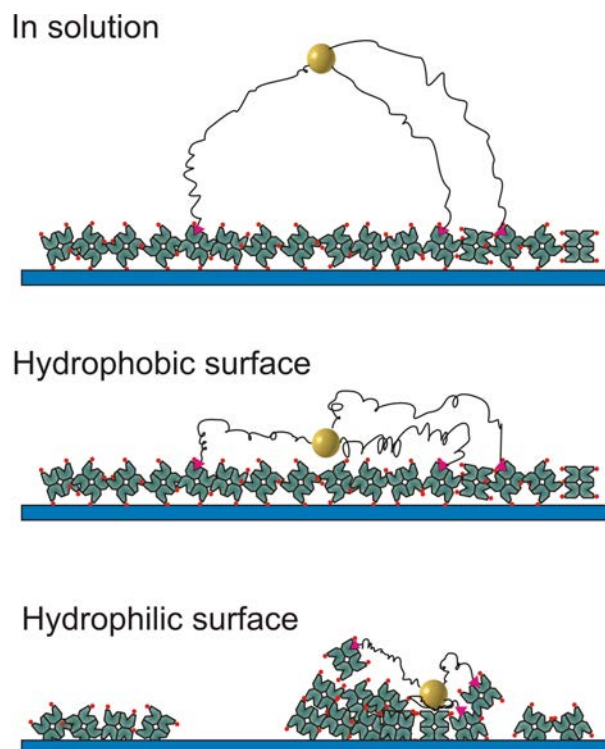


FIGURE 8.6 One possible explanation of re-deposition of chi-avidin on hydrophilic silicon surface rather than on hydrophobic silicon surface.

face, the chi-avidin have stronger affinity which can not easily to form re-deposit. While for hydrophilic silicon surface, the affinity of chi-avidin with silicon surface is much poor, and re-deposition or re-clustering happens.

8.2 Building blocks of the DNA nanoparticle actuator and assembly

In order to build a nanoscale actuator, one needs to choose the material that could be elongated or depressed in a controllable way, while the size should be very small but detectable. The first choice of the material in our Academy project was a single protein (chi-avidin), however, the denaturalization, cluster formation, physical adsorption etc make the system to complicated to analyze. So in reality, single strand DNA was used in the final targeting material, to be controlled under ultra-high external electric field. A challenge was to realize this ultra-high electric field in liquid.

8.2.1 Assembly of DNA nanoparticle actuator

The building blocks of a DNA nanoparticle actuator includes: nChiAVD-Cys (neutral chimeric avidin with cysteine modification), blocking agent (Bovine serum albu-

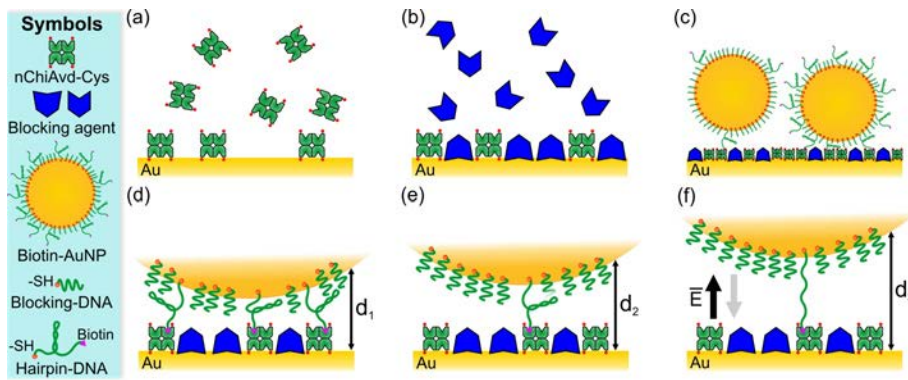


FIGURE 8.7 Schematic illustration of the DNA-AuNP-nanoactuator and SPR characterization of its assembly. (a) Binding of neutral cysteine-tagged chimeric avidins (nChiAvd-Cys) on a gold surface, (b) the passivation of the remaining surface using a blocking agent (BSA or SH-PEG), (c) immobilization of AuNPs functionalized with biotinylated DNA. Linking is former by biotin-avidin binding. (d,e) After immobilization, the biotin-DNA (hairpin-DNA or plain ssDNA) is in a folded state and the particle is located close to the gold surface. The distance d to the surface and the mobility of AuNP are influenced by the number of the linking DNAs, where more bindings indicates less mobility and shorter distance to the gold surface (distance d_1 versus d_2). (f) By applying electric field the DNA hairpin can be opened (or ssDNA straightened) and the particle is pushed away from the surface ($d_3 > d_2$). When the electric field is switched off, the DNA loop can refold. Reprint from A.III

min), 40 nm biotin-AuNPs, SH (poly (ethylene glycol)methyl ether thiol (SH-PEG, Mn=800) and hairpin-DNA (IDT, Coralville, Iowa, USA) .

The schematic illustration of the DNA-AuNPs nanoactuator is shown in Fig.8.7. Here the running buffer used was PBS buffer. First, a thin layer of gold surface with evaporation method was done on plastic surfaces with titanium as sticking layer. nChiAvd-Cys was then injected with the chamber with 0.75mg/ml concentration of 10 mins. nChiAvd-Cys would then form selfassembled thin layer with strong thiol-gold interaction and leaving free labeling biotin binding sites open. 300 ul blocking agents (500ug/ml BSA, or 500ug/ml SH-PEG) was then injected to block uncovered surface to reduce unspecific binding of b-AuNPs on the gold surface. 40 nm B-AuNPs was then injected and constantly monitored with dark field camera. When the concentration of the b-AuNPs was on the correct density, around 10s to 100s B-AuNPs per 100 micrometer square, the incubation of B-AuNPs was stopped. The non-selectivity B-AuNPs and nChiAVD-Cys would then repeatedly be washed away by pure water. All these processes were monitored by reflection angle with SPR characterization.

8.2.2 Ultra high electric field in micrometer scale

Ultra high electric field was added through a parallel capacitor with external DC bias. The parallel capacitor was made of gold surface and indium tin oxide (ITO)

glass (Fig.8.2.2(h)).

In this work, we assumed that in the middle of the chip, where the measurements were carried out, the electric field was uniform. To estimate the electric field strength for DC-voltage in this region, we calculated the distance between the gold surface on silicon chip and the ITO glass above it. This was done by measuring the capacitance C between the plates and calculating the distance d using the plate capacitor equation.8.2.2.

$$C = \frac{\epsilon_0 \epsilon_r A}{d} \quad (8.2)$$

where the ϵ_r is the relative permittivity of air, the ϵ_0 is the absolute permittivity and A is the area of the smaller surface. The applicability of equation 1 can be justified by two assumptions. First, the distance between the plates is much smaller than the size of the plates, which is valid, since the distance should be well under 1 mm and the size of silicon chip is 5.7 mm \times 7.1 mm and the size of the ITO is 18 mm \times 18 mm. Secondly, one of the plates is much larger than the other one, so that the edge effects can be ignored, which is valid since the ITO is considerable larger than the silicon chip. These assumptions mean that the smaller surface (gold surface) sees the larger surface (ITO) as a mirror surface with the same area as the gold surface and twice the distance d from the real, smaller surface. Since the electrostatic energy of this mirror system is twice that of the original system, then the capacitance is half of the original system. Now for the mirror system, the equation.8.2.2 is valid, and since we have twice the distance and half the capacitance and the capacitance of the original system simplify also into the equation.8.2.2.

The capacitance was measured using Wayne Kerr Automatic LCR Meter 4225, where C was 4.1 pF. By inserting the area of the silicon chip, the measured capacitance C and both permittivities into the equation 1, the distance d of 87 $\hat{1}$ /₄m was obtained. For biasing voltage of 1 V, the electric field strength corresponds to 1.15×10^4 V/m.

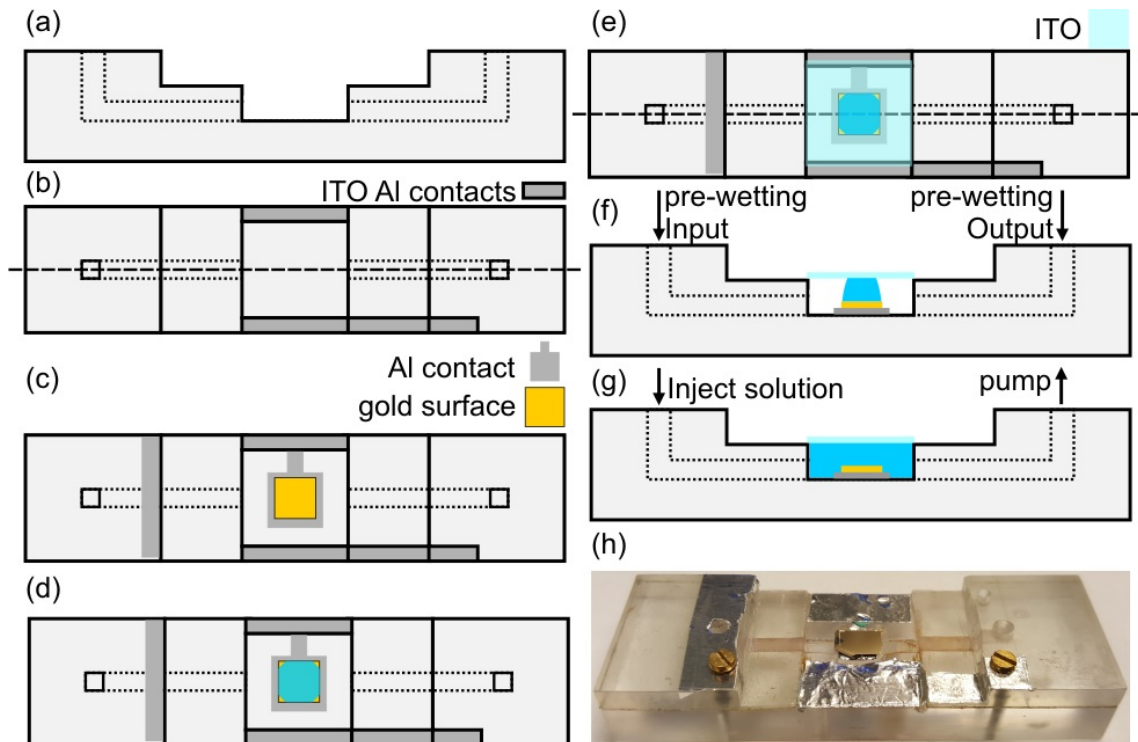


FIGURE 8.8 Schematic illustration of ultra high electric field added with parallel capacitor in water (a) Initial schematic side view of the holder without the aluminum contacts for the silicon chip. Dotted lines indicates the fluid channels. (b) A schematic top view of the holder without aluminum contact, where the dashed line indicates the cross section in (a). (c) In the first step, aluminum contacts were fabricated and the gold coated silicon was clued to the contacts using varnish and silver paste. (d) Chimeric avidin and BSA solution were incubated for 30 min, followed by washing step. (e) Next, the avidin and BSA coated gold surface was sealed into chamber using the ITO cover glass. The cross section of (f) is indicated by the dashed line. (f) A schematic side view of the holder configuration in image (e). The fluid channels are pre-wetted before the AuNP deposition. (g) During the deposition, the AuNP solution was injected to the chamber and let incubate for 15 - 90 min. Then pump was turned on and NaPhos and NaCl buffer was added while pumping the excess liquid away. (h) Image of the sample holder without the ITO cover glass. The length of the holder is 75 mm and the width is 26 mm. Reprinted from A.III

Bibliography

- [1] <http://www.globalsino.com/EM/page4603.html>.
- [2] ABE, K., IWAMOTO, S., AND YANO, H., *Obtaining Cellulose Nanofibers with a Uniform Width of 15 nm from Wood*. *Biomacromolecules* **8** (2007) 3276–3278. PMID: 17784769, <https://doi.org/10.1021/bm700624p>, URL <https://doi.org/10.1021/bm700624p>.
- [3] ARNOLD, M. S., GREEN, A. A., HULVAT, J. F., STUPP, S. I., AND HERSAM, M. C., *Sorting carbon nanotubes by electronic structure using density differentiation*. *Nature Nanotechnology* **1** (2006) 60 EP –. Article, URL <http://dx.doi.org/10.1038/nnano.2006.52>.
- [4] BALAVOINE, F., SCHULTZ, P., RICHARD, C., MALLOUH, V., EBBESEN, T. W., AND MIOSKOWSKI, C., *Helical Crystallization of Proteins on Carbon Nanotubes: A First Step towards the Development of New Biosensors*. *Angewandte Chemie International Edition* **38** 1912–1915.
- [5] BEKYAROVA, E., ITKIS, M. E., CABRERA, N., ZHAO, B., YU, A., GAO, J., AND HADDON, R. C., *Electronic Properties of Single-Walled Carbon Nanotube Networks*. *Journal of the American Chemical Society* **127** (2005) 5990–5995. URL <https://doi.org/10.1021/ja0431531>.
- [6] BINNIG, G., QUATE, C., AND GERBER, C., *Atomic force microscope*. *Physical review letters* **56** (1986) 930–933.
- [7] BUSTAMANTE, C. AND KELLER, D., *Scanning force microscopy in biology*. *Physics Today* **48** (1995) 32–38.
- [8] CHEN, R. J., BANGSARUNTIP, S., DROUVALAKIS, K. A., WONG SHI KAM, N., SHIM, M., LI, Y., KIM, W., UTZ, P. J., AND DAI, H., *Noncovalent functionalization of carbon nanotubes for highly specific electronic biosensors*. *Proceedings of the National Academy of Sciences* **100** (2003) 4984–4989.
- [9] CHEN, R. J., ZHANG, Y., WANG, D., AND DAI, H., *Noncovalent Sidewall Functionalization of Single-Walled Carbon Nanotubes for Protein Immobilization*. *Journal of the American Chemical Society* **123** (2001) 3838–3839.

- [10] COLEMAN, J. N., KHAN, U., BLAU, W. J., AND GUNÂKO, Y. K., *Small but strong: A review of the mechanical properties of carbon nanotubeâpolymer composites*. Carbon **44** (2006) 1624 – 1652.
- [11] DAI, J., ZHANG, J., ZHANG, W., AND GRISCHKOWSKY., D., *Terahertz time domain spectroscopy characterization of the far-infrared absorption and index of refraction of high-resistivity, float-zone silicon*. J. Opt. Soc. Am. B **21** (2004) 1379–1386.
- [12] DE VOLDER, M. F. L., TAWFICK, S. H., BAUGHMAN, R. H., AND HART, A. J., *Carbon Nanotubes: Present and Future Commercial Applications*. Science **339** (2013) 535–539. <http://science.sciencemag.org/content/339/6119/535.full.pdf>.
- [13] FEYNMAN, R. P., *There's Plenty of Room at the Bottom* (1959).
- [14] GREEN, N., *AVIDIN. 1. THE USE OF [14C]BIOTIN FOR KINETIC STUDIES AND FOR ASSAY*. Biochemical Journal **89** (1963) 585–591.
- [15] HELBING, C., STOEBEL, R., HERING, D. A., ARRAS, M. M. L., BOSSERT, J., AND JANDT, K. D., *pH-Dependent Ordered Fibrinogen Adsorption on Polyethylene Single Crystals*. Langmuir **32** (2016) 11868–11877. PMID: 27775351, <http://dx.doi.org/10.1021/acs.langmuir.6b03110>, URL <http://dx.doi.org/10.1021/acs.langmuir.6b03110>.
- [16] HERRANEN, O., *Experimental Characterization of electronic, structure and optical properties of individual carbon nanotubes*, Ph.D. thesis, University of Jyväskylä (2014).
- [17] HERRIG, A., JANKE, M., AUSTERMANN, J., GERKE, V., JANSHOFF, A., AND STEINEM, C., *Cooperative Adsorption of Ezrin on PIP2-Containing Membranes*. Biochemistry **45** (2006) 13025–13034. PMID: 17059219, <http://dx.doi.org/10.1021/bi061064a>, URL <http://dx.doi.org/10.1021/bi061064a>.
- [18] HOUSECROFT, C. E. .-v. AND CONSTABLE, E. C. .-v., *Chemistry : an introduction to organic, inorganic and physical chemistry* (Harlow : Pearson Prentice Hall, 2006).
- [19] HOWARTH, M., CHINNAPEEN, D. J.-F., GERROW, K., DORRESTEIN, P. C., GRANDY, M. R., KELLEHER, N. L., EL-HUSSEINI, A., AND TING, A. Y., *A monovalent streptavidin with a single femtomolar biotin binding site*. Nature Methods **3** (2006) 267 EP –. Article, URL <http://dx.doi.org/10.1038/nmeth861>.
- [20] HYTONEN, V., LAITINEN, O., AIRENNE, T., KIDRON, H., MELTOLA, N., PORKKA, E., HORHA, J., PALDANIUS, T., MAATTA, J., NORDLUND, H., JOHNSON, M., SALMINEN, T., AIRENNE, K., YLA-HERTTUALA, S., AND KULOMAA,

M., *Efficient production of active chicken avidin using a bacterial signal peptide in Escherichia coli*. *Biochemical journal* **384** (2004) 385–390.

- [21] HYTÖNEN, V. P., MÄÄTTÄ, J. A., NISKANEN, E. A., HUUSKONEN, J., HELTUNEN, K. J., HALLING, K. K., NORDLUND, H. R., RISSANEN, K., JOHNSON, M. S., SALMINEN, T. A., KULOMAA, M. S., LAITINEN, O. H., AND AIRENNE, T. T., *Structure and characterization of a novel chicken biotin-binding protein A (BBP-A)*. *BMC Struct Biol* **7** (2007) 8–8. 1472-6807-7-8[PII], URL <http://www.ncbi.nlm.nih.gov/pmc/articles/PMC1831776/>.
- [22] IIJIMA, S., *Helical microtubules of graphitic carbon*. *Nature* **354** (1991) 56 EP –.
- [23] JAVEY, A., GUO, J., WANG, Q., LUNDSTROM, M., AND DAI, H., *Ballistic carbon nanotube field-effect transistors*. *Nature* **424** (2003) 654 EP –. URL <http://dx.doi.org/10.1038/nature01797>.
- [24] JEAN-NOEL FUCHS, M. O. G., *Introduction to the physical properties of graphene* (2008).
- [25] JIANG, K., SCHADLER, L. S., SIEGEL, R. W., ZHANG, X., ZHANG, H., AND TERRONES, M., *Protein immobilization on carbon nanotubes via a two-step process of diimide-activated amidation*. *J. Mater. Chem.* **14** (2004) 37–39. URL <http://dx.doi.org/10.1039/B310359E>.
- [26] JÖRG, R., GANG, W., AND D., J. K., *Formation and Topotactical Orientation of Fibrinogen Nanofibrils on Graphite Nanostructures*. *Advanced Engineering Materials* **11** B177–B181. <https://onlinelibrary.wiley.com/doi/pdf/10.1002/adem.200900084>, URL <https://onlinelibrary.wiley.com/doi/abs/10.1002/adem.200900084>.
- [27] KAISER, A. B., *Electronic transport properties of conducting polymers and carbon nanotubes*. *Reports on Progress in Physics* **64** (2001) 1. URL <http://stacks.iop.org/0034-4885/64/i=1/a=201>.
- [28] KAISER, A. B., DÜSBERG, G., AND ROTH, S., *Heterogeneous model for conduction in carbon nanotubes*. *Phys. Rev. B* **57** (1998) 1418–1421. URL <https://link.aps.org/doi/10.1103/PhysRevB.57.1418>.
- [29] LING, W. L., BIRO, A., BALLY, I., TACNET, P., DENIAUD, A., DORIS, E., FRACHET, P., SCHOEHN, G., PEBAY-PEYROULA, E., AND ARLAUD, G. J., *Proteins of the Innate Immune System Crystallize on Carbon Nanotubes but Are Not Activated*. *ACS Nano* **5** (2011) 730–737. PMID: 21214219, <https://doi.org/10.1021/nn102400w>, URL <https://doi.org/10.1021/nn102400w>.

- [30] LIVNAH, O., BAYER, E. A., WILCHEK, M., AND SUSSMAN, J. L., *Three-dimensional structures of avidin and the avidin-biotin complex*. Proc Natl Acad Sci U S A **90** (1993) 5076–5080. 8506353[pmid].
- [31] LLOYD-HUGHES, J. AND JEON, T.-I., *A Review of the Terahertz Conductivity of Bulk and Nano-Materials*. Journal of Infrared, Millimeter, and Terahertz Waves **33** (2012) 871–925.
- [32] MA, P.-C., SIDDIQUI, N. A., MAROM, G., AND KIM, J.-K., *Dispersion and functionalization of carbon nanotubes for polymer-based nanocomposites: A review*. Composites Part A: Applied Science and Manufacturing **41** (2010) 1345 – 1367. URL <http://www.sciencedirect.com/science/article/pii/S1359835X10002009>.
- [33] MAATTA, J. A. E., EISENBERG-DOMOVICH, Y., NORDLUND, H. R., HAYOUKA, R., KULOMAA, M. S., LIVNAH, O., AND HYTONEN, V. P., *Chimeric Avidin Shows Stability Against Harsh Chemical Conditions-Biochemical Analysis and 3D Structure*. Biotechnology and bioengineering **108** (2011) 481–490.
- [34] MELITZ, W., SHEN, J., KUMMEL, A. C., AND LEE, S., *Kelvin probe force microscopy and its application*. Surface Science Reports **66** (2011) 1 – 27.
- [35] MINOT, E. D., *Tuning the band structure of carbon nanotubes*, Ph.D. thesis, Cornell University (2004).
- [36] M.MEYYAPPAN, *Carbon nanotubes science and applications* (CRC PRESS, 2005).
- [37] MTSUKO, D., *Experimental study of electron transport in mesoscopic carbon based nanostructures*, Ph.D. thesis, University of Jyväskylä (2012).
- [38] MTSUKO, D., KOSHIO, A., YUDASAKA, M., IIJIMA, S., AND AHLKOG, M., *Measurements of the transport gap in semiconducting multiwalled carbon nanotubes with varying diameter and length*. Phys. Rev. B **91** (2015) 195426. URL <https://link.aps.org/doi/10.1103/PhysRevB.91.195426>.
- [39] NOVOSELOV, K. S., GEIM, A. K., MOROZOV, S. V., JIANG, D., ZHANG, Y., DUBONOS, S. V., GRIGORIEVA, I. V., AND FIRSOV, A. A., *Electric Field Effect in Atomically Thin Carbon Films*. Science **306** (2004) 666–669. <http://science.sciencemag.org/content/306/5696/666.full.pdf>, URL <http://science.sciencemag.org/content/306/5696/666>.
- [40] RADUSHKEVICH, L. AND LUKYANOVICH, V. J. Phys. Chem. Russia **1** (1952) 88.
- [41] RESNICK, A., *Introduction to Experimental Biophysics: Biological Methods for Physical Scientists*, by Jay Nadeau. Contemporary Physics **53** (2012).



- [42] SCHÄÖNENBERGER, C., *Bandstructure of Graphene and Carbon Nanotubes: An Exercise in Condensed Matter Physics* (2000).
- [43] SHAO, D., TAPIO, K., AUER, S., TOPPARI, J. J., HYTÖNEN, V. P., and Ahlskog, M., *Surface Characterization of Carbon Nanotubes*. [//DOI.ORG/10.1021/ACS.LANGMUIR.8B02855](https://doi.org/10.1021/acs.langmuir.8b02855).
- SHAO, D., YOTPRAYOONSAK, P., SAUNAJOKI, V., AHLKOG, M., VIRTANEN, J., KANGAS, V., VOLODIN, A., HAESSENDONCK, C. V., BURDANOVA, M., MOSLEY, C. D. W., AND LLOYD-HUGHES, J., *Conduction properties of thin films from a water soluble carbon nanotube/hemicellulose complex*. *Nanotechnology* **29** (2018) 145203. <http://stacks.iop.org/0957-4484/29/i=14/a=145203>.
- SHENG, P., *Fluctuation-induced tunneling conduction in disordered materials*. *Phys. Rev. B* **21** (1980) 2180–2195. <https://link.aps.org/doi/10.1103/PhysRevB.21.2180>.
- SHULAKER, M. M., HILLS, G., PATIL, N., WEI, H., CHEN, H.-Y., WONG, H. S. P., AND MITRA, S., *Carbon nanotube computer*. *Nature* (2013).
- STEIGERWALD, D. M. D., *New Detection System for LEO FE-SEM, Ultra Low Voltage BSE Imaging*.
- Thermo Science Company, *Thermo Scientific Avidin-Biotin Technical Handbook*.
- THOSTENSON, E. T., REN, Z., AND CHOU, T.-W., *Advances in the science and technology of carbon nanotubes and their composites: a review*. *Composites Science and Technology* **61** (2001) 1899 – 1912.
- TSEBRO, V. I., TONKIKH, A. A., RYBKOVSKIY, D. V., OBRAZTSOVA, E. A., KAUPPINEN, E. I., AND OBRAZTSOVA, E. D., *Phonon contribution to electrical resistance of acceptor-doped single-wall carbon nanotubes assembled into transparent films*. *Phys. Rev. B* **94** (2016) 245438. <https://link.aps.org/doi/10.1103/PhysRevB.94.245438>.
- VALIMAA, L., *Streptavidin- A versatile binding perotein for solid phase immunoassays*, Ph.D. thesis, University of Turku (2008).
- YAMAMOTO, D., NAGURA, N., OMOTE, S., TANIGUCHI, M., AND ANDO, T., *Streptavidin 2D Crystal Substrates for Visualizing Biomolecular Processes by Atomic Force Microscopy*. *Biophys J* **97** (2009) 2358–2367. BPJ987[PII], <http://www.ncbi.nlm.nih.gov/pmc/articles/PMC2764062/>.
- YOTPRAYOONSAK, P., *Complexes of carbon nanotubes with ions and macromolecules; Studies on electronic conduction properties*, Ph.D. thesis, University of Jyväskylä (2014).
- ZAUER, D., TASKINEN, B., EICHINGER, D., FLATTINGER, C., RUTTMANN, B., KNOGLINGER, C., TRAXLER, L., EBNER, A., GRUBER, H. J., AND HYTÖNEN, V. P., *Regenerative biosensor chips based on switchable mutants of avidin—A systematic study*. *Sensors and Actuators B: Chemical* **229** (2016) 646 – 654. <http://www.sciencedirect.com/science/article/pii/S0925400516301885>.

ZHUKOVA, E. S., GREBENKO, A. K., BUBIS, A. V., PROKHOROV, A. S., BELYANCHIKOV, M. A., TSAPENKO, A. P., GILSHTEYN, E. P., KOPYLOVA, D. S., GLADUSH, Y. G., ANISIMOV, A. S., ANZIN, V. B., NASIBULIN, A. G., AND GORSHUNOV, B. P., *Terahertz-infrared electrodynamics of single-wall carbon nanotube films*. *Nanotechnology* **28** (2017) 445204.

**Conduction properties of thin films
from a water soluble carbon
nanotube/hemicellulose complex
(Nanotechnology)**

A.I

Conduction properties of thin films from a water soluble carbon nanotube/hemicellulose complex

Dongkai Shao¹, Peerapong Yotprayoosak^{1,5,6}, Ville Saunajoki¹, Markus Ahlskog^{1,6} , Jorma Virtanen², Veijo Kangas², Alexander Volodin³, Chris Van Haesendonck³, Maria Burdanova⁴, Connor D W Mosley⁴ and James Lloyd-Hughes⁴ 

¹ Nanoscience Center, Department of Physics, University of Jyväskylä, FI-40014, Finland

² XYNAC Inc., 4275 Fulton Road NW, Canton, OH 44718-2821, United States of America

³ Katholieke Universiteit Leuven, Afdeling Vaste-stoffysica en Magnetisme, Celestijnenlaan 200D, B-3001 Leuven, Belgium

⁴ Department of Physics, University of Warwick, Gibbet Hill Road, Coventry, CV4 7AL, United Kingdom

E-mail: peyotpra@gmail.com and markus.e.ahlskog@jyu

Received 25 October 2017, revised 24 January 2018

Accepted for publication 31 January 2018

Published 20 February 2018



CrossMark

Abstract

We have examined the conductive properties of carbon nanotube based thin films, which were prepared via dispersion in water by non-covalent functionalization of the nanotubes with xylan, a type of hemicellulose. Measurements of low temperature conductivity, Kelvin probe force microscopy, and high frequency (THz) conductivity elucidated the intra-tube and inter-tube charge transport processes in this material. The measurements show excellent conductive properties of the as prepared thin films, with bulk conductivity up to 2000 S cm^{-1} . The transport results demonstrate that the hemicellulose does not seriously interfere with the inter-tube conductance.

Keywords: carbon nanotubes, hemicellulose, thin films, terahertz, electronic transport

(Some figures may appear in colour only in the online journal)

1. Introduction

Mixtures of cellulose and carbon nanotubes (CNT) are usually comprehended as composites, where the cellulose forms the host matrix and CNTs as filler material enhance the electrical and thermal conductivity as well as the strength properties. Such composites have been studied lately due to their potentially useful applications such as sensors, actuators and electrostatic dissipation/electromagnetic interference shielding materials [1–7]. They are normally prepared by separately dispersing the cellulose and the CNT material and then mixing the two dispersions.

However, as has been reported in a few works [8–12], non-covalently bound cellulose can be utilized as a dispersant

(similar to surfactant molecules [13]) to disperse CNTs in water. Here, the cellulose polymer molecules form complexes with the CNTs, whose accurate nature is still under debate and study [11, 14]. Processability of CNTs via dispersion in water has obvious advantages with respect to environmental concerns, and enhances the prospects for scaled-up production of CNT based devices.

The method of using cellulose polymer as a dispersant can still be used to prepare CNT/cellulose composites, as surplus cellulose can freely be mixed and thus the CNT content can be varied. CNTs are attractive in the field of composite technology as a very small content of CNTs, in the range of 0.01%–10%(wt) can percolate throughout the host matrix. On the other hand, in CNT materials that have been prepared by dispersing in water the CNT/cellulose complex (and not adding any extra cellulose), the CNT content in the processed material can be around 50%(wt). As the role of the

⁵ Current address: Department of Physics, Faculty of Liberal Arts and Science, Kasetsart University (Kamphaeng Saen Campus), Nakhon Pathom 73140, Thailand.

⁶ Authors to whom any correspondence should be addressed.

cellulose is solely that of a dispersant, then usually the cellulose is to be considered a nuisance for the end purpose, and therefore the material is a dispersion and not a composite, although the concepts and vocabulary seem to be somewhat varying in the research literature on this developing topic. For electronic applications, dispersions of CNT materials (often single wall carbon nanotubes, SWNT) are processed into different types of conductors, which range from truly 2D networks to essentially 3D films and fibers. A prime example is the fabrication of conductive transparent thin films [15].

CNT materials that have been prepared with inclusion of dispersants are thus not true composites; the CNT content is far above any percolation threshold. Nevertheless, in electronic applications the tube–tube interconnectivity is crucial and is easily interrupted if the tubes are complexed with molecular species. Even without this complication, and the fact that normally, CNT material is a mixture of metallic and semi-conducting tubes, it is very difficult to model satisfactorily charge transport in bulk CNT materials. As is usually discussed [16–18], the conduction process can be divided into intra- and inter-tube resistance. The difficulty is then that the inter-tube conduction processes are not well known in macroscopic assemblies of CNT, but are usually presumed to occur at specific locations where crossing tubes are mechanically connecting each other. The inter-tube resistance is most simply described as dependent on an activation energy, and the total resistance can be thought to be the result of a network of resistors where usually the inter-tube resistance dominates [19]. However, many works also apply variable range hopping theories that do not directly build on mechanical network connectivity [20, 21].

To our knowledge, there is no comprehensive study of transport properties in thin films of CNT/cellulose complex, where the role of cellulose is explicitly that of a dispersant. Hamedi *et al* [11] reported nanocellulose dispersed CNT films, or composites, with a conductivity on the order of 100 S cm^{-1} , which is a rather high level, but lower than what is reported for pure SWNT materials [22]. An effective method for dispersing CNTs using hemicellulose (hc) (Xylan) as a dispersant material has previously been reported by two of the authors in a patent [23]. In this paper, we report on transport measurements in thin films consisting of CNT-hc prepared using this method. These include low temperature transport, high frequency (THz) conductivity measurements, and Kelvin probe force microscopy (KPFM) measurements of the local conductive properties on the current carrying CNT-hc devices. Computational and experimental studies on the microscopic nature of this complex will be reported in a companion paper.

2. Experimental methods

2.1. Sample fabrication

We used double wall carbon nanotubes (DWNT) material from Unidym Co. (USA)⁷, which according to the manufacturer has

an average length of $2 \mu\text{m}$, diameters in the range 2–3 nm, and purity of $>50 \text{ wt}\%$. The commercially obtained xylan, that is the hc, was an extract from beech tree⁸. CNT-hc dispersion was prepared by adding a mixture of 100 mg DWNTs, and 1 ml 2-propanol into 100 ml of water. The mixture was sonicated for 1 min using a 300 W sonicator (cooling was not considered to be necessary). Xylan (100 mg) was added in four 25 mg portions, while sonicating for 4 min between each addition. 10 ml of this dispersion was diluted with 390 ml of water, and sonicated further for 4 min. The diluted dispersion containing 25 mg DWNTs, 25 mg xylan in one liter of water was used as such for all experiments. This CNT-hc dispersion was stable for at least one year at $+4 \text{ }^\circ\text{C}$, which is demonstrated in figure 1(a). Imaging of depositions of this dispersion with scanning probe and electron microscopy shows that it contains individual and still some bundles of tubes with diameters up to around 10 nm.

CNT-hc films were deposited by either spin casting or drop-dry casting the dispersion on pieces of commercially purchased highly doped silicon wafer which had a 300 nm thick silicon oxide insulation layer. In most cases electrodes were fabricated on these prior to deposition of CNT-hc. The spinning speed (from 1000–6000 rpm) was varied in order to obtain different film thicknesses. For thicker films the drop-dry casting method was used, and the thickest films ($>100 \text{ nm}$) were obtained by multiple castings. Prior to the deposition of the CNT-hc, it was found helpful to slightly hydrophilize the silicon oxide surface by a gentle treatment with O_2 plasma (Oxford RIE). To measure the film thickness we produced a sharp edge through it by brushing the film with a wet cotton stick. The step height at the edge was measured with AFM, as is shown in figure 1(c).

The fastest spinning speeds of small amounts of solution did not produce continuous films but instead individual tubes and fragments of CNT networks. We prepared microelectrode structures that were used to catch some of these network fragments for two-point conductivity measurements.

The following different experiments were undertaken:

- (i) Low temperature DC-conductivity measurements of macroscopic thin films in four-point electrode configuration, and of micron-sized CNT network fragments in two-point configuration. The electrode structures for the former were $\sim 2 \text{ mm}$ wide and had a spacing of $\sim 100 \mu\text{m}$ between adjacent electrodes. The latter were measured with microelectrode structures shown in figure 1(d). Microelectrodes of different sizes were used, but a width of $50 \mu\text{m}$ and separation of $5 \mu\text{m}$ was typical.
- (ii) KPFM measurements of the potential distributions in current-carrying CNT-hc devices with the same microelectrode structure as in (case 1).
- (iii) Spectroscopic measurements of the high frequency conductivity at THz frequencies of CNT-hc thin films on plain Si substrates.

⁷ Unidym Inc, 1244 Reamwood AVE, Sunnyvale, CA 94089, United States of America.

⁸ Symrise Bio Actives GmbH, Porgesring 50, 22113 Hamburg, Germany.

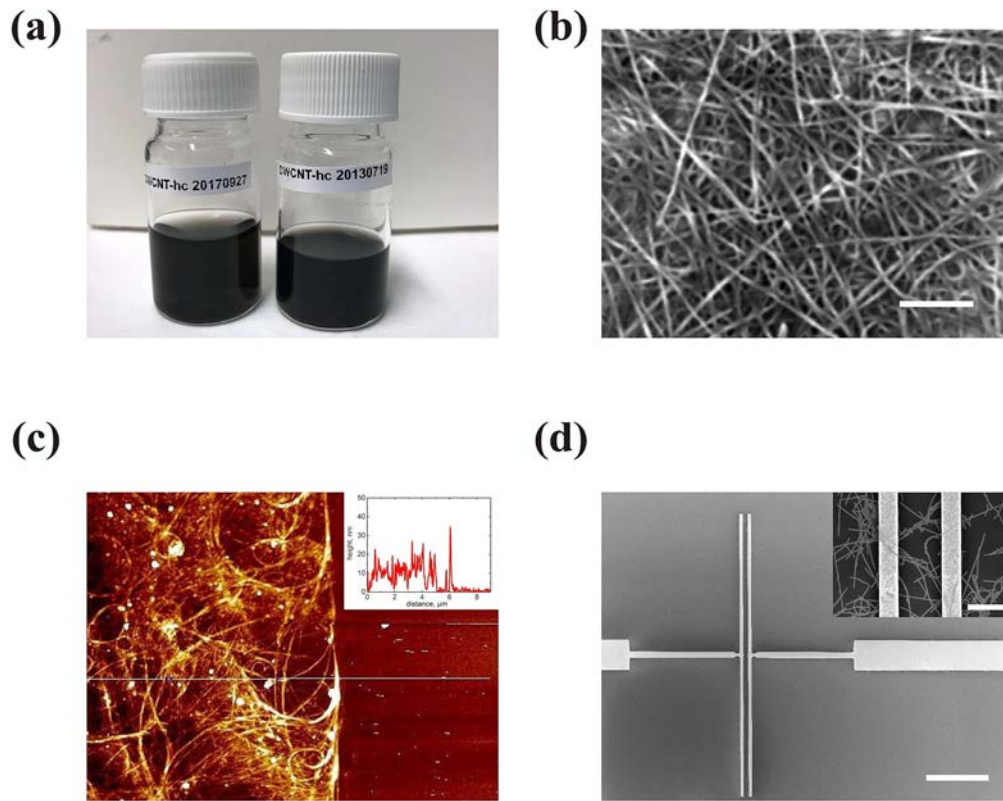


Figure 1. (a) Demonstration of the stability of typical carbon nanotube-hemicellulose (CNT-hc) dispersions. The bottle on the left side is weeks old, while the one on the right side is four years old, and does not have any visible precipitation of CNT-hc complex. (b) SEM image of (CNT-hc) thin film. Scale bar 200 nm. (c) AFM image of a spin coated CNT-hc film, where the sharp edge has been created as explained in the text. The inset shows height profile data across the edge along the line superimposed on the AFM image. (d) SEM image of a microelectrode structure for measuring CNT-hc network fragments. Scale bar 10 μm . Inset: close-up of electrodes with tubes visible. Scale bar 3 μm .

The macroscopic electrodes (case 1) were fabricated by depositing gold (Au), using an e-beam evaporator through a mechanical mask in an ultra-high vacuum chamber, while the microelectrodes (case 1, 2) were fabricated by conventional electron beam lithography (Raith e-LiNE). The Au electrode thickness of the latter was 40 nm, and had 5 nm Ti film as the adhesion layer. The samples were attached onto chip carriers, and bonded with aluminum wires for electrical connection to the measurement apparatus. The highly doped silicon substrate could be connected as a back-gate electrode, which was used especially for the microelectrode samples (figure 1(d)). The high frequency measurements (case 3) were done on high-resistivity float-zone silicon [24] that does not absorb THz radiation.

2.2. Measurements

The low temperature conductivity was measured with standard DC-techniques both for macroscopic thin films (case 1) and the network fragments (case 2) in the temperature range 4.2–300 K. For the measurements we used a 4 K He-bath cryostat with the sample inside a closed vacuum can.

KPFM measurements on the current carrying CNT-hc devices were performed in air using an Agilent 5500 scanning probe microscope using the amplitude modulation KPFM in a single-pass double frequency mode [25]. For the topographic

images acquisition the first resonance of the cantilever at 67 kHz was used and for KPFM frequencies in the range 10–30 kHz were used for the V_{AC} of 1.5 V bias between the tip and sample. For the KPFM measurements presented in the manuscript a probe with the evaluated tip apex radius of 7 nm \pm 2 nm was selected from commercial PPP-EFM probes (nanosensors) having Pt/Ir conductive coating. The tip apex radius was evaluated according [26] by AFM imaging of DWNTs with diameter in the 2–4 nm range deposited on the atomically flat Au(111) crystalline terraces. All measurements were carried out under dry N_2 atmosphere. During the measurements a voltage of $\pm(1-6)$ V is applied between the CNT-hc device electrodes.

Terahertz time-domain spectroscopy was used to measure the THz radiation transmitted through the CNT-hc films, and the bare silicon [27]. The complex, frequency-dependent conductivity $\sigma(\omega) = \sigma_1(\omega) + i\sigma_2(\omega)$ of the CNT-hc films was calculated from

$$\sigma(\omega) = \frac{1 + n_s}{Z_0 \delta} \left(\frac{1}{T(\omega)} - 1 \right), \quad (1)$$

where n_s is the refractive index of the silicon substrate, Z_0 is the impedance of free space, δ is the thickness of the film and $T(\omega)$ is the experimental complex transmission [27]. The effective conductivity of the CNT-hc film was obtained over a

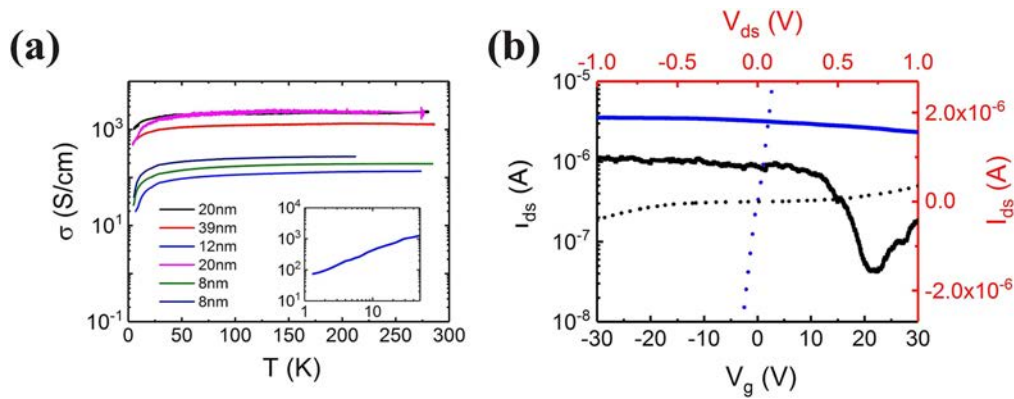


Figure 2. (a) Temperature dependence of the conductivity of CNT-hc films with different thicknesses. Inset: 1 K data in log scale of the 12 nm sample. (b) Low temperature ($T = 4.2$ K) measurements of I versus V_{ds} (top and right axis, red color) and I versus V_g (bottom and left axis) of two typical CNT-hc network fragments. Electrode separations were $3 \mu\text{m}$ (black line) and $5 \mu\text{m}$ (blue line).

frequency range from 0.2–2.5 THz, limited by the bandwidth of the THz pulses detected. Transmission spectra were also obtained from 6.0 to 20.0 THz using a commercial FTIR to better constrain the CNT-hc films' absorption.

3. Results

3.1. DC-conduction measurements

Figure 1(b) shows an SEM image of a typical CNT-hc thin film. The temperature dependent conductivity of six thin film samples is shown in figure 2(a) with thicknesses in the range 8–40 nm. The room temperature conductivity of the thicker films is quite high, up to $2 \times 10^3 \text{ S cm}^{-1}$. On the other hand, thinner films (< 20 nm) are less conductive. The conductivity of all samples is relatively constant down to 50 K, but starts to decrease more rapidly below 10 K. At room temperature, all CNT-hc samples exhibit Ohmic behavior with a linear drain-current (I_{DS}) response. At 4.2 K, the response becomes slightly nonlinear, but there is no gate dependence when tested from a back-gate configuration.

The inset of figure 1(d) shows a close-up image of how the CNTs or CNT network fragments are randomly placed on top of the electrode gap. We present here data from two representative sample of a total of 6 measured samples. Randomly aligned single CNTs in most cases do not directly cross the gap. SEM inspection reveals that usually a few CNT junctions are required to cross the electrode gap, though in this way little can be said about the electrical connectivity. Figure 2(b) displays gate electrode controlled current and IV -curves at 4.2 K from the two typical CNT-hc network fragments, measured over a $2.5 \mu\text{m}$ gap. A small but clearly discernible transport gap is seen in the other sample while its conductance is practically independent from external electric field. The former has a low temperature (zero-bias) resistance of $50 \text{ k}\Omega$ while the latter has c. $5 \text{ M}\Omega$. copic thin films, at low temperatures a clearly discernible nonlinearity appears in the IV -characteristics (at $V_g = 0$). The two samples are different but together they represent well the variation among the samples.

3.2. Kelvin Probe microscopy measurements

A representative example of KPFM measurements for one of the microelectrode structure with $20 \mu\text{m}$ wide electrodes is presented next. The AFM topography and corresponding KPFM images of the inter-electrode region of the current-carrying device acquired at different scan scales are shown in figures 3(a), (b) and 4(a), (b), respectively. The larger scale, low resolution KPFM image (figure 3(b)) clearly indicates that the electric potential along the electrode gap drops almost uniformly. To verify whether the current is running uniformly through this electrode gap region we present in figure 3(c) the local potential profiles within it and parallel to the electrodes. Profile A indicates that the potential has a linear drop almost uniformly along the electrode gap region. On the other hand, profile B indicates that there are equipotentials parallel to the electrodes direction. These results demonstrate that the CNT-hc network film behaves as a uniform conductor at scales larger than $10 \mu\text{m}$. The situation changes dramatically at smaller scales. The higher resolution KPFM image reveals considerably non-uniform potential drop behavior. A representative example of a $2 \times 2 \mu\text{m}^2$ KPFM image is shown in figure 3(b). The visualized potential distribution clearly correlates with the topography image (figure 4(a)). The profiles A and B in figure 4(c) taken along the current carrying CNT fragments demonstrate that the potential drops mainly at the intertube contacts (labeled by the white arrows in figure 4(a)). Nevertheless, it should be noted that there are crossings of current-carrying CNTs with practically undistinguishable (within the noise level) drop values, (see profile C in figure 4(c)), which correspond to relatively low intertube resistances.

3.3. THz time-domain spectroscopy

We obtained the complex conductivity of films with the thicknesses 130, 470, and 1170 nm. As shown in figure 5(a), the real conductivity σ_1 (blue points) at room temperature for the 130 nm film has a weak frequency dependence, with a resonance peaked at around $\omega_0/2\pi$. The DC limit to σ_1 is around 2000 S cm^{-1} , in agreement with the DC transport

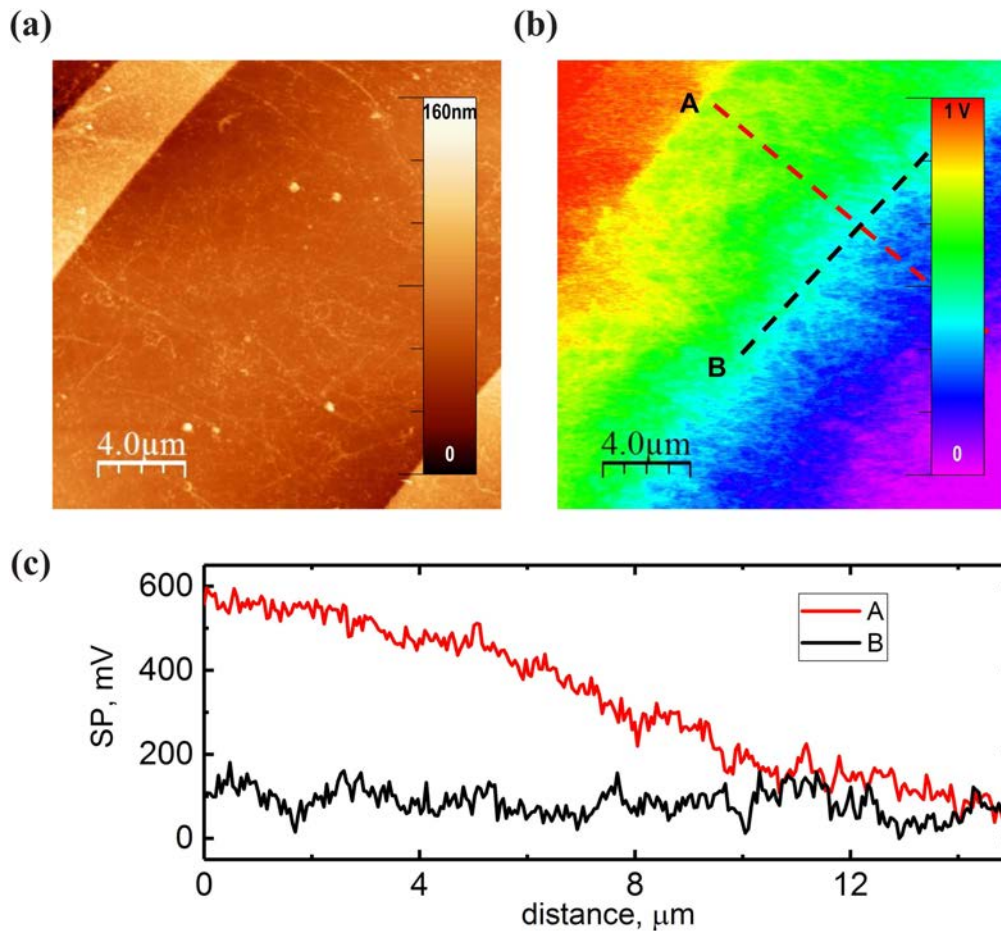


Figure 3. $20 \times 20 \mu\text{m}^2$ AFM topography (a) and KPFM surface potential (SP) images of the CNT-hc device in the current carrying state (b). Local SP profiles (c) taken across the dashed lines. The profile curves have been vertically offset for clarity.

results in figure 2. A suppressed imaginary conductivity σ_2 (red points) is clearly seen at low frequencies. Similar resonant behavior can be seen for the 470 nm film in figure 5(b).

4. Discussion

Simple performance criteria for the conductive properties of CNT composites are the room temperature conductivity σ and the resistivity ratio $R_R = \rho(4.2 \text{ K})/\rho(300 \text{ K})$. As even for the thinner films $\sigma \sim 100 \text{ S cm}^{-1}$, and $R_R < 10$, the thin film of CNT-hc complex material of this work exhibit a relatively high conductivity which is comparable to pure SWNT material [16, 17, 20, 28]. Therefore, the presence of the hc does not seem to be detrimental to the charge transport properties, and we do not consider the hc component as an *a priori* dominating factor of the conduction process, e.g. as determining the intertube connectivity. However, even in pure bulk SWNT or DWNT material, the transport properties are mainly interpreted in terms of a conduction process between the tubes. In the discussion that follows, we demonstrate how the different measurements illuminate the conductivity of our CNT-hc materials from this point of view.

The KPFM measurements probe in a most concrete manner the relation between the morphology of the current-carrying

CNT-hc thin films and the conductivity. The KPFM images reveal a uniform network of CNT-hc with an average length of $\sim 0.6 \mu\text{m}$ between the crossings of CNTs. The measurements strongly suggest that at the microscopic level the voltage drop in crossed current-carrying CNTs concentrates to the tube-tube contacts. However, the measurements bring to light two types of voltage drops in the junctions between crossed current-carrying CNTs: a pronounced voltage drop and a relatively low level voltage drop, which correspond to relatively high and low intertube resistances, respectively. The high resistances could be explained by random occurrences of thin insulating hc layer between the contact points of the CNTs junction. The inspection of 17 regions of $2 \times 2 \mu\text{m}^2$ size of the scanned area reveals the presence of at least two low resistive CNT junctions in $\sim 70\%$ of the regions. Because of the uniform structure CNT-hc in the thickness direction, the translation of the observed surface potential structure is justified. From the KPFM measurement data, we can judge that high conductivity in the composite CNT-hc films is dominated by the low intertube contact resistances, that are not interrupted by an insulating hc layer.

The low temperature conductance measurements on microelectrode structures also directly illuminate the relation between properties at the single tube level and the macroscopic conductivity. In figure 1(d) we presented such with a few nanotubes electrically connecting the electrode gaps

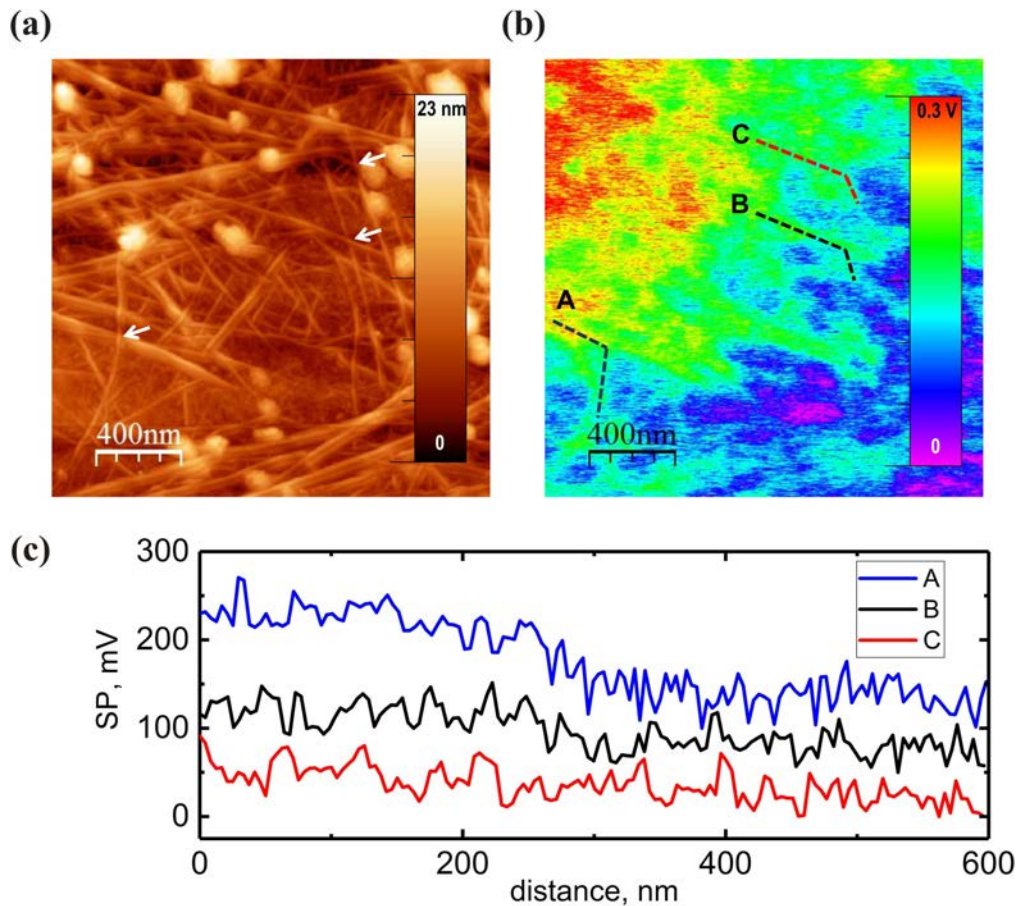


Figure 4. Higher resolution $2 \times 2 \mu\text{m}^2$ AFM topography (a) and KPFM SP images of the CNT-hc device in the current carrying state (b). The profile curves have been vertically offset for clarity. Local SP profiles (c) taken across the dashed lines in (b). The white arrows in (a) indicate the (tube–tube) contacts at which the potential drops occur.

individually or in random chains (we, however, did not count the tubes individually). The strong sample-to-sample variation stems trivially from the random deposition which gives a very fluctuating number and orientation of a few interconnected nanotubes, and thus also a strongly varying number of tube–tube junctions connecting the electrodes. Moreover, the unsorted DWNTs have a distribution of different chiralities and thus a mix of metallic and semiconducting tubes. The semiconducting character and their fluctuating appearance are manifest in the variation of the strength of the field-effect in the microelectrode samples.

The measurements on the microelectrode structures show the resistance to vary from a few 10s of $\text{k}\Omega$ to a few $\text{M}\Omega$, and could conceivably be explained by the more conducting sample being dominated by metallic tubes and the other by semiconducting ones. In figure 2(b) the sample with the smaller resistance of a few 10s of $\text{k}\Omega$, which is roughly independent of the gate voltage and about one order of magnitude larger than the single tube resistance in the ballistic limit of $6.5 \text{ k}\Omega$. This is compatible with the conduction being determined by tube–tube junctions between metallic tubes. The nonlinearity in the low temperature I – V curve (figure 2(b)) could then be due to Coulomb blockade effects due to barriers at tube–tube or electrode–tube junctions. A Coulomb charging energy of a few meVs is consistent with

the transport data. For the more resistive sample, which has a clear transport gap in the I – V_g curve, a semiconducting bandgap, which in DWNTs is $<0.5 \text{ eV}$, is likely the main factor determining the conductivity [29].

Next, we shift to the measurements on macroscopic thin films. In this kind of material, the high frequency measurements can yield information on the intra-tube conduction processes. The optical conductivity of CNTs at far-infrared and THz frequencies has been studied in depth in the literature [22, 27, 30].

A reduced, or even a negative, imaginary conductivity (figure 5) is a signature of the motion of spatially-confined charges within an effective medium. This resonant behavior can be alternatively thought of as an axial plasmon where electrons oscillate along the CNTs length. For SWNTs, careful studies of the dependence of this far-infrared absorption peak on the CNT length [30] and on separated plasmonic and semiconducting SWNTs [22] have supported the plasmonic picture of AC conductivity. Experimentally-derived conductivity spectra can be modeled as the sum of a plasmon resonance term, corresponding to the finite optical conductivity of electrons in individual CNTs, and by a Drude term $\sigma_D(\omega) = \sigma_D/(1 - i\omega\tau_D)$ representing mobile carriers that undergo percolative transport throughout the CNT-hc network with DC conductivity σ_D and scattering time τ_D .

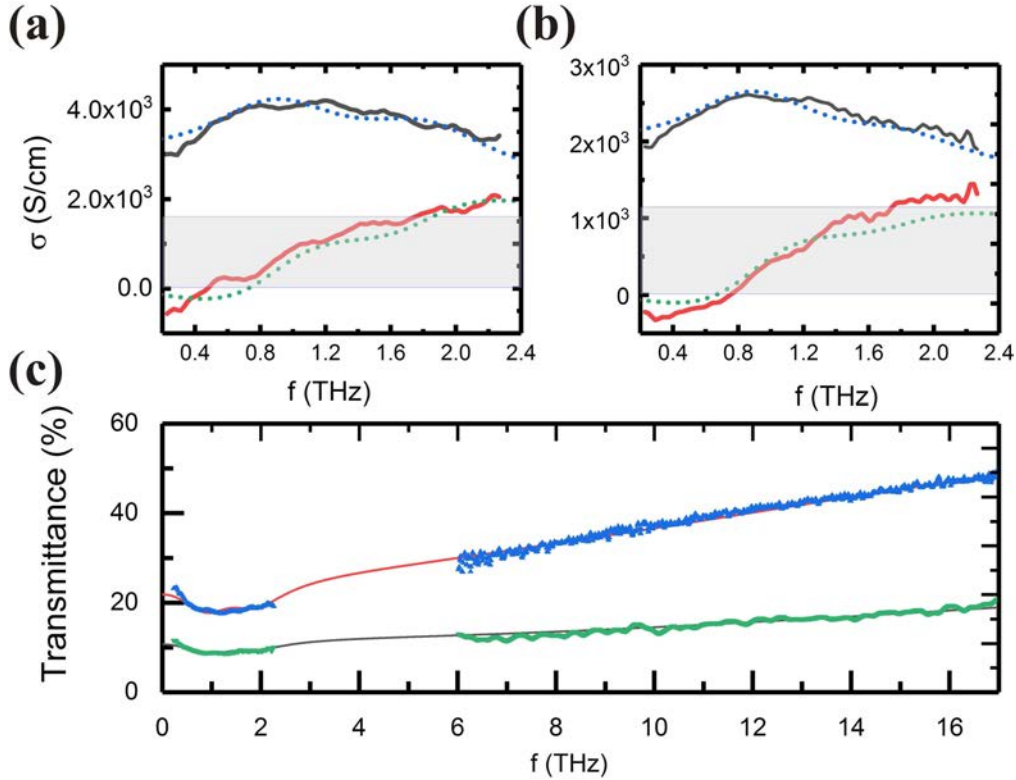


Figure 5. (a) Real (black lines) and imaginary (red lines) conductivity of a 130 nm CNT-hc film. (b) Similarly, for the 470 nm film. The dashed lines are fits as described in the text. The blue shaded areas show the contributions of the Drude term to the real part of the conductivity. (c) Measured (blue and green points) and modeled (red and black lines) amplitude transmission spectra from THz-TDS (left) and FTIR (right).

The complex conductivity $\sigma(q, \omega)$ for axial plasmons in CNTs was obtained from the Boltzmann transport equation in the relaxation time approximation [31], and depends on the wavevector q of the plasmon excited, its scattering time τ , and the Fermi velocity $v_F \sim 8 \times 10^5 \text{ m s}^{-1}$. The overall optical response of a single SWNT was found to be well approximated by that of a single axial plasmon: the fundamental resonance, with $q = \pi/L$ for tube length L . The plasmon frequency is given by $\omega_0 = v_q \pi/L$, where v_q is the plasmon mode velocity, which is a weak function of L [31]. This functional dependence of ω_0 on L has been reported for SWNTs, where for instance $\omega_0/2\pi \sim 2.7 \text{ THz}$ for $\sim 1 \mu\text{m}$ long SWNTs with a 2 nm diameter [30]. In a defect-free linear CNT, L should correspond to the physical length of the CNT. However, in real CNTs $2L$ is instead the plasmon wavelength, and L can be interpreted as the mean distance along the axis before an interruption (e.g. another tube, or a sharp bend in the CNT) occurs. The total conductivity of an effective medium consisting of an ensemble of CNTs can therefore be modeled as

$$\sigma(\omega) = \frac{\sigma_D}{1 - i\omega\tau_D} + \sum_j \frac{A_j(-i\omega + 1/\tau_j)}{(-i\omega + 1/\tau_j)^2 + (v_F q_j)^2}, \quad (2)$$

where the first term captures any possible long-range, percolative transport, for instance via CNT bundles or adjoining unbundled CNTs. The second term contains a sum over all possible plasmon wavevectors q_j , which in the single plasmon

approximation, namely that $q_j = \pi/L_j$, amounts to a sum over all possible lengths L_j . The amplitude term A_j represents the relative number of CNTs with that particular active length, and an average over all possible orientations.

Here, we used two such resonances with $L_1 = 220 \text{ nm}$, $L_2 = 450 \text{ nm}$ and $\tau_1 = \tau_2 = 300 \text{ fs}$ for both samples in order to model the THz conductivity spectrum, shown as the solid lines in the figure 5. These parameters were held the same for the different thickness samples: the active lengths and scattering time should be properties of the CNT-hc and should not vary substantially with film thickness. The amplitude terms were $A_{1,2} = (7.1, 10.0) \times 10^{17} \text{ S m}^{-1} \text{ s}^{-1}$ for the 130 nm sample and $A_{1,2} = (2.5, 6.0) \times 10^{17} \text{ S m}^{-1} \text{ s}^{-1}$ for the 470 nm sample. The Drude term was constrained by fitting the amplitude of the transmission (the square root of the power transmission) obtained from FTIR spectroscopy, shown in figure 5(c). By re-arranging equation (1) one can write,

$$|T(\omega)| = |1 + n_s|/|1 + n_s + \sigma(\omega)Z_0\delta|, \quad (3)$$

and use $\sigma(\omega)$ from equation (2) to create a modeled $|T(\omega)|$. An iterative fit to the experimental $|T(\omega)|$ from THz-TDS and FTIR yielded $\sigma_D = 1589 \pm 10 \text{ S cm}^{-1}$ for the 470 nm film, with the same $\tau_D = 18 \pm 1 \text{ fs}$ assumed for both. The blue shaded areas in figures 5(a) and (b) indicate the Drude contribution to σ_1 , which makes up a substantial fraction of the overall THz conductivity.

The resonance frequency of the weaker plasmon contribution to the optical conductivity indicates that plasmons oscillate over a length scale of between 220 and 450 nm. As the average tube length is $2\ \mu\text{m}$, this shorter length scale over which plasmons oscillate may indicate the typical distances between defects, or the average distance between tube–tube contacts (estimated at $0.6\ \mu\text{m}$). The scattering time for these electrons is long (~ 300 fs) in comparison to that for electrons undergoing inter-tube transport (~ 18 fs). The scattering time τ is a measure of how quickly the direction of the momentum is randomized: the shorter scattering time for percolative electrons arises from electrons changing direction more substantially at junctions than along the CNT.

Knowledge of the scattering time permits the effective mobility, μ , and carrier density, n , of the composite to be calculated from $\mu = e\tau/m^*$ and $\sigma_D = ne^2\tau/m^*$, given the experimental τ and σ_D . A very rough estimate for m^* in our DWNTs can be obtained by considering m^* for SWNTs, which crucially depends on the CNT diameter d [32–34]. The outer shell diameters ranged from 2–3 nm in the present case. For $d = 3.0$ nm, $m^* = 0.026 m_e$, increasing to $m^* = 0.038 m_e$ for $d = 2.0$ nm [32]. To facilitate a comparison with uniform conductive films we calculated the effective mobility and effective carrier density of our composite using $\mu = e\tau/m^*$ and $\sigma_D = ne^2\tau/m^*$, assuming that $m^* = 0.03 m_e$. Taking the Drude lifetime $\tau = 18$ fs for long-range charge transport yields $\mu = 1054\ \text{cm}^2\ \text{V s}^{-1}$. For the 130 nm film, with $\sigma_D = 2335\ \text{S cm}^{-1}$, the carrier density is $n = 1.4 \times 10^{19}\ \text{cm}^{-3}$. However we emphasize that there is a large uncertainty in the effective mass that may change these numbers significantly. In addition to the variation with CNT diameter, the mass for SWNTs also varies substantially with chemical potential as the bands are highly nonparabolic [32], and this discussion further ignores complications like tube–tube interactions and a finite CNT curvature. Further, a strong THz electromagnetic response may be expected from a metallic inner shell if the outer shell is semiconducting.

Finally, we examine the low temperature DC-transport measurements, for which the intertube transport has decisive importance. In the macroscopic thin films, electrically connected paths percolate through the material. One can assume those paths that are dominated by semiconducting tubes to turn non-conducting at low temperature. The thin films exhibited no gate effect, even at low temperatures. Upon reducing the thickness, down to ~ 10 nm, the level of conductivity drops by an order of magnitude from the bulk values. This is normal in most types of thin films as a consequence of increased disorder. At low temperatures the inter-tube resistance leads to thermally activated hopping/tunneling processes that govern the overall DC charge transport. The inset in figure 2(a) presents the conductivity down to 1.3 K at a log–log scale for one representative thin film sample. From the conductivity data, we can judge that as $T \rightarrow 0$ K, the temperature dependence is weakly activated and the samples are close to the metal-insulator transition

boundary [35]. We estimate that the activation energy is in the meV-range. We may thus assume that the intertube connections have relatively low resistance, but they dominate over the scattering within the tubes. It follows from the activated nature of the DC-conductivity that the conductivity decreases at the lowest temperatures, which is more or less always seen in all CNT-materials. This brief analysis of the low temperature DC-transport properties is consistent with that stemming from the KPFM- and the optical conductivity measurements.

As one example of the potential of these materials in applications, we demonstrate the efficiency of these CNT-hcs as broadband absorptive filters, by calculating the attenuation of the films on which we measured the optical conductivity. This was relatively frequency independent (as the transmission is relatively flat) up to 2.5 THz. The attenuation increases with film thickness to around ~ 30 dB for the 1170 nm-thick film, suggesting that CNT-hcs are effective for electromagnetic shielding applications at least up to 2.5 THz, and with enhanced shielding for thicker films. The benefit of CNT-hc compared to CNTs is an easier dispersal, and the fabrication of stable and uniform films without decreasing the electrical conductivity relative to pure CNTs. Indeed, the exceptional conductive performance of the CNT-hc films persists from DC all the way up to terahertz frequencies. Recent studies on bundles of SWNTs using THz spectroscopy reported similarly high conductivities for thin films, as long as the nanotubes are sufficiently long and densely packed [36–38].

5. Conclusions

The CNT-hc complex has the advantage of relatively easy dispersal in water, which enables the fabrication of stable and uniform films in an environmentally friendly way, and with an electrical conductivity comparable to pure CNT material. In low temperature DC measurements, a relatively weakly increasing resistivity of the CNT-hc is seen, showing that the material is close to the metal-insulator transition. High frequency measurements reveal a weak maximum in conductivity at THz frequencies, which is consistent with plasmon resonances in individual CNTs combined with DC-conductivity across intertube connections.

The high conductivity can be understood as a combination of several factors:

- (i) The excellent conductive properties of 1D charges moving along the CNTs.
- (ii) The contribution of metallic CNTs, which constitute a substantial share as the CNTs were not sorted by their chirality.
- (iii) A low contact resistance between CNTs in the present case, as proven microscopically with KPFM in this manuscript. Essentially the hc (xylan), which wraps the nanotubes and makes it easy to disperse them in water, does not act as an electrical barrier to conduction.

Acknowledgments

We thank for valuable discussions Dr. Oren Regev, Ben-Gurion University of the Negev, Israel. This work was funded by the Academy of Finland (Grant No. 263523). P Y acknowledges the support from the Thai Ministry of Education, the Office of Higher Education Commission, project CHE-PhD-SFR 2007.

ORCID iDs

Markus Ahlskog  <https://orcid.org/0000-0003-3479-2619>

James Lloyd-Hughes  <https://orcid.org/0000-0002-9680-0138>

References

- [1] Yoon S H, Jin H J, Kook M C and Pyun Y R 2006 *Biomacromolecules* **7** 1280–4
- [2] Jung R, Kim H S, Kim Y, Kwon S M, Lee H S and Jin H J 2008 *J. Polym. Sci. B* **46** 1235–42
- [3] Yun S, Jang S D, Yun G Y, Kim J H and Kim J 2009 *Appl. Phys. Lett.* **95** 104102
- [4] Tanaka T, Sano E, Imai M and Akiyama K 2010 *J. Appl. Phys.* **107** 054307
- [5] Lu J, Zhang H, Jian Y, Shao H and Hu X 2012 *J. Appl. Polym. Sci.* **123** 956–61
- [6] Yun S and Kim J 2011 *Carbon* **49** 518–27
- [7] Lee T W and Jeong Y G 2015 *Carbohydrate Polym.* **133** 456–63
- [8] Minami N, Kim Y, Miyashita K, Kazaoui S and Nalini B 2006 *Appl. Phys. Lett.* **88** 093123
- [9] Yang Q, Shuai L, Zhou J, Lu F and Pan X 2008 *J. Phys. Chem. B* **112** 12934–9
- [10] Olivier C, Moreau C, Bertoncini P, Bizot H, Chauvet O and Cathala B 2012 *Langmuir* **28** 12463–71
- [11] Hamed M M, Hajian A, Fall A B, Hakansson K, Salajkova M, Lundell F, Wagberg L and Berglund L A 2014 *ACS Nano* **8** 2467–76
- [12] Hajian A, Lindstrom S B, Pettersson T, Hamed M M and Wagberg L 2017 *Nano Lett.* **17** 1439–47
- [13] Islam M F, Rojas E, Bergey D M, Johnson A T and Yodh A G 2003 *Nano Lett.* **3** 269–73
- [14] Fernandes R M F, Buzaglo M, Shtein M, Pri Bar I, Regev O, Marques E F and Furo I 2014 *J. Phys. Chem. C* **118** 582–9
- [15] Sun D M, Liu C, Ren W C and Cheng H M 2013 *Small* **9** 1188–205
- [16] Kaiser A, Skakalova V and Roth S 2008 *Physica E* **40** 2311–8
- [17] Lekawa-Raus A, Walczak K, Kozlowski G, Wozniak M, Hopkins S C and Koziol K K 2015 *Carbon* **84** 118–23
- [18] Skakalova V, Kaiser A B, Woo Y S and Roth S 2006 *Phys. Rev. B* **74** 085403
- [19] Nirmalraj P N, Lyons P E, De S, Coleman J N and Boland J J 2009 *Nano Lett.* **9** 3890–5
- [20] Vavro J, Kikkawa J M and Fischer J E 2005 *Phys. Rev. B* **71** 155410
- [21] Behnam A, Biswas A, Bosman G and Ural A 2010 *Phys. Rev. B* **81** 125407
- [22] Zhang Q, Hároz E H, Jin Z, Ren L, Wang X, Arvidson R S, Lüttge A and Kono J 2013 *Nano Lett.* **13** 5991–6
- [23] Jorma Virtanen V K 2017 Highly conducting material *US Patent Specification* 20160141483
- [24] Dai J, Zhang J, Zhang W and Grischkowsky D 2004 *J. Opt. Soc. Am. B* **21** 1379–86
- [25] Melitz W, Shen J, Kummel A C and Lee S 2011 *Surf. Sci. Rep.* **66** 1–27
- [26] Wang Y and Chen X 2007 *Ultramicroscopy* **107** 293–8
- [27] Lloyd-Hughes J and Jeon T I 2012 *J. Infrared Millim. Terahertz Waves* **33** 871–925
- [28] Behabtu N et al 2013 *Science* **339** 182–6
- [29] Kim J, Hong D, Lee H, Shin Y, Park S, Khang Y, Lee M and Hong S 2013 *J. Phys. Chem. C* **117** 19721–8
- [30] Morimoto T, Joung S K, Saito T, Futaba D N, Hata K and Okazaki T 2014 *ACS Nano* **8** 9897–904
- [31] Nakanishi T and Ando T 2009 *J. Phys. Soc. Japan* **78** 114708
- [32] Marulanda J M and Srivastava A 2008 *Phys. Status Solidi b* **245** 2558–62
- [33] Akinwande D, Nishi Y and Wong H S P 2007 Analytical model of carbon nanotube electrostatics: density of states, effective mass, carrier density and quantum capacitance *IEEE International Electron Devices Meeting* pp 753–6
- [34] Zhou X, Park J Y, Huang S, Liu J and McEuen P L 2005 *Phys. Rev. Lett.* **95** 146805
- [35] Jaiswal M and Menon R 2006 *Polym. Int.* **55** 1371–84
- [36] Zhukova E S et al 2017 *Nanotechnology* **28** 445204
- [37] Gorshunov B et al 2018 *Carbon* **126** 544–51
- [38] Karlsen P et al 2018 *J. Phys. D: Appl. Phys.* **51** 014003

Surface characteristics control the attachment and functionality of (chimeric)avidin (Langmuir)

A.II

1 Surface Characteristics Control the Attachment and Functionality of 2 (Chimeric) Avidin

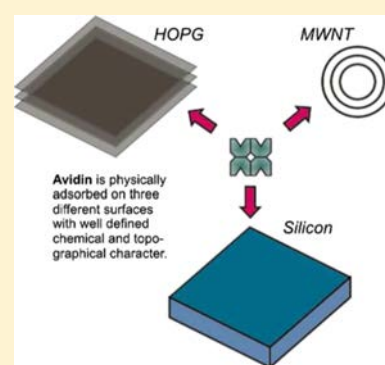
3 Dongkai Shao,[†] Kosti Tapio,[†] Sanna Auer,[‡] J. Jussi Toppari,[†] Vesa P. Hytönen,[‡]
4 and Markus Ahlskog^{*,†}

5 [†]Nanoscience Center, Department of Physics, University of Jyväskylä, Jyväskylä FI-40014, Finland

6 [‡]Faculty of Medicine and Life Sciences and BioMediTech, Fimlab Laboratories, University of Tampere, Tampere FI-33520, Finland

7 **S** Supporting Information

8 **ABSTRACT:** The physical adsorption (physisorption) of proteins to surfaces is an
9 important but incompletely understood factor in many biological processes and is of
10 increasing significance in bionanotechnology as well. Avidin is an important protein
11 because of strong avidin–biotin binding, which has been exploited in numerous
12 applications. We have undertaken thorough experimentation on the physisorption of
13 avidin, to chemically different flat surfaces of Si and graphite and also to the curved
14 version of the latter, on multiwalled carbon nanotubes (MWNTs) of different
15 diameters. The difference in the behavior of avidin on Si versus graphite is drastic; on
16 Si, avidin deposits as single globular tetrameric units and maintains functionality,
17 whereas on graphite, it forms irregular networks of two-layer thick filaments, where the
18 first layer has lost its biological activity. On MWNTs, avidin also deposits as one-
19 dimensional formations, or stripes, but these appear to order in a perpendicular
20 arrangement to the MWNT axis. A better understanding of protein–surface
21 interactions is essential for the development of robust and reliable methods for
22 biofunctionalization of materials. This work also provides insights into the importance of the nanoscale surface architecture.



23 ■ INTRODUCTION

24 Physical adsorption (physisorption) of proteins on solid
25 surfaces is important in many biological processes. In bio-
26 and nanotechnology, the phenomenon is of interest for
27 biointerfaces, although the purpose is often to avoid physical
28 adsorption of proteins to certain surfaces. On the other hand,
29 in applications where a protein monolayer is needed, it is more
30 common to resort to covalent linking, that is, chemical
31 adsorption, of the protein to the surface. Covalent linking can
32 ensure the desired orientation of the protein and thus preserve
33 its functionality. However, the prevalence of chemical
34 adsorption is one motivation for also studying physisorption
35 of proteins, as the two can be difficult to separate from each
36 other with absolute certainty.¹

37 The complexity of proteins ensures that even though
38 physisorption is simple to execute, it is difficult to investigate
39 in a detailed level.^{2–4}

40 Especially, the older experimental work on protein adhesion
41 phenomena has been undertaken with techniques, such as
42 ellipsometry and the quartz crystal microbalance, which at best
43 can sense the formation of a monolayer but do not reach the
44 single-molecule level.⁵ The individual protein may severely
45 change its conformational state upon interaction with the
46 surface, and if the surface mobility is high, there is the
47 possibility of complex pattern formation, which requires high-
48 resolution imaging data in order to be investigated and
49 understood.

50 There are a number of both theoretical and experimental
51 atomic force microscopy (AFM) studies of individual protein
52 deposition on surfaces such as Si^{6,7} and graphite and
53 graphene.^{8–12} Yet, because of the complexity of the problem,
54 many important aspects remain open issues.

55 Conventionally, in both applications and experimentation,
56 one has used substrates whose surfaces are flat both on
57 macroscopic and microscopic scales, such as silicon, certain
58 oxides, mica, graphite, and so forth. For such surfaces,
59 parameters that are of prime importance are surface energy,
60 polarity, and charge. In addition to these, surface topography
61 has rarely been a parameter in experiments, as in reality, it is
62 difficult to have it under control at the nanometer scales that
63 are most relevant for proteins. This does not mean that surface
64 topography could not sometimes be a major factor. However,
65 AFM allows the surface topography to be conveniently
66 measured on those scales. Moreover, carbon nanotubes offer
67 a practically realizable surface with a clean and well-defined
68 curvature on that scale. Arc-discharge synthesized multiwalled
69 carbon nanotubes (MWNTs) were the first type of carbon
70 nanotubes discovered,¹³ but are nowadays at the fringe of
71 interest because of the abundance of carbon impurities and the
72 unscalability of the synthesis method. Yet, they are of a high

Received: August 27, 2018

Revised: October 19, 2018

Published: November 6, 2018

73 quality and can provide a nearly perfect curved graphitic
74 surface in a tube diameter range at least up to 20 nm.¹⁴

75 In this work, we have studied experimentally the physical
76 adsorption of tetrameric avidin to different surfaces, a protein
77 which is important both in current technology and in
78 bionanotechnological research.

79 Avidins are well-known because of the superior strength of
80 the noncovalent binding between avidin and biotin molecules,
81 which is utilized in numerous applications such as for labeling,
82 biofunctionalization, targeting, and delivery.¹⁵ The majority of
83 avidins are tetrameric proteins, and their functionality is lost if
84 the tetramer is dissociated. In the applications and numerous
85 research works where avidin or streptavidin has been used,
86 usually, it has been covalently linked to a surface or to a
87 nanoparticle. Therefore, despite being a commonly used
88 protein, there is not much in the research literature on the
89 physical adsorption properties of avidin.

90 The main elements of the experiments of this work are
91 summed up in Figure 1. We use silicon (Si) and highly

patterns of avidin depending on the surface characteristics. For 96
applications, the important aspects are stability and function- 97
ality of the adsorbed protein molecule. The functionality of 98
avidin–biotin binding in the monolayer scale avidin deposits 99
was tested with biotinylated gold nanoparticles (b-AuNPs) and 100
was found to work well under specific conditions. 101

■ EXPERIMENTAL SECTION 102

Materials. Chimeric avidin has been obtained as a hybrid of 103
chicken avidin and avidin-related protein 4 and produced in 104
Escherichia coli using the method described earlier.¹⁶ Chimeric avidin 105
consists of four identical subunits with a molecular weight of 52.6 kDa 106
per tetramer. It has extremely high thermal stability (melting 107
temperature 111.1 °C). Two independent batches of chimeric avidin 108
were used in the following experiments with very similar results. For 109
the preparation of samples, phosphate-buffered saline (PBS) buffer 110
was used for all experiments involving avidin and b-AuNPs. The 111
composition of PBS buffer used is 0.8 g/L of NaCl, 0.2 g/L of KCl, 112
1.4 g/L of Na₂HPO₄·2H₂O, and 0.2 g/L of KH₂PO₄. Deionized water 113
was prepared with a Milli-Q ultrapure water system. b-AuNPs of 5 nm 114
diameter (Figure 1) were purchased from Cytodiagnosics.^a On 115
average, there are around 40 biotin groups on each AuNP based on 116
the surface area and biotin group density. 117

Sample Preparation. Precut 8 mm × 8 mm pieces of silicon 118
wafer were cleaned from small particles by blowing with a carbon 119
dioxide gas gun and then washing with acetone and isopropyl alcohol. 120
The Si pieces were rendered hydrophilic or hydrophobic with reactive 121
ion etching (RIE-Plus Oxford Instruments). The etching was done for 122
2 min at 30 °C and 300 W forward power. The flow parameters were 123
50 sccm O₂ for hydrophilic treatment and 50 sccm CHF₃ and 5 sccm 124
O₂ for hydrophobic treatment. The hydrophilic treatment results, 125
predominantly, in a thin layer of –OH groups on the silicon surface, 126
similar to the conventional piranha treatment. The hydrophobic 127
treatment removes the native silicon oxide on top of the silicon 128
surface, which will leave pure silicon surface, which is hydrophobic. 129
The surface of course immediately begins to reoxidize, but for the 130
time required to perform the experiments, usually within an hour, the 131
hydrophobic character will dominate. HOPG was purchased from 132
Goodfellow Ltd. Fresh HOPG surfaces were used for the experiments 133
and were obtained by simple cleaving of the piece of HOPG. The 134
contact angle of a water droplet on both HOPG and hydrophobic 135
silicon is in c. 85°. 136

An arc-discharge synthesized MWNT material was used, which 137
contains high-quality MWNTs, but also much graphitic carbon debris. 138
The MWNTs were randomly distributed on Si/SiO₂ chips, with 139
microolithographically fabricated 200 nm wide trenches, so that we 140
could find tubes both on the solid surface and crossing the trenches. 141
The diameter distribution of MWNTs was 2–20 nm, which means 142
that usually a tube crossing a trench was mechanically rigid enough to 143
be almost straight on the suspended part and to be able to stay so 144
during imaging with AFM. Further details are given in the Supporting 145
Information. 146

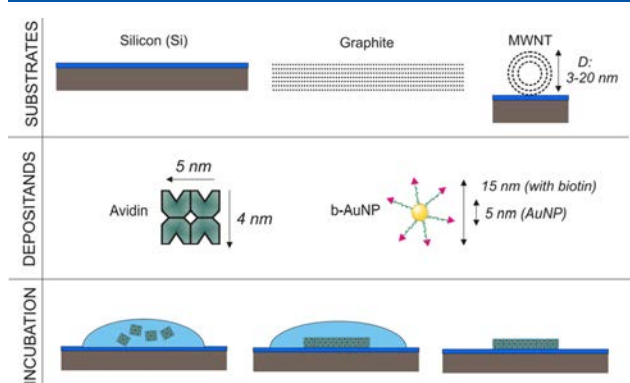


Figure 1. Essential elements of the experiments. First row: the substrates used for physical protein adsorption. Second row: the protein we study is avidin, which is a homotetrameric protein. b-AuNPs are used to test the functionality of avidin with respect to its ability to bind biotin. Third row: scheme for the simplest incubation technique of avidin on a surface, which is some of three mentioned above. A droplet of a solution of avidin is placed on a substrate, and allowed to stand there for a predetermined time. Physisorption of avidins takes place during this time, after which the droplet is blown away.

92 oriented pyrolytic graphite (HOPG) as smooth chemically
93 different surfaces. A third substrate is the MWNT, which
94 realizes testing of the effect of curvature on HOPG. We found
95 fundamental and well-defined differences in the adsorption

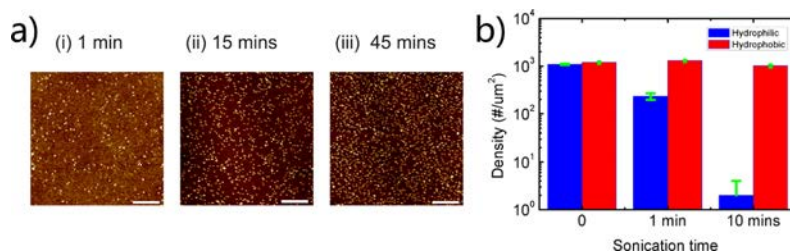


Figure 2. Deposition of avidin on silicon. (a) AFM images of avidin on hydrophobic surfaces, after incubation from 0.1 μM solution. The incubation times are indicated above the figures. Scale bar 200 nm. (b) To evaluate the attachment strength, the density of avidin (nr. per square micrometer) is displayed as a function of both sonication time, on hydrophobic and hydrophilic surfaces that initially had a high concentration. The density was calculated on three different sites of the sample. The error bars indicate the deviations.

147 Physical adsorption of avidin was done by incubation (Figure 1).
148 After appropriate conditioning of the substrate, a small droplet
149 (usually 50 μL) of avidin solution was placed on it. The washing steps
150 included three dd- H_2O immersions (1 min each) and blowing of air
151 using a 1000 μL pipette three times. The sample was then dried with a
152 nitrogen gas gun.

153 All the important results of this work are based on repeated
154 experimentation. The presented sets of data of deposition on silicon
155 and graphite are the results of multiple tests where we have tried out
156 different concentrations, incubation times, and some other deposition
157 parameters that are optimal for revealing the fundamental effects. The
158 same applies for the work on MWNTs, but here, there are more
159 practical difficulties, as the MWNTs exist in a distribution of
160 diameters, that appear randomly in the deposited MWNT material.
161 Therefore, each MWNT sample is, strictly speaking, unique. We have
162 prepared a total of c. 50 individual MWNTs for the experiments
163 described here, which was sufficient for us to obtain several samples
164 around each diameter in the range of 2–20 nm. Another essential
165 aspect is that arc-discharge grown MWNTs are of superior quality
166 compared to ordinary chemical vapor deposition grown MWNTs.¹⁷

167 ■ RESULTS AND DISCUSSION

168 Figure 2a shows the AFM images of the result of physical
169 adsorption of avidin on the Si surface. The main observation is
170 that avidin deposits as randomly placed globular clusters,
171 presumably single tetramers on the silicon surface. As
172 expected, the density of avidins on the surface increases with
173 increasing solution concentration and incubation time. A close-
174 up image of high density of avidin is shown in Figure 3. The

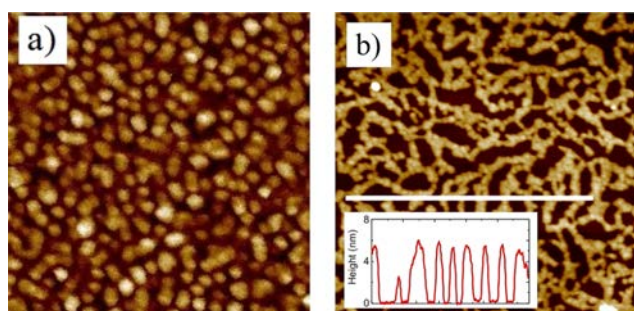


Figure 3. Dense avidin deposition on (a) Si (size 200 nm) and (b) graphite (size 1 μm). Inset: AFM height data along the line on the graphite figure.

175 hydrophilicity of silicon surface has little effect on the final
176 deposition density of avidin. The highest density we found is
177 around 6500 units per square micrometer at pH = 7 buffer.

178 The height of avidin on a silicon surface is around 2.5–3
179 nm, both on hydrophilic and hydrophobic surfaces. This is
180 about half of the tetramer size of avidin in solution, as
181 determined by X-ray diffraction.¹⁸ It is rather obvious that
182 crystallography supports a highly extended shape of the
183 protein, which partially collapses on a surface, even if we
184 preserve the major characteristics of the protein. We may thus
185 claim that 2.5–3 nm is in fair agreement with the size of the
186 functional core of the tetrameric protein (after drying the
187 sample).

188 We found that the hydrophilicity of the Si surface affects the
189 affinity of adsorbed avidin. This was tested with simple bath
190 sonication. The graph of Figure 2b shows that the density of
191 avidin on a hydrophobic surface nearly keeps constant for 10
192 min of sonication time, whereas on a hydrophilic surface, it
193 drops very strongly, indicating loose attachment. Moreover, we

used AFM imaging with the PeakForce mode (Bruker Icon) to
adjust the peak force setpoint, the maximum force with which
the oscillating tip is interacting with the surface. We found that
we could move avidin on a hydrophobic surface with 30 nN as
the peak force setpoint, whereas on a hydrophilic surface, 14
nN was sufficient, again indicating that avidin binding is tighter
in the former case.

Figure 4 shows avidin on HOPG after incubation from 1 μM
solution, in samples with different incubation times and with
AFM profile height data. It is evident that, unlike on the Si
surface, avidin has a strong tendency upon physical adsorption
to aggregate into patterns on HOPG surfaces. After the
shortest 30 s incubation, shown in the first image (i), avidins
have formed separated irregular or slightly chain-like clusters.
Some of these clusters appear to form linear assemblies, which
most likely correspond to the omnipresent single-layer fault
lines of a HOPG surface. The same phenomenon has been
observed with other proteins.¹⁹ A closer image of a typical
avidin cluster is shown in the inset of Figure 4(i). The height
of these irregular clusters is around 1.5–2 nm, which is lower
than the individual avidin height on Si.

Figure 4(ii) shows the avidin patterns after a longer, 1 min
incubation. There is a crucial difference to the previous figure:
the pattern is essentially similar, but from the AFM height data,
we can see that besides the 2 nm height, a second height level
of around 4 nm appears. Our interpretation is that a second
layer of avidin starts to form on top of the first deposited
(mono-)layer, already slightly chain-like in appearance. In this
case, the second, which we call a double layer, has not fully
covered the first monolayer. In the third, 15 min incubation, all
avidin structures are now around 4–5 nm in height,
corresponding to the double-layer type of deposition.

Figure 3b shows how the avidin pattern on HOPG develops
after a further increase of the incubation time. The chain
structures, still having the same 4–5 nm height, get connected
to form an irregular network. The size of the empty regions is
in the 10–100 nm range. The width of the chain structures
does initially correspond to what is expected from images with
tip-convolution widening of a single avidin tetramer unit. The
avidin deposits widen further upon increasing the time, an
example of which is shown in Figure 7c.

Next, we move to arc-discharge MWNTs, which give us the
opportunity to study deposition on curved graphite. Although
the material contains amorphous carbon debris, the tubes
themselves are of high quality, and by searching, one can find
in selected locations MWNTs with few impurities within a
micron scale area. Figure 5a shows an MWNT of diameter 10
nm before deposition. The AFM images reveal a smooth tube
surface mostly absent of impurity particles or other
deficiencies. More details are presented in the Supporting
Information.

Figure 6 shows two suspended MWNTs of diameter 16 and
17 nm, after avidin deposition. A most interesting result is the
character of avidin depositions, observed in these larger
diameter MWNTs. The deposits have the form of stripes that
are roughly perpendicular to the tube axis. Besides occasional
differences, we did not observe any clear-cut evidence for
different depositions of avidin on a suspended section
compared to the nonsuspended parts. We conclude that
possible effects of the suspension are masked by complicated
local effects beyond our control.

Figure 5b,c shows tubes of smaller diameter, where the
deposits are still present but their stripe-like character, as

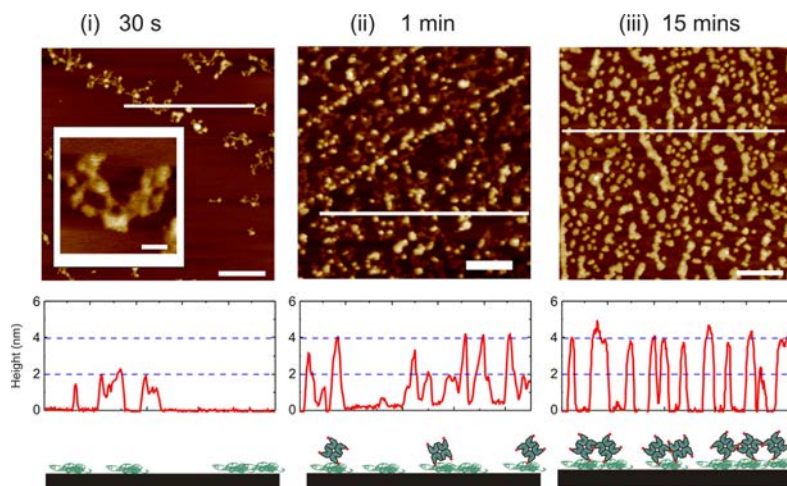


Figure 4. Avidin deposition on HOPG. The uppermost AFM images show the deposited avidin, after incubation in $1 \mu\text{M}$ solution for three different times. These times are indicated above the figures. Scale bars are 100 nm. (i) Closer image as the inset, with a scale bar of 20 nm. Below the AFM images are the extracted topographical height data (along the lines). Lowest is the schematic illustration of the suggested model for pattern formation by the avidins.

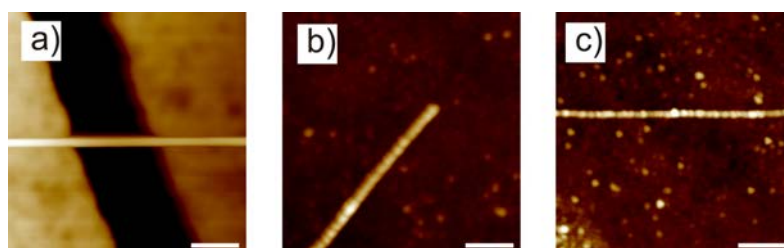


Figure 5. AFM images of the experiments with avidin deposition on MWNTs. (a) Suspended, intermediate-sized MWNT ($D = 10 \text{ nm}$) before deposition. The tube is perfectly clean, within the resolution limit of AFM. (b) Avidin on MWNT with $D = 5 \text{ nm}$. (c) Avidin on MWNT with $D = 3 \text{ nm}$. In these smaller tubes, the MWNT diameter is close to the size of globular, folded avidin.

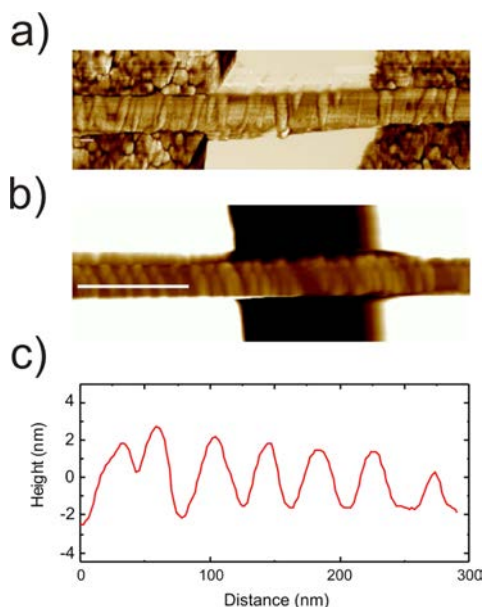


Figure 6. AFM images of avidin deposition on larger MWNTs. (a) Suspended MWNT with $D = 16 \text{ nm}$ and (b) suspended MWNT with $D = 17 \text{ nm}$. The avidin is seen as stripes perpendicular to the tube axis. (c) Height profile along the line in (b).

up into chains across the smallest tubes, it is, to a large extent, 259 understandable as a technical imaging issue. The tip radius is 260 typically around 10 nm and the tip apex is of course not truly 261 spherical and is therefore unable to discern the real geometry 262 of avidin deposition around the curvature of smaller diameter 263 tubes. The height is measured as 2–5 nm, and we did not find 264 a visible transition from single-layer to double-layer structures. 265 Despite this inaccuracy, it is clear that the height corresponds 266 to that on graphite. The separation between the stripes varies 267 but is in the range 20–40 nm. Figure 6b demonstrates that the 268 deposits can sometimes be very regularly spaced. 269

The last results of this work are the tests on the functionality 270 of avidin deposits and on the ability of the surface-bound 271 avidins to bind the b-AuNPs via the biotin coupling. Deposits 272 of avidin on Si and HOPG were separately incubated with a 273 solution of b-AuNP. In the case of avidin on Si, we present in 274 the supplement the data images of incubation with b-AuNPs 275 on avidin deposition. In this case, it was not easy to 276 discriminate unambiguously between avidins complexed with 277 b-AuNP and very possible sole b-AuNPs on the surface. 278 However, the data implies that, on (hydrophobic) silicon, 279 avidin has an affinity for b-AuNPs. The affinity is clearly 280 greater than that of b-AuNP to bare silicon. 281

On HOPG, the results were less ambiguous and more 282 interesting. We demonstrate that the distinctly different mono- 283 and double-layer formations of avidin (Figure 4) have 284 dramatically different affinities to b-AuNPs. We made b- 285 AuNP incubation tests on these two formations, and 286

257 observed with AFM, gradually vanishes. Besides the self- 258 evident fact that there is no space for multiple proteins to link

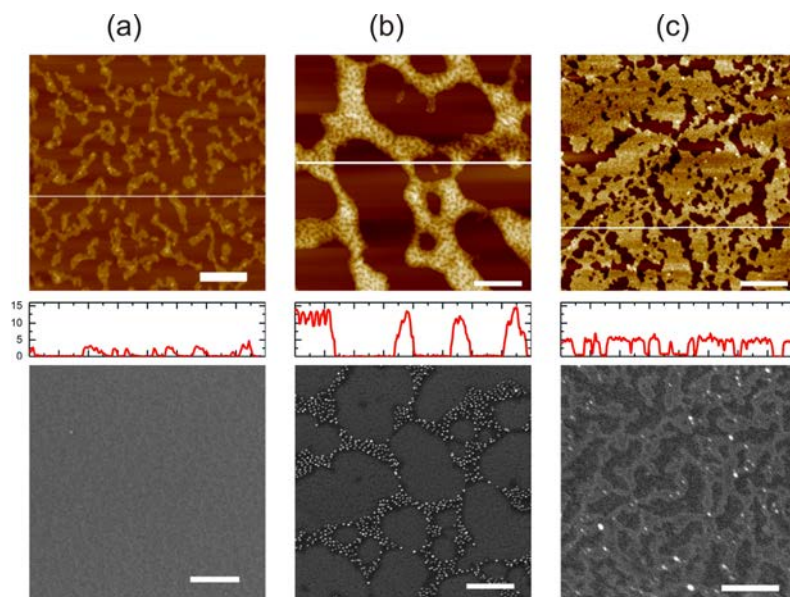


Figure 7. Testing functionality of three different avidin layers on HOPG by incubation with b-AuNPs and subsequent imaging. For each case, on top is an AFM image and below it is the height profile. Lowest is a SEM image. (a) Avidin monolayer; (b) avidin double layer; and (c) d-biotin-blocked double layer. Scale bar 200 nm.

287 additionally on a third one, which was a double layer made
 288 from biotin-blocked avidin. This third type is for control
 289 purpose only, as such avidin cannot link to b-AuNPs. The
 290 results of incubation tests on these three systems are presented
 291 with AFM and scanning electron microscopy (SEM) images in
 292 **Figure 7**, where each column of images corresponds to one of
 293 the above-mentioned systems.

294 The first and second columns of **Figure 7** show results of
 295 deposition of b-AuNP on the mono- and double layers,
 296 respectively. In a single column, above is an AFM image with a
 297 height data profile and below these is an SEM image. It is
 298 strikingly clear that on the presumed unfolded/denatured
 299 single-layer chain structure (first column), there is little affinity
 300 to b-AuNPs, as especially the SEM images reveal (**Figure 7a**)
 301 the absence of any gold particles. As opposed to this, the
 302 double-layer structure (second column) efficiently attracts b-
 303 AuNPs. The third column contains images of a double layer
 304 made from biotin-blocked avidin (**Figure 7c**). The affinity for
 305 b-AuNP is negligible, which then confirms avidin–biotin
 306 linking as the mechanism behind affinity to the double layer.

307 We have shown that avidin deposits in very specific and
 308 different ways depending on the characteristic surface. On
 309 silicon, avidin deposits as isolated globular clusters, and this
 310 individual character remains discernible even at the highest
 311 densities of the deposits (**Figure 3**). The behavior is in two
 312 ways starkly different on graphite. First, no globules were seen.
 313 The first single proteins, imaged after the shortest incubation
 314 times (**Figure 4(i)**), show a tendency to spread along the
 315 graphite surface. Second, after a little longer incubation, the
 316 avidin forms irregular chain structures. On the MWNTs,
 317 similar one-dimensional (1D)-like chain formations are found
 318 as on graphite, which are called “stripes”, and are organized
 319 roughly perpendicular to the tube axis. We must relate these
 320 data to general results on protein physisorption, as most of the
 321 molecular dynamics simulations on avidin have focused on its
 322 interaction with biotin^{20–22} and have ignored issues related to
 323 bulk surfaces.

The individual globular clusters on Si are interpreted as
 324 single avidin tetramers. The measured height, ~ 2.5 nm, is
 325 clearly lower than what would be implied from the solution-
 326 phase crystallographic data ($5 \text{ nm} \times 5 \text{ nm} \times 4 \text{ nm}$), which is
 327 expected because of the immersed water and fully extended
 328 protein conformation in the latter. Otherwise, there is no
 329 indication in the AFM data on the decomposition of avidins on
 330 a silicon surface. Moreover, the height is independent of its
 331 hydrophilic/hydrophobic state, whereas hydrophilicity seems
 332 to matter with respect to the affinity of avidin to the silicon
 333 surface, a result in agreement with the well-documented
 334 adherence of proteins to hydrophobic surfaces.² 335

For graphite, concerning the individual behavior, both
 336 experimental and theoretical work are in line with our results.
 337 In ref 23, simulation revealed that avidin and graphene can
 338 form stable complexes primarily via hydrophobic forces and
 339 suggested conformational rearrangement near the surface.
 340 However, this work uses only one monomer of avidin, while
 341 we have utilized the biologically more relevant tetrameric form.
 342 The recent work of Barinov et al.²⁴ obtained quite solid results
 343 by investigating three different proteins on fresh and
 344 hydrophilically modified graphite. The results confirm that
 345 proteins commonly tend to collapse/denature on a plain
 346 graphite surface, which is what we described as spreading in
 347 the AFM data. The work also makes the case that confusing
 348 results are easily obtained if the graphite surface has significant
 349 contamination. Thus, the spreading of avidin on graphite that
 350 we observed in the very first deposits (**Figure 4(i)**) is
 351 supported by other works. 352

The other big difference between Si and graphite is that on
 353 the former, the avidin deposits solely as single globular
 354 proteins, while agglomeration dominates in graphite. The
 355 competition between these two mechanisms is a familiar issue
 356 in studies on physical adsorption of proteins.^{3,4} Single-protein
 357 deposition has been quantitatively explained by Langmuir
 358 adsorption and/or randomized sequential adsorption theories,
 359 which depict the adsorption process to consist of individual
 360 proteins that stochastically land on empty slots on the surface. 361

362 An essential feature is that the protein molecules normally are
363 charged and thus repel each other at close distances, leading to
364 different maximum packing densities. In this work, the avidin
365 monolayer has, at saturation coverage, a density of around
366 6000 per micrometer squared (500 Ru). This is about 20% of
367 the highest reported chemical adsorption density of avidin on
368 biotin-functionalized surfaces (2800 Ru).²⁵ A possible
369 explanation could be that avidin in PBS bears a net positive
370 surface charge ($pI = 9.5 > pH = 7$ buffer), causing interprotein
371 repulsion.

372 The very different avidin patterns on graphite result from an
373 agglomeration process. Similar AFM studies have been
374 reported previously with ezrin²⁶ and fibrinogen.²⁷ Fibrinogen
375 is present in blood and plays a key role in the coagulation
376 process, whereby physical adhesion is of special relevance. It
377 was shown²⁷ that fibrinogen can deposit (on polyethylene
378 crystals) as individual proteins or as 1D, single-molecule thick
379 chains, depending on solution parameters such as pH value. It
380 was argued that the interplay between protein–protein
381 interaction, surface diffusion, and surface–protein interaction
382 determines whether aggregation occurs, and the weight of
383 different factors can be tuned. Thus, the tendency of proteins
384 to form monolayered chain structures under specific
385 conditions, the same as in our case with avidin on graphite,
386 has been well demonstrated, although a solid theoretical
387 understanding is still lacking. The exact mechanism of how the
388 bilayered chain structures (Figure 4(ii)) of avidin on graphite
389 are formed is not clear. Our observations point to a two-
390 stepped formation process, where the deposition of the first
391 layer is strongly accompanied by denaturation and protein
392 unfolding and this layer having a small height. Seemingly, this
393 first layer is strongly adhering to the next avidin still in the
394 solution phase, leading to the formation of the bilayer structure
395 (Figure 4a).

396 On the MWNTs, the organized structure of avidin stripe
397 deposition could be concluded from those tubes that were
398 large enough, that is, had a radius not smaller than the tip
399 radius. The image data from smaller tubes did not allow the
400 same resolution but apart from that is not in contradiction with
401 the data from the larger tubes. The distance between the
402 stripes is typically 20–40 nm and could be very regular (Figure
403 6b), which hints at a mechanism with a repulsive force
404 between the avidin stripes, as they deposit on the MWNT.

405 In a few previous works,^{28–30} carbon nanotubes and
406 different proteins have been mixed together to enable the
407 water solubility of the tubes. These works have demonstrated
408 the affinity of carbon nanotubes toward proteins. However,
409 most of them use only single-walled nanotubes (SWNTs), with
410 diameter 1–2 nm. More or less casual AFM imaging of
411 protein-functionalized carbon nanotubes has been reported,
412 but to our knowledge, there is no previous AFM imaging data
413 that reveal the actual organization patterns of proteins on
414 nanotubes. There are at least two reports of transmission
415 electron microscopy (TEM) high-resolution imaging of
416 proteins on the MWNT surface, despite that the TEM
417 imaging of proteins is seriously hampered by the low visibility
418 as they consist of light atoms. Balavoine et al.³¹ reported of
419 streptavidin on MWNTs while Ling et al.³² reported of a
420 recognition protein (C1q) on the MWNT. Both works are on
421 arc-discharge MWNTs, as in our case. Also, in both cases,
422 perpendicular or helical arrangement of the protein was
423 observed.

424 That there are very few works on the TEM imaging of
425 proteins physically adsorbed onto high-quality arc-discharge
426 synthesized MWNTs is understandable because of the multiple
427 problems involved both in sample preparation and the imaging
428 technique. Our AFM results support the tentative conclusion
429 from the above-mentioned two TEM works, where certain
430 proteins tend to arrange perpendicular to the tube axis. The
431 fact that avidin on graphite forms a random network built up
432 by chain formations, while on MWNTs, the corresponding
433 stripes are organized perpendicular to the tube axis, implies
434 that the avidin deposition energetically favors some degree of
435 curvature upon adsorption to a graphitic surface.

436 De Leo et al.¹² have reviewed, mainly from the simulation
437 point of view, the issue of proteins interfacing with graphitic
438 nanomaterials, including carbon nanotubes. Besides the
439 intermolecular forces, a crucial factor is what is called shape
440 complementarity, which means that certain proteins have a
441 concave-shaped section, which has been shown to act as a
442 docking site for fullerenes and SWNTs. Larger nanotubes, that
443 is, MWNTs, have a smaller curvature and shape complemen-
444 tarity may not be particularly effective. Yet, a few
445 experimental³⁰ and theoretical⁹ reports do claim increased
446 affinity of proteins to MWNTs with an increasing MWNT
447 diameter.

448 Finally, the pertinent question with protein assembly on
449 surfaces is that of their functionality. Our results demonstrate a
450 very specific behavior of avidin, as on graphite, the double layer
451 exhibits capture of b-AuNP while the monolayer does not. The
452 result was well confirmed by the blocking of the biotin sites in
453 the double layer so that no b-AuNP was adsorbed. These
454 findings suggest that the first avidin layer is unfolded and
455 represents protein which has lost the biological function. The
456 first layer then modifies the surface properties so that the
457 second layer stays functional.

458 ■ CONCLUSIONS

459 In conclusion, we have undertaken thorough experimentation
460 on the physisorption of avidin to chemically different flat
461 surfaces, Si and graphite, and also to the curved version of the
462 latter, on high-quality MWNTs of different diameters. The
463 difference between the behavior of avidin on Si and graphite is
464 drastic, in that on Si, avidin deposits as single globular
465 tetrameric units, while on graphite, spreading of avidin along
466 the surface occurs and it also agglomerates in chain-like
467 formations. Eventually, avidin on graphite forms irregular
468 networks of two-layer thick filaments. The upper avidins of this
469 double layer and the globular clusters on silicon exhibit
470 preserved functionality with respect to biotin binding, whereas
471 the first layer of avidin on graphite has lost its functionality. On
472 MWNTs, avidin, also upon deposition, agglomerates into 1D
473 formations as on graphite. However, as opposed to the
474 irregular network appearance on graphite, the cylindrical
475 nanometer-sized curvature favors ordering of avidin in a
476 perpendicular and at best periodical arrangement to the
477 MWNT axis. This work has significance within avidin–biotin
478 technology and may facilitate the engineering of protein–
479 surface interfaces in general.^{33,34} Our study reveals some
480 challenges associated with physisorption, but may also open
481 avenues for exploitation of surface-induced effects. The
482 phenomena of protein–surface interactions are still under-
483 stood only partly, as simulation requires large computing
484 power and the available experimental data are limited in
485 quality. The relatively well-defined variation in the exper-

486 imental parameters of this work (surface chemistry and
487 nanoscale topography) should help the field to make further
488 advances.

489 ■ ASSOCIATED CONTENT

490 ■ Supporting Information

491 The Supporting Information is available free of charge on the
492 ACS Publications website at DOI: 10.1021/acs.langmuir.8b02855.

494 MWNT material and deposition, surface character-
495 ization, and functionality of avidin on silicon (PDF)

496 ■ AUTHOR INFORMATION

497 Corresponding Author

498 *E-mail: markus.e.ahlskog@jyu.fi. Phone: +358 (0)
499 407284358.

500 ORCID

501 J. Jussi Toppari: 0000-0002-1698-5591

502 Vesa P. Hytönen: 0000-0002-9357-1480

503 Markus Ahlskog: 0000-0003-3479-2619

504 Notes

505 The authors declare no competing financial interest.

506 ■ ACKNOWLEDGMENTS

507 This work was financially supported by the Academy of
508 Finland through projects 263526, 130900, and 283011 for
509 J.J.T., 263540 and 290506 for V.P.H., and 263523 for M.A. We
510 thank Harlan Barker for insightful comments for the
511 manuscript.

512 ■ ADDITIONAL NOTE

513 ^awww.cytodiagnostics.com.

514 ■ REFERENCES

- 515 (1) Nel, A. E.; Mädler, L.; Velegol, D.; Xia, T.; Hoek, E. M. V.;
516 Somasundaran, P.; Klaessig, F.; Castranova, V.; Thompson, M.
517 Understanding biophysicochemical interactions at the nano-bio
518 interface. *Nat. Mater.* **2009**, *8*, 543–557.
- 519 (2) Anand, G.; Sharma, S.; Dutta, A. K.; Kumar, S. K.; Belfort, G.
520 Conformational Transitions of Adsorbed Proteins on Surfaces of
521 Varying Polarity. *Langmuir* **2010**, *26*, 10803–10811.
- 522 (3) Rabe, M.; Verdes, D.; Seeger, S. Understanding protein
523 adsorption phenomena at solid surfaces. *Adv. Colloid Interface Sci.*
524 **2011**, *162*, 87–106.
- 525 (4) Kastantin, M.; Langdon, B. B.; Schwartz, D. K. A bottom-up
526 approach to understanding protein layer formation at solid-liquid
527 interfaces. *Adv. Colloid Interface Sci.* **2014**, *207*, 240–252, Special
528 Issue: Helmut M. Möhwald Honorary Issue.
- 529 (5) Spaargaren, J.; Giesen, P. L. A.; Janssen, M. P.; Voorberg, J.;
530 Willems, G. M.; van Mourik, J. A. Binding of blood coagulation factor
531 VIII and its light chain to phosphatidylserine/phosphatidylcholine
532 bilayers as measured by ellipsometry. *Biochem. J.* **1995**, *310*, 539–545.
- 533 (6) Sommerfeld, J.; Richter, J.; Niepelt, R.; Kosan, S.; Keller, T. F.;
534 Jandt, K. D.; Ronning, C. Protein Adsorption on Nano-scaled,
535 Rippled TiO₂ and Si Surfaces. *Biointerphases* **2012**, *7*, 55.
- 536 (7) Nejad, M. A.; Mücksch, C.; Urbassek, H. M. Insulin adsorption
537 on crystalline SiO₂: Comparison between polar and nonpolar surfaces
538 using accelerated molecular-dynamics simulations. *Chem. Phys. Lett.*
539 **2017**, *670*, 77–83.
- 540 (8) Zou, X.; Wei, S.; Jasensky, J.; Xiao, M.; Wang, Q.; Brooks, C. L.,
541 III; Chen, Z. Molecular Interactions between Graphene and Biological
542 Molecules. *J. Am. Chem. Soc.* **2017**, *139*, 1928–1936.
- 543 (9) Raffaini, G.; Ganazzoli, F. Surface Ordering of Proteins
544 Adsorbed on Graphite. *J. Phys. Chem. B* **2004**, *108*, 13850–13854.

- (10) Mücksch, C.; Urbassek, H. M. Molecular Dynamics Simulation
of Free and Forced BSA Adsorption on a Hydrophobic Graphite
Surface. *Langmuir* **2011**, *27*, 12938–12943.
- (11) Mücksch, C.; Rösch, C.; Müller-Renno, C.; Ziegler, C.;
Urbassek, H. M. Consequences of Hydrocarbon Contamination for
Wettability and Protein Adsorption on Graphite Surfaces. *J. Phys.*
Chem. C **2015**, *119*, 12496–12501.
- (12) De Leo, F.; Magistrato, A.; Bonifazi, D. Interfacing proteins
with graphitic nanomaterials: from spontaneous attraction to tailored
assemblies. *Chem. Soc. Rev.* **2015**, *44*, 6916–6953.
- (13) Iijima, S. Helical microtubules of graphitic carbon. *Nature*
1991, *354*, 56–58.
- (14) Mtsuko, D.; Koshio, A.; Yudasaka, M.; Iijima, S.; Ahlskog, M.
Measurements of the transport gap in semiconducting multiwalled
carbon nanotubes with varying diameter and length. *Phys. Rev. B:*
Condens. Matter Mater. Phys. **2015**, *91*, 195426.
- (15) Laitinen, O. H.; Nordlund, H. R.; Hytönen, V. P.; Kulomaa, M.
S. Brave new (strept)avidins in biotechnology. *Trends Biotechnol.*
2007, *25*, 269–277.
- (16) Hytönen, V. P.; Määttä, J. A. E.; Nyholm, T. K. M.; Livnah, O.;
Eisenberg-Domovich, Y.; Hyre, D.; Nordlund, H. R.; Hörhå, J.;
Niskanen, E. A.; Paldanius, T.; et al. Design and construction of highly
stable, protease-resistant chimeric avidins. *J. Biol. Chem.* **2005**, *280*,
10228–10233.
- (17) Hokkanen, M. J.; Lautala, S.; Shao, D.; Turpeinen, T.;
Koivistoinen, J.; Ahlskog, M. On-chip purification via liquid
immersion of arc-discharge synthesized multiwalled carbon nano-
tubes. *Appl. Phys. A: Mater. Sci. Process.* **2016**, *122*, 634.
- (18) Livnah, O.; Bayer, E. A.; Wilchek, M.; Sussman, J. L. Three-
dimensional structures of avidin and the avidin-biotin complex. *Proc.*
Natl. Acad. Sci. U.S.A. **1993**, *90*, 5076–5080.
- (19) Reichert, J.; Wei, G.; Jandt, K. D. Formation and Topotactical
Orientation of Fibrinogen Nanofibrils on Graphite Nanostructures.
Adv. Eng. Mater. **2009**, *11*, B177–B181.
- (20) Izrailev, S.; Stepaniants, S.; Balsera, M.; Oono, Y.; Schulten, K.
Molecular dynamics study of unbinding of the avidin-biotin complex.
Biophys. J. **1997**, *72*, 1568–1581.
- (21) Wang, J.; Dixon, R.; Kollman, P. A. Ranking ligand binding
affinities with avidin: a molecular dynamics-based interaction energy
study. *Proteins: Struct., Funct., Bioinf.* **1999**, *34*, 69–81.
- (22) Söderhjelm, P.; Kongsted, J.; Ryde, U. Ligand Affinities
Estimated by Quantum Chemical Calculations. *J. Chem. Theory*
Comput. **2010**, *6*, 1726–1737.
- (23) Macwan, I.; Khan, M. D. H.; Aphale, A.; Singh, S.; Liu, J.;
Hingorani, M.; Patra, P. Interactions between avidin and graphene for
development of a biosensing platform. *Biosens. Bioelectron.* **2017**, *89*,
326–333.
- (24) Barinov, N. A.; Prokhorov, V. V.; Dubrovin, E. V.; Klinov, D. V.
AFM visualization at a single-molecule level of denaturated states of
proteins on graphite. *Colloids Surf., B* **2016**, *146*, 777–784.
- (25) Zauner, D.; Taskinen, B.; Eichinger, D.; Flattinger, C.;
Ruttmann, B.; Knoglinger, C.; Traxler, L.; Ebner, A.; Gruber, H. J.;
Hytönen, V. P. Regenerative biosensor chips based on switchable
mutants of avidin-A systematic study. *Sens. Actuators, B* **2016**, *229*,
646–654.
- (26) Herrig, A.; Janke, M.; Austermann, J.; Gerke, V.; Janshoff, A.;
Steinem, C. Cooperative Adsorption of Ezrin on PIP₂-Containing
Membranes†. *Biochemistry* **2006**, *45*, 13025–13034.
- (27) Helbing, C.; Stoeßel, R.; Hering, D. A.; Arras, M. M. L.;
Bossert, J.; Jandt, K. D. pH-Dependent Ordered Fibrinogen
Adsorption on Polyethylene Single Crystals. *Langmuir* **2016**, *32*,
11868–11877.
- (28) Lin, Y.; Allard, L. F.; Sun, Y.-P. Protein-Affinity of Single-
Walled Carbon Nanotubes in Water. *J. Phys. Chem. B* **2004**, *108*,
3760–3764.
- (29) Karajanagi, S. S.; Yang, H.; Asuri, P.; Sellitto, E.; Dordick, J. S.;
Kane, R. S. Protein-Assisted Solubilization of Single-Walled Carbon
Nanotubes. *Langmuir* **2006**, *22*, 1392–1395.

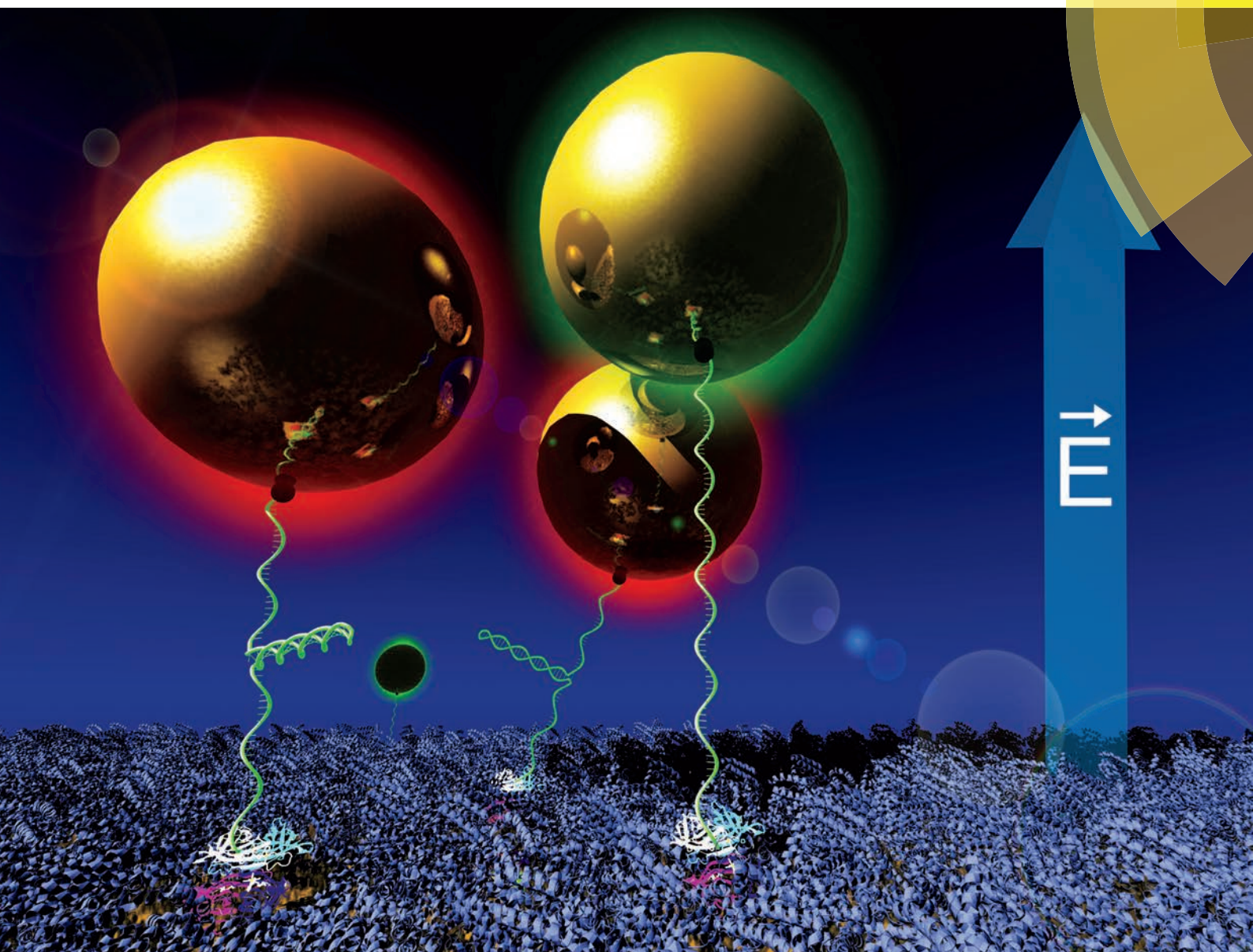
- 613 (30) Mu, Q.; Liu, W.; Xing, Y.; Zhou, H.; Li, Z.; Zhang, Y.; Ji, L.;
614 Wang, F.; Si, Z.; Zhang, B.; et al. Protein Binding by Functionalized
615 Multiwalled Carbon Nanotubes Is Governed by the Surface
616 Chemistry of Both Parties and the Nanotube Diameter. *J. Phys.*
617 *Chem. C* **2008**, *112*, 3300–3307.
- 618 (31) Balavoine, F.; Schultz, P.; Richard, C.; Mallouh, V.; Ebbesen, T.
619 W.; Mioskowski, C. Helical Crystallization of Proteins on Carbon
620 Nanotubes: A First Step towards the Development of New
621 Biosensors. *Angew. Chem., Int. Ed.* **1999**, *38*, 1912–1915.
- 622 (32) Ling, W. L.; Biro, A.; Bally, I.; Tacnet, P.; Deniaud, A.; Doris,
623 E.; Frachet, P.; Schoehn, G.; Pebay-Peyroula, E.; Arlaud, G. J. Proteins
624 of the Innate Immune System Crystallize on Carbon Nanotubes but
625 Are Not Activated. *ACS Nano* **2011**, *5*, 730–737.
- 626 (33) Tapio, K.; Shao, D.; Auer, S.; Tuppurainen, J.; Ahlskog, M.;
627 Hytönen, V. P.; Toppari, J. J. A DNA nanoparticle actuator enabling
628 optical monitoring of nanoscale movements induced by an electric
629 field. *Nanoscale* **2018**, *10*, 19297–19309.
- 630 (34) Taskinen, B.; Zauner, D.; Lehtonen, S. I.; Koskinen, M.;
631 Thomson, C.; Kähkönen, N.; Kukkurainen, S.; Määttä, J. A. E.;
632 Ihalainen, T. O.; Kulomaa, M. S.; et al. Switchavidin: Reversible
633 Biotin-Avidin-Biotin Bridges with High Affinity and Specificity.
634 *Bioconjugate Chem.* **2014**, *25*, 2233–2243.

**DNA-nanoparticle actuator enabling
optical monitoring of nanoscale
movements induced by electric field
(Nanoscale)**

A.III

Nanoscale

rsc.li/nanoscale



ISSN 2040-3372



PAPER

J. Jussi Toppari *et al.*
A DNA–nanoparticle actuator enabling optical monitoring of nanoscale movements induced by an electric field





Cite this: *Nanoscale*, 2018, **10**, 19297

A DNA–nanoparticle actuator enabling optical monitoring of nanoscale movements induced by an electric field†

Kosti Tapio,^a Dongkai Shao,^{‡a} Sanna Auer,[§]  [§]  Jussipekka Tuppurainen,^c Markus Ahlskog,^a Vesa P. Hytönen  ^b and J. Jussi Toppari  ^{*a}

Merging biological and non-biological matter to fabricate nanoscale assemblies with controllable motion and function is of great interest due to its potential application, for example, in diagnostics and biosensing. Here, we have constructed a DNA-based bionanoactuator that interfaces with biological and non-biological matter *via* an electric field in a reversibly controllable fashion. The read-out of the actuator is based on motion-induced changes in the plasmon resonance of a gold nanoparticle immobilized to a gold surface by single stranded DNA. The motion of the gold nanoparticle and thus the conformational changes of the DNA under varying electric field were analyzed by dark field spectroscopy. After this basic characterization, another actuator was built utilizing hairpin-DNA coated gold nanoparticles, where the hairpin-DNA induced discrete transitions between two specific open-loop and folded-loop states. These two states and the transition dynamics between them were clearly visible in the actuator behavior. The demonstrated nanoactuator concept could be readily extended to inspection of conformational changes of other biomolecules as well. Besides, this concept enables other possibilities in applications like surface-enhanced Raman spectroscopy and fluorescence enhancement, since the specific wavelength of the plasmon resonance of the actuator can be tuned by the external voltage.

Received 9th July 2018,
Accepted 17th August 2018

DOI: 10.1039/c8nr05535a

rscl.li/nanoscale

Introduction

Nature offers excellent building blocks for almost all of the functions and devices used in modern semiconductor-based technology and materials science. However, reliable interfaces between the biological and non-biological domains remain a challenge. Therefore, bionanoactuators and -sensors have been under intense study during the past few decades. In particular, bionanosensors have attracted great attention in, *e.g.*, the environment,^{1,2} food^{1,3} and biomedical industries,^{2,4} where the sensors commonly use either substrate-immobilized or suspended probes, which through optical,⁵ mechanical,⁶ electrical⁷ or chemical^{8–10} interactions assay the surrounding medium to extract information. Some more sophisticated

nanosensors may require outside activation or actuation *via*, *e.g.*, solution flow,¹¹ electric or magnetic fields¹² or thermo-optical effects.¹³ If the purpose of the nanodevice is to controllably change the active state of any chemical or physical quantity, rather than detect any target, it can be called a nanoactuator, even though some kind of sensing system is needed to read its state.

One of the most interesting molecules for biosensor and -actuator applications is DNA, due to its robust self-assembly properties, reasonable price and wide range of available chemical modifications. DNA has been utilized in applications ranging from, *e.g.*, electronics^{14,15} to biosensing,^{16,17} and the immobilization of DNA strands on surfaces has been studied extensively.^{18,19} However, their use in electrical or optical probing is still challenging,^{15,20} due to the lack of clear electrical or optical properties. Meanwhile, metallic nanoparticles (NP) have become increasingly popular due to their strong plasmonic and electric properties,²¹ enabling even probing of individual particles or structures to obtain information about their state or surroundings.^{22,23} In this work, we combine the advantages of the selective binding scheme of biomolecules, especially DNA, to the extremely sensitive optical detection of metallic NPs, so that the system can be reversibly manipulated using external triggers and simultaneously monitored optically.

^aUniversity of Jyväskylä, Department of Physics, Nanoscience Center, FI-40014 University of Jyväskylä, P.O. Box 35, Finland. E-mail: j.jussi.toppari@jyu.fi

^bFaculty of Medicine and Life Sciences and BioMediTech, University of Tampere, Arvo Ylpön katu 34, FI-33520 Tampere, Finland and Fimlab laboratories, Biokatu 4, FI-33520 Tampere, Finland

^cBioNavis Ltd, Hermiankatu 6-8 H, FI-33720 Tampere, Finland

† Electronic supplementary information (ESI) available: Additional data and analysis, and experimental details. See DOI: 10.1039/c8nr05535a

‡ These authors contributed equally to this work.

§ Present address: BioMensio Ltd, Hermiankatu 6-8 H, FI-33720 Tampere.

Here, we present a new type of bionanoactuator based on DNA-functionalized gold nanoparticles (AuNP), where the plasmonic coupling between the AuNP and a gold surface is used for read-out. The charged AuNPs are anchored to the gold surface *via* DNA linkers and moved reversibly by applying an electric field to the liquid medium surrounding them. Due to the distance-dependent plasmonic coupling between the AuNP and the Au-surface, the localized surface plasmon resonances (LSPR) of the AuNP will either redshift or blueshift. This spectral change is used to determine the distance between the AuNP and the surface, and is further correlated to the conformation of the DNA linker to study its mechanical properties and behavior. We utilized plain single stranded DNA (ssDNA) with varying lengths to calibrate the system, and afterwards a hairpin-DNA to study the folding and unfolding of it under a mechanical load applied *via* AuNPs dragged by the electric field. This yields information on the unfolding energetics of individual DNA strands.

The demonstrated scheme can be readily extended to study also the conformation of other biomolecules by replacing the DNA between the AuNP and the surface by any biomolecule, such as talin protein containing relatively soft alpha-helical structures, which greatly elongate under a mechanical load in living cells.^{24,25} Also other reasons for conformational changes, like pH in the case of Influenza Hemagglutinin protein,²⁶ could be studied in a similar way. In addition, the plasmonic coupling between the AuNP and the surface will induce high electric fields, which can be used, *e.g.*, in surface-enhanced Raman spectroscopy (SERS), where typically the plasmon resonance of the system cannot be adjusted after fabrication,^{27,28} or if they can be adjusted,^{29,30} then the process is irreversible. Our DNA-nanoparticle bionanoactuator adds that functionality with a reversibly tunable surface plasmon resonance.

Experimental

The DNA strands (see ESI Table S3† for DNA sequences) were purchased from Integrated DNA Technology (IDT, Coralville, Iowa, USA). Neutral cysteine-tagged chimeric avidin (nChiAvid-Cys) was produced in *Escherichia coli* and purified using 2-iminobiotin affinity chromatography.³¹ Bovine serum albumin (BSA), D-biotin, poly(ethylene glycol) methyl ether thiol (SH-PEG, $M_n = 800$), bis(*p*-sulfonatophenyl)phenylphosphine dihydrate dipotassium salt (BSPP) and AuNPs with 80 nm diameter (lot # MKBV4360 V) were purchased from Sigma-Aldrich (3050 Spruce St., St Louis, MO 63103, USA). The UV-vis absorption spectra of the AuNPs were measured using a PerkinElmer Lambda 850 UV-vis spectrometer. The ITO coverslip (8–12 Ω per sq, lot # 1200330) glasses were purchased from SPI Supplies (West Chester, Pennsylvania, USA).

Preparation of AuNPs coated with biotinylated DNAs

For DNA–AuNP conjugation, we followed a similar protocol to Storhoff and Mirkin with a few minor adjustments.^{32,33} For

preconjugation, the spherical AuNPs were surface stabilized by treating them with BSPP solutions overnight (~12 h). First, 0.2 mg of BSPP was weighed and 300 μ l of plain AuNP solution (156 pM) was used to dissolve it (BSPP concentration = 0.67 mg ml⁻¹). Attachment of DNA onto AuNPs was done *via* thiolated 3'-end of the ssDNA. Note that the thiol was included in every DNA strand shown below even if it is not mentioned separately. The 5'-end was modified with biotin or left blank depending on the case. Before conjugation, the ssDNA strands were treated with 1 mM TCEP to cleave the disulfide bonds between thiol-groups. The DNA–TCEP solution was incubated for 1 h and then 38 μ l of the solution was added to a separate tube containing 300 μ l of the BSPP-treated AuNPs. The DNA–AuNP solution was mixed overnight after which we started to add salt buffer to detach the free end of the DNA from the AuNP surface. A typical problem with large AuNPs (>60 nm) is that they are very unstable even in buffers with moderate ion concentration in contrast to small AuNPs, which are resistant against high ionic strength. For this reason, we adjusted the salt concentration slowly during a 3–4 day period, until a slight color change was observed. This was done by adding 2 μ l of 60 mM NaCl to the tube containing 338 μ l of the DNA–AuNP solution. After approximately 8 h, another 2 μ l of 60 mM NaCl buffer was added, followed by overnight incubation. This was repeated until a color change was observed, with the final concentration of 2.1 mM NaCl.

The mixtures were centrifuged (2 min, 2000 rcf) and the supernatant was removed. The volume was adjusted to 300 μ l by adding 0.1 mM NaPhos and 1 mM NaCl (NaPo–NaCl buffer, pH 7.6) and the centrifugation process was repeated 2 times. In the last run the volume was adjusted to 50–100 μ l with the same buffer. Finally, the UV-vis spectra and the hydrodynamic radius, D , were recorded from the final solution. The UV-vis spectra revealed that the LSPR peak is roughly the same for all of the samples with or without DNA (see ESI Fig. S1†), but the hydrodynamic radius differed as explained in the Results and discussion section.

For the calibration tests, we utilized thiolated and biotinylated random ssDNA sequences with varying length, but for the final study, hairpin-DNA was utilized. The hairpin-DNA consists of a middle loop section and two arms (3' and 5' end) with different lengths. The loop has a length of 25 bases and when folded it forms 10 bp zipper ($T_m = 69$ °C, Mfold). The 5' end arm has a length of 15 bases and the 3' end arm has a length of 8 bases. To control the biotin density on the AuNPs, we made a solution (98 μ l) that contained biotinylated DNA (hairpin-DNA or ssDNA) and thiolated a 3 nm long DNA strand with a random sequence and without biotin (blocking-DNA). To test the optimal ratio the molar ratio of hairpin-DNA : blocking-DNA was altered from 1 : 0 to 1 : 999. Finally, the ratio 1 : 999 was chosen for all the experiments (ssDNA and hairpin-DNA); except for comparing the motion of individual particles under the influence of an electric field, we used AuNPs coated only with hairpin-DNA, as described in the Results and discussion section.

Protein and nanoparticle attachment to gold surfaces in the SPR setup

A BioNavis SPR Navi 200 MP-SPR device and BioNavis thin glass substrates (Schott D263 T glass slides) coated with gold layers were used to detect the resonance angle SPR (RA-SPR) signal resulting from the biomolecule and the gold particle binding. The experimental procedures were based on the literature-established methods.³⁴ The sensors were fabricated by first cleaning the glass substrate using reactive ion etching (RIE) with O₂ plasma (20 W, 15 s), and then the sample was placed inside a JYU self-made UHV e-beam evaporator. First, 2 nm adhesion layer of titanium was evaporated followed by the evaporation of 42 or 48 nm gold layer.

In the SPR measurements, the duration of each protein, biomolecule or AuNP injection was 16 min. Phosphate buffered saline (PBS) was used as a running buffer and the total sample volume was 300 µl. The avidins were pre-treated with TCEP to reduce the amount of possible avidin dimers. Typical measurements started by mixing 6–10 µl of chimeric avidin (0.75 mg ml⁻¹) with 6 µl of TCEP (1 mM) and finally adjusting the volume to 300 µl with PBS. This solution was incubated for 10 min at RT before injection. At the same time, base piranha solution was prepared by mixing NH₄OH : H₂O₂ : H₂O = 1 : 1 : 5; the solution was heated to 80 °C and a gold sensor was placed in the piranha solution for 10 min.³⁵ After 10 min, the sensor was immersed in water for a short duration (5–10 s) and then dried using N₂ flow and lastly it was placed inside the SPR device (Navi 200 MP-SPR).

The sensor chamber was quickly flushed with PBS buffer and the chimeric avidin was injected into PBS. After roughly 16 min, the injection was stopped and the injection lines were quickly washed three times with 300 µl of the buffer. Next, 300 µl of (0.29 mM) SH-PEG in PBS or (500 µg ml⁻¹) BSA in PBS was injected into the chamber and after 16 min the previous purging procedure was repeated. Similar procedures were followed for biotin and AuNP injections. Biotin was injected into PBS and the AuNPs were typically diluted 30–60 times in PBS to reduce the bulk effect. The tracked resonance angles were roughly at 66° for a 785 nm laser.

After the SPR measurements, the gold sensor was removed from the MP-SPR device, ddH₂O was added to the area of the SPR chambers and a coverslip was placed on top of the sensor. The dark field (DF) images of the chambers were taken using an Olympus microscope equipped with a 50× DF objective (MPLANFL N) and a Canon camera (EO5 D6, see the ESI† for more details of the microscope setup).

Assessment of the interaction between avidin and biotinylated-AuNP using DLS

The biotin–avidin interaction was investigated by mixing the biotinylated-AuNPs with the chimeric avidin. In short, 1 µl of chimeric avidin solution (0.75 mg ml⁻¹) was added to 9 µl of PBS and 0.5 µl of TCEP and incubated for 10 min. Then 2 µl of this solution was added to 10 µl of biotinylated-AuNP solution and the mixture was incubated for 10 min. Finally, 12 µl of the

solution was added to 4 ml ddH₂O in a Kartell UV-vis cuvette and mixed thoroughly. The water was filtered beforehand using a 0.1 µm pore size syringe filter and the cuvette was washed three times with the filtered water before use. The cuvette was placed inside a DLS analyzer (Beckman Coulter N5 Submicron Particle Size Analyzer) and the mean hydrodynamic diameter and the polydispersity index were recorded. The measurement angle was 90° in all of the measurements and the laser light source had a wavelength of 632 nm. For comparison, we also measured the hydrodynamic diameter of the original biotinylated-AuNP solutions and calculated the relative increase in the diameter after the avidin aggregation compared to the initial diameter.

Preparation of the gold surface for immobilization of biotinylated AuNPs

The Au-surface was prepared by cutting roughly 6 mm × 6 mm boron-doped (100) silicon chips and cleaning the surface in a heated acetone bath followed by sonication in an isopropanol bath for 30 s. After this, the surface was still further cleaned using O₂ plasma (Oxford Instruments/Plasmalab 80plus RIE: O₂ flow 50 sccm, 60 s and 100 W) and placed inside a vacuum evaporator. For making reliable electrical contacts between the front surface and the backside of the chip, the titanium adhesion layer and the subsequent gold layer were evaporated in three different angles: perpendicular to the front surface, at 45 degree with respect to the backside surface and perpendicular to the backside surface. For titanium, a 2 nm layer was evaporated at each direction. For gold, a 42 nm layer was evaporated in the front side and 10 nm for each angle in the backside.

Immobilization of biotinylated AuNPs on a gold surface coated with chimeric avidins

The experimental setup is described in detail in the ESI,† and a more general description is provided here. The nChiAvd-Cys solution was prepared by mixing 2 µl of Cys-tagged charge-neutralized chimeric avidin (0.75 mg ml⁻¹) to 1 µl of TCEP (1 mM) and 96 µl PBS and incubating the mixture for 10 min at room temperature. At the same time, the Au-surface was treated with a similar basic piranha solution as in the SPR measurements (NH₄OH : H₂O₂ : H₂O = 1 : 1 : 5) for 10 min at 80 °C. After the piranha treatment, the Au-surface was rinsed in ddH₂O and the backside was dried using a clean-room tissue. The chip was connected to a self-made, polycarbonate holder (see ESI Fig. S5†) by adding a small drop of conductive silver grease (OW Circuits Works) to the gold layer on the backside of the chip, circling the paste with varnish and gluing the chip to aluminium connections on the holder. After a few minutes, 50 µl of the avidin solution was added to the Au-surface and incubated for 30 min. Then the surface was washed with PBS, substituted with 50 µl of 1 mg ml⁻¹ BSA in PBS and the solution was incubated for 30 min. After this, the surface was washed with NaPo–NaCl buffer.

In order to prepare the electric field apparatus, a small layer of silver paste was added to both contacts for ITO-coated

cover glass on the holder and the ITO-coated cover glass was placed on top of the Au-surface. Then the coverslip was fixed using scotch tape and the resistance through ITO was measured to ensure good contact. Without the silver paste the contacts were typically poor. The input and output flow channels on the holder were pre-wetted for the AuNP injection, the holder with the Au-surface was placed on the microscope and ISMATEC tubing pump (ISM597D) was inserted into the output channel. An image of the plain Au-surface was recorded for reference. Then, the extra water from the chamber containing the chip was removed and 50 μl of the biotinylated AuNP (30–60 pM) in NaPo–NaCl buffer was injected into the chamber. The biotin–AuNP deposition was monitored for 15–90 minutes, until enough particles were immobilized on the surface but the density was still suitable for the LSPR scattering measurements (particle-to-particle distance larger than 10 μm). Then 1–2 ml of NaPo–NaCl buffer was run through the chamber until all of the free AuNPs were removed.

Dark field measurement of the LSPR scattering spectra and optical imaging

Here, we provide a brief description of the dark field microscope setup and the LSPR spectra measurements, and a more detailed description is provided in the ESI.† The dark field microscope setup is illustrated in Fig. S6.† The scattered light from individual gold nanoparticles was collected into the Acton SP2150 spectrograph equipped with an Andor Ivac CCD camera *via* an optical fiber (core size 300 μm). To do this the tip of fiber was placed on the image plane of the output port of the microscope, and the part of the dark field image on the fiber spot was thus extracted to the spectrograph. The fiber tip could be visualized by light illumination from the spectrograph side, and individual particles could be selected for the LSPR measurement by moving the fiber spot on the particles using an XYZ-micrometer stage. The size of the fiber spot was roughly 10 μm , and the deposition of biotin–AuNPs was stopped before the average particle-to-particle distance became smaller than 10 μm to enable individual particle measurements.

The LSPR measurements started by moving the fiber spot on the desired particle, waiting for 1 min and recording the initial, zero voltage spectra with 3–5 s integration time and averaging of 3 spectra. The following voltage sweeps consisted of a voltage change, 1 min stabilization time and recording the LSPR spectra with the same averaging and the integration time as before. Apart from changes in the transparency of ITO, we did not observe any changes in the background signal during the voltage sweeping, and for each particle, we recorded the background next to it on an empty spot. A Canon EOS 6D camera was connected to the other output port of the microscope, and we used the Canon EOS utility software to remotely control the camera, to take dark field optical images and to monitor the sample surface during and after deposition of biotin–AuNPs. For the dark field images, the exposure time was 2.5 to 4 seconds.

Measurement of the effect of the applied electric field

For the large scale optical analysis, the voltage was swept from negative side to positive side (typically from -3 V to $+3\text{ V}$ and back) to see the changes in the LSPR spectra of the surface-bound AuNPs. The voltage biasing is with respect to the gold surface. After each voltage step, the system was let to stabilize for 1 min. The voltage was swept 3 times from the positive side to the negative side, and in each step an optical image was taken. Then, images were processed to see which particles changed color notably (see ESI Fig. S7 and S8†). The LSPR scattering spectra were measured for these particles. The microscope focus was checked and adjusted frequently during the measurements. Applying voltages higher than $\pm 3\text{ V}$ resulted in irreversible changes in the ITO due to the decomposition of InO_2 and SnO_2 ,³⁶ which eventually blocked the view to the Au-surface completely. Also, higher voltages caused bubbling in the system, and for these reasons, the voltage was kept as low as possible.

For the individual particle spectra analyses, depending on the amount of hairpin-DNA on AuNPs, the voltage was swept either from -0.5 V to $+0.5\text{ V}$ with either 0.1 or 0.05 step (0.1% ratio of hairpin-DNA) or from -3 V to $+3\text{ V}$ with 0.5 V step (pure hairpin-DNA). After each voltage step, the system was left to equilibrate for 1 min and the LSPR scattering spectra were recorded. This was repeated for several voltage sweeps from the negative to positive side. Both the individual scattering spectra of nanoparticles and the RGB data from optical images were analyzed to determine the individual and mass scale behaviors of the biotinylated-AuNPs.

Results and discussion

Our electric field controllable DNA–AuNP-nanoactuator consists of a gold surface acting as an electrode, a DNA of interest attached to this surface from one end, and a negatively charged gold nanoparticle attached to the other end of the DNA. AuNP is used as an electric field controlled handle to stretch the DNA to change its conformation. The assembly of the nanoactuator is shown in Fig. 1a–c: (a) the binding of neutral cysteine-tagged chimeric avidins (nChiAvid-Cys) on the gold surface, (b) the passivation of the rest of the surface using a blocking agent (BSA or SH-PEG), and finally (c) the immobilization of 80 nm in diameter AuNPs, functionalized with biotinylated DNA (ssDNA or hairpin-DNA) and otherwise passivated with blocking-DNA.

Initially, to test the immobilization, we used AuNPs coated with two different ssDNAs that either had both a thiol- and a biotin-end (biotin-DNA) or just the thiol-end (blocking-DNA). Later on, to demonstrate the functionality of ready DNA–AuNP-nanoactuators, we used thiolated and biotinylated ssDNAs with varying lengths (3 nm, 8 nm and 15 nm, labelled DNA-s3nm, DNA-s8nm and DNA-s15nm). For a general discussion, we will refer to all AuNPs coated with different biotinylated DNAs as biotin–AuNPs. The results of these tests were then applied to study the folding of a thiolated and biotinyl-

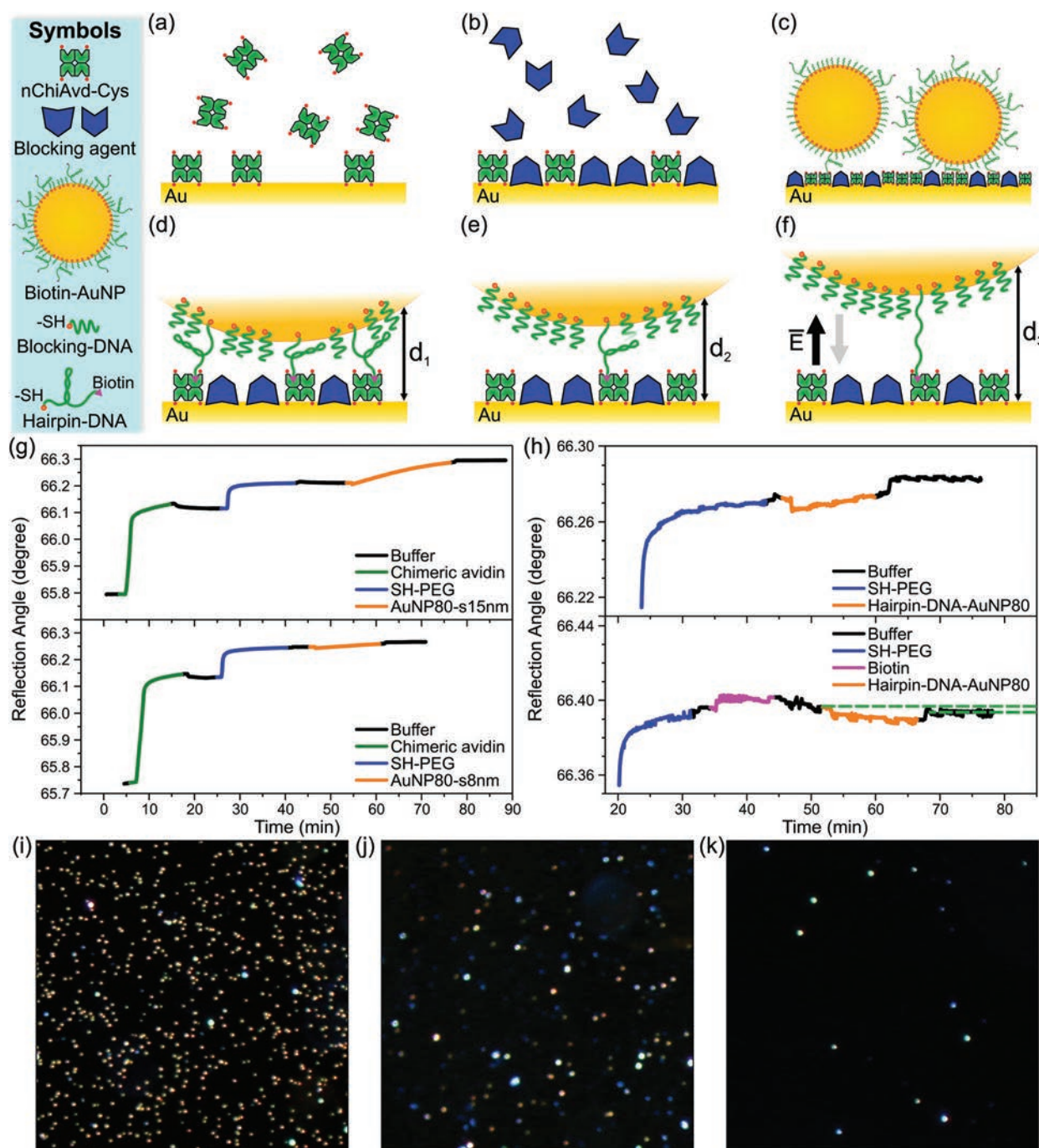


Fig. 1 Schematic illustration of the DNA–AuNP–nanoactuator and SPR characterization of its assembly. (a) Binding of neutral cysteine-tagged chimeric avidin (nChiAvid-Cys) on a gold surface. (b) The passivation of the remaining surface using a blocking agent (BSA or SH-PEG), (c) immobilization of AuNPs functionalized with biotinylated DNA. (d, e) After immobilization, the biotin–DNA (hairpin-DNA or plain ssDNA) is in a folded state and the particle is located close to the gold surface. The distance d to the surface and the mobility of AuNP are influenced by the number of linking DNAs, where more linking molecules indicate less mobility and thus shorter distance to the gold surface (distance d_1 versus d_2). (f) By applying an electric field the DNA hairpin can be opened (or ssDNA straightened) and the particle is pushed away from the surface ($d_3 > d_2$). When the electric field is switched off, the DNA loop can refold. (g) SPR characterization of the assembly steps from (a) to (c) using AuNPs coated with 8 nm or 15 nm ssDNA linker. The binding of nChiAvid-Cys, blocking agent (SH-PEG) and biotin–AuNP is detected as positive shifts in the resonant angle. (h) A similar SPR characterization as in (g), but the specific avidin–biotin binding interaction is confirmed by passivating the surface bound avidins by free biotin before biotin–DNA attachment as a negative control (lower graph), and comparing it to the regular binding of the hairpin-DNA–AuNPs (upper graph). The green dashed lines in the lower graph indicate the slight negative shift for the binding of AuNP due to biotin passivation. (i–k) Dark field images of the surface after immobilization of the hairpin-DNA–AuNPs. (i) The surface after the process depicted in a–c; (j) the surface after the process involving additional passivation with free biotins as shown in the lower graph of h; (k) a plain gold surface. Figure (i) shows a large amount of AuNPs with the same color, which can be attributed to the same distance from the surface and thus to specific binding. The AuNPs with varying colors (j, k) indicate unspecific binding with varying distances. The widths of the images (i–k) are roughly 100 μm .

lated hairpin-DNA, where the opening and re-hybridization of the double stranded part adds additional entropy constraint, leading to a switch-like behavior.

During the operation of the nanoactuator, the DNAs between the AuNP and the Au-surface are stretched by moving the charged AuNPs with the electric field (Fig. 1e and f), while optically tracking the particle position by the change in its LSPR resonance, *i.e.*, the scattering spectrum measured with dark field microscopy. The position of the particle can be further correlated to the conformation of the DNA as shown in Fig. 1e and f. We investigated the behavior of the nanoactuators both by monitoring individual particles as well as by analyzing an ensemble of particles. Also, for the hairpin-DNA, we studied the influence of the amount of biotin-avidin binding sites on the motion of the nanoactuator by varying the ratio between the hairpin-DNA and blocking-DNA attached to AuNPs (Fig. 1d and e).

Assembly of the DNA-AuNP nanoactuator

There are at least three major points to consider in the actuator design to obtain as freely moving AuNP as possible. First, the cysteine-tagged chimeric avidin was chosen as a platform for biotin targeted immobilization, since it allows a higher degree of control in the orientation of the avidin and in the motion of the particle while still retaining a strong interaction with biotin ($K_a = 10^{15} \text{ M}^{-1}$).^{37,38} Second, the blocking agent used to passivate the unoccupied surface after avidin immobilization is required, since the unspecific binding of biotin-AuNPs on the surface could greatly hinder the operation of the well-assembled actuators. Third, in addition to the length of the DNA linker, also the number of them connecting the individual AuNP and surface-immobilized avidin will set a limit on how far above the surface the particle can be lifted (Fig. 1d and e), as well as controlling the force needed for particle displacement.

To address the first two points, and also, partially the third one, we used Resonance Angle Surface Plasmon Resonance (RA-SPR, Fig. 1g and h and S4†) to characterize the binding of the chimeric avidin (Fig. 1a), the surface blocking agent (Fig. 1b) and the biotin-AuNPs (Fig. 1c). In addition, immobilization of the biotin-AuNPs was also confirmed afterwards by using dark field microscopy (Fig. 1i-k).

The SPR measurements were carried out using standard procedures (see the Methods section).³⁴ In each deposition step, a 16 min injection of the proteins or polymers to the sensor surface was followed by flushing of the measurement chamber using phosphate buffered saline (PBS) buffer, followed by the next injection. The binding of avidin was detected as a positive shift in the SPR signal (Fig. 1g, green solid lines), which is expected for a material with non-negative, non-complex permittivity.^{39,40} After 3.5–4.5 min injection, the binding curve started to reach a plateau, indicating that the surface becomes fully coated with avidins. The subsequent blocking agent (SH-PEG) injection followed a similar trend (Fig. 1g, blue lines), but the plateau was reached faster, since a large portion of the surface was already covered by the avidins,

and the smaller blocking agents move more rapidly to the surface than the avidins.

To study the immobilization of biotin-AuNPs, we used hairpin-DNA-AuNPs, AuNP-s8nm and AuNP-s15nm on the avidin-functionalized and passivated surface. These ssDNAs were chosen, since their lengths correspond to the hairpin-DNA in the folded and open states (see the Methods section and ESI† for more details). The AuNP-s15nm had a higher positive SPR angle shift than the AuNP-s8nm as shown in Fig. 1g, because of a different coupling between the LSPR of the AuNP and the Au-surface. Several publications have noted that the SPR signal depends strongly on the coupling between the AuNPs and the gold surface^{39,41} far away from the surface, AuNPs have only a regular mass-contribution (positive shift). But, when AuNPs are close to the Au-surface, as here, the SPR signal can have a significant positive shift, a negligible positive shift or even a negative shift, depending on the change in the LSPR.³⁹ Here this means that for the biotin-AuNPs with longer DNA-linkers the mass-contribution is dominant and a SPR shift is noticeable, while for the shorter linkers, the SPR shift is negligible. For hairpin-DNA, we observed a similar positive but small SPR shift as for the AuNP-s8nm, which indicates that the hairpin is mostly folded during the linking (Fig. 1h, upper curve).

To further clarify the situation, the immobilization of hairpin-DNA-AuNPs was verified by dark field microscopy afterwards (Fig. 1i). As a negative control, we passivated the avidins on the surface with an excess of free biotin after the application of the blocking agent, and tested the hairpin-DNA-AuNP immobilization (Fig. 1h, lower curve). In this case, no significant attachment of AuNP was observed in dark field microscopy (Fig. 1j) and the SPR shift was slightly negative (indicated by the green dashed lines in Fig. 1h), which could be attributed to a slight dissociation of avidins and the blocking agent.

Controlling the coverage of biotinylated DNA on AuNPs

The AuNPs can be bound to the surface *via* one or several DNA strands (Fig. 1d and e), and the number of bonds greatly influences the attachment and detachment properties of the particle⁴² and, especially, the mobility of it. To achieve the highest degree of motion for the actuator, we minimized the number of biotin-avidin bonds between a single particle and the surface. To achieve this, we fabricated AuNPs with different densities of biotins on the particle surface by mixing short blocking-DNAs without biotin with the longer biotinylated hairpin-DNA with molar ratios of hairpin-DNA : blocking-DNA varying between 1 : 0 and 1 : 999 during the functionalization process and characterized the result using Dynamic Light Scattering (DLS). In this case, the hydrodynamic diameter, D , of the biotin-AuNPs should be decreasing as the amount of shorter blocking DNA is increased, which was also observed (ESI Fig. S2†). However, due to the noisy result with a smaller amount of hairpin-DNA, we can only qualitatively correlate the hydrodynamic diameter to the amount of biotin groups on the surface of biotin-AuNPs.

For a better estimation of the amount of biotinylated DNA, we used the fact that a typical density of thiolated DNA on the surface of AuNP is 0.08–0.16 strand per nm².⁴³ The estimated total amount of DNA sequences on the surface of a single NP is then roughly 20 000, when taking into account the length of the DNA used and the size of the NP. Based on this and the ratio between the biotinylated hairpin-DNA and the non-biotinylated blocking-DNA in the solution, we can estimate the amount of hairpin-DNAs to be roughly 20 per particle in the case of 0.1% hairpin sample and about two in the lowest tested hairpin-DNA portion of 0.01%.

Although the hydrodynamic diameter of the particle is related to the biotin density on the particle surface, it does not necessarily correlate with the binding efficiency between biotin–AuNP and avidins. To further characterize this and to verify our estimation of the amount of biotinylated DNA per NP, the hairpin-DNA–AuNP was tested for its capability to cluster with avidins in solution (see the Experimental section). It is expected that the average hydrodynamic diameter of the particle or particle-cluster in the formed avidin–AuNP mixture would increase with the number of biotinylated DNAs at the surface of AuNP due to a higher probability of particle clustering. To analyze this, we calculated the relative increase in the hydrodynamic diameter $D_{rel} = (D_{final} - D_{ini})/D_{ini}$, where D_{final} and D_{ini} are the hydrodynamic diameters after and before the mixing of the biotin–AuNPs with avidin (Fig. 2a).

The same mixing ratios were used during the functionalization process. The relative increase in D_{rel} and thus the amount of aggregation has a peak at the ratio 1 : 1 and starts to decrease on increasing the amount of blocking-DNA as shown in Fig. 2b. This is due to the decrease in the number of the biotins and thus avidin binding points on the particle surface. On the other hand, the decrease in the apparent hydrodynamic radius observed when reducing the amount of blocking-DNA from the 1 : 1 ratio can be due to an insufficient avidin to biotin–AuNP ratio or because too high surface

density of biotin does not support efficient avidin–biotin binding.⁴⁴ Interestingly, we observed that AuNPs without any biotin, *i.e.*, coated with only blocking-DNA, had the same 20% increase in the hydrodynamic diameter after mixing with avidin as compared to the control AuNPs without any DNA. This might be due to non-specific binding of avidin on AuNP or bulk effects. Yet, the hairpin-DNA samples with only 0.1% of biotinylated hairpin-DNA (ratio 1 : 999) showed a still higher increase in hydrodynamic radius after the addition of avidin (30%) compared to the control sample (20%). Assuming that the 0.1% hairpin-DNA sample does not form particle–particle dimers and that the 20% increase is due to the bulk effects, then the increase from 20% to 30% would roughly correspond to the size of addition of one avidin layer (see ESI† for more details).

The aggregation process was greatly diminished when lowering the amount of hairpin-DNA down to 0.1%, and vanished totally with 0.01% concentration. This agrees very well with the above estimation, especially when taking into account that the hairpin-DNA is longer than the blocking-DNA, and thus slower in diffusion, which most probably lowers its contribution within the attached DNA compared to the concentration ratio in solution. Since the aggregation process was significantly reduced but still happening at the 1 : 999 ratio, we used this ratio to fabricate all biotin–AuNPs (ssDNA: 3 nm, 8 nm and 15 nm, and hairpin-DNA) for the electric field manipulation studies.

Numerical calculation of the LSPR spectra of the DNA–AuNP–nanoactuator

As mentioned above, we utilized the optical properties of the AuNP to track its position above the gold surface; the LSPR scattering spectra of AuNP are very sensitive to the distance between the nanoparticle and the surface. We used the Finite Element method (FEM) (Comsol Multiphysics version 5.1) to solve the LSPR spectra of the AuNP–Au-surface coupled system as a function of the distance d (Fig. 3). The scattering spectra for transverse electric (TE) and transverse magnetic (TM) polarized light in Fig. 3d–f show that the main LSPR peak shifts from 570 nm to 660 nm as the distance d decreases from 20 nm to 1 nm. There is also a secondary peak appearing around 550 nm when the particle-to-surface distance is 5 nm or less. Similar behavior has been reported in the literature,^{22,28,45,46} and it can be interpreted as an interaction between the real particle and a conduction surface-induced mirror particle. The main LSPR peak, which redshifts as the particle is brought closer to the surface, corresponds to the parallel dipole–dipole interaction between the real particle and the mirror particle. The secondary peak corresponds to in-plane dipole–dipole interaction. Both the in-plane and parallel dipole–dipole excitations create high electric fields that are confined within the gap between the particle and the surface (Fig. 3b and c and S14†). Fig. 3f shows the LSPR scattering peak position dependency on the distance d for both TE and TM polarized light.⁴⁷ Since we are probing with unpolarized light, the position of the AuNP is correlated to the average

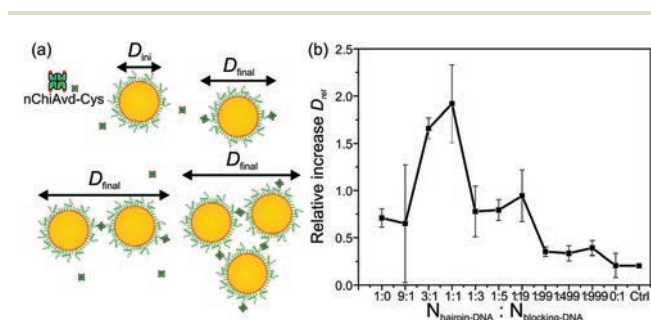


Fig. 2 Clustering of biotin–AuNPs with different ratios of hairpin-DNA and blocking-DNA in the presence of avidin. (a) A schematic view of the avidin–biotin–AuNP aggregation process. After mixing the biotin–AuNPs with chimeric avidin, the average size of the species increases due to the aggregation, which can be seen as an increased hydrodynamic diameter D_{final} compared to the initial hydrodynamic diameter D_{ini} . (b) The relative increase of the hydrodynamic diameter D_{rel} versus the hairpin-DNA : blocking-DNA ratio. Ctrl means control AuNPs without any DNA.

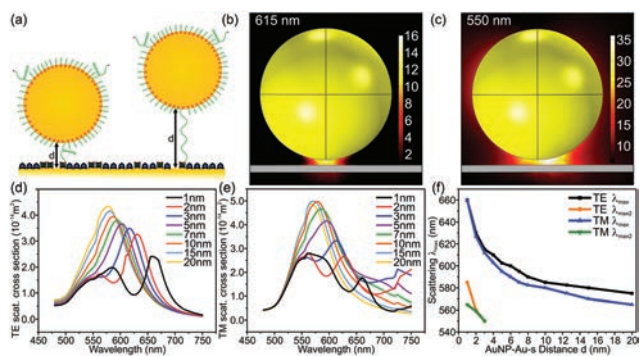


Fig. 3 Numerical simulation data of an 80 nm gold nanoparticle coupled to the gold surface. (a) A schematic view of the simulated system. The distance d between the particle and the gold surface is varied from 1 nm to 20 nm and the scattering cross section of the TM and TE polarized excitation is calculated numerically. (b) The field enhancement of the AuNP–Au-surface system at 615 nm (TM polarization), when d is 3 nm. The field is highly confined between the surface and the particle. (c) The field enhancement of the AuNP–Au-surface system at 550 nm (TM polarization), when d is 3 nm. The field is mostly confined to the gap but is more spatially distributed as compared to the system excited using a longer wavelength (b). (d, e) The simulated TE and TM scattering cross-section of the AuNP–Au-surface system, when the distance is changed from 1 nm to 20 nm. (f) The scattering cross-section wavelength maximum *versus* the distance d , where the LSPR scattering peak redshifts as the particle is brought closer to the Au-surface. There is also a secondary peak appearing when the particle–surface distance is exceeding 4 nm, which can be seen in fig. (d) and (e).

LSPR peak position of the two polarizations, which will be further correlated to the motion of the actuator and then to the stretching of the DNA.

Manipulation of DNA–AuNP nanoactuators by an electric field

To implement all the above-mentioned findings for the functionality studies of ready DNA–AuNP-nanoactuators, we built an experimental setup where we can observe nanoparticles on a gold surface within a liquid environment by using *in situ* dark field microscopy, while applying a voltage to create an electric field within the liquid medium. Moreover, liquids can be pumped in and out of the measurement flow chamber during the experiments to deliver studied assemblies as a suspension or to change the buffer conditions, *e.g.*, pH, amount of salts or temperature. This liquid flow holder was designed so that the chip with the active Au-surface could be fixed on the bottom and the chamber can be sealed using an ITO glass on top. The holder contains electric contacts for both the ITO and the Au-surface for applying the electric field. See ESI† for more details of the setup.

The fabrication of the DNA–AuNP-nanoactuators was carried out similarly to the RA-SPR measurements above (ESI Fig. S5†): after a hydrophilic treatment, the gold-coated Si chip was glued into the contact of the holder using silver paste and varnish. The resistance between the outside contacts and the Au-surface was measured to ensure good electrical contact ($R \sim 10\text{--}250 \Omega$). The avidin and BSA solutions were prepared similarly to the SPR measurement, but the solution was incubated

on the Au-surface instead of injection. The avidin solution was first applied on the surface for 30 min, followed by a washing step using PBS buffer and a subsequent incubation of BSA for 30 min. After protein deposition, the sample was cleaned by injecting 50 μl of 0.1 mM NaPhos and 1 mM NaCl buffer (pH 7.6, NaPo–NaCl) and the chamber was sealed using ITO coated glass by connecting two opposite sides of the ITO glass to upper contacts in the holder. Again, the resistance from the external contact to the floating side of the ITO was measured to ensure good contacts ($R \sim 8\text{--}50 \Omega$). The input and output fluid channels of the holder were pre-wetted using NaPo–NaCl and the holder was placed under an optical microscope. Typical immobilization of the biotin–AuNPs consisted of pumping of the biotin–AuNP solution into the chamber, waiting for 15 to 90 min for biotin–AuNPs to immobilize and the subsequent flushing of the non-bound biotin–AuNPs using NaPo–NaCl.

The nanoactuator motion was studied both statistically on a large scale and by monitoring individual actuators. The individual actuators were studied by recording the LSPR scattering spectra of a single particle with dark field microscopy while applying an electric field. However, this scheme could not be scaled up due to the serial nature of the measurements. Instead, we used a camera to take optical dark field images containing a large ensemble of actuators and analyzed the color (wavelength) changes of the particles *via* the RGB data. The large-scale behavior was analyzed to evaluate the percentage of controllable actuators, *i.e.* the fabrication yield, and to observe the collective motion of the system, which gives insight into the folding properties of the biomolecule. On the other hand, the individual measurements can be used to directly evaluate the optical properties of the system, *i.e.*, the LSPR peak position and how accurately it can be controlled, which is important when considering applications in, *e.g.*, SERS or fluorescence enhancement.

The large-scale measurements were performed by sweeping the bias voltage from negative to positive voltages in constant steps (see the Methods section). After each voltage change and subsequent 1 min stabilization, an optical image of the sample was recorded. After the measurements, the optical images were processed using the Image-J program to extract the RGB data of the biotin–AuNPs with respect to the bias voltage (see ESI†). The RGB data were further converted into the corresponding hue, saturation and value (HSV) numbers (see ESI†). The HSV representation was selected, since the visible spectra can be represented in different hue values from 0° to 360° in a convenient linear scale. The issue here is that the hue values cannot be directly related to the maximum wavelength of the LSPR scattering spectra and thus to the position of the AuNP. To overcome this, we calibrated the system by measuring both the LSPR spectra and the corresponding RGB (HSV) values from several AuNPs without an applied electric field (see ESI†). The hue *versus* LSPR peak wavelength was plotted for calibration, and, in particular, we estimated the shift in hue value corresponding to particle movement from the close vicinity of the surface (distance 5 nm or less in Fig. 3)

to a position distal to the surface (distance ~ 20 nm in Fig. 3 and S9, see ESI† for more details). The distance of 5 nm was selected, since this would correspond to the thickness of the chimeric avidin and the passivation layer, and most probably the particle would not penetrate this layer. A minimum shift in hue for a significant movement was found to be around 40° , and for any further processing, we selected only those particles that had at least once a Hue shift of 40° or more, when the direction of the voltage was switched several times.

Demonstration of the nanoactuator operation by ssDNA

To demonstrate the controllable behavior, we first analyzed nanoactuators assembled with different ssDNAs of varying lengths, *i.e.*, DNA-s3nm, DNA-s8nm and DNA-s15nm. As described above, we analyzed the behavior of each particle under an electric field from the optical images to evaluate the degree of its controllability. Most of the particles that had at least a 40° shift in the hue could be categorized roughly into four groups (Fig. 4 and S10†): the particles which could be pushed away with negative E-field and pulled towards the gold surface with positive E-field (group 1, orange histograms, 4.6–8.9% of AuNPs); particles which had opposite behavior compared to group 1 (group 2, blue histograms, 0.2–5.2%); particles which eventually got stuck far away from the surface (group 3, purple histograms, 1.8–3.8%) and particles which eventually got stuck close to the surface (group 4, green histograms, 0.4–2.1%). The black histograms of the last column illustrate the data measured for all particles, *i.e.*, all the groups together.

The difference between group 1 and group 2 can be at least partially attributed to the charge distribution of the particles. We characterized the zeta-potential of the different biotin–AuNPs, which showed that most of the samples had a large portion of negatively charged particles (94.2–99.1%) and a small portion of positively charged particles (0.9–5.8%), which would indicate that negative particles contribute to group 1 and positive particles to group 2 (see ESI Fig. S3 and Table S2†). Also, the surface charge and double-layer induced by the electric field can affect the behavior of the AuNPs. Overall, the interaction of AuNPs and different charges in the system leaves a lot of room for interpretation and further studies would be required to fully assess the situation.

Fig. 4a shows the results of the analysis for the AuNP-s15nm sample. For the particles of group 1 (56 particles, orange) the hue (H) values form a Gaussian distribution which shifts continuously to higher values with negative voltage and is pulled back towards 0° with positive voltage. We also observed similar behavior for particles with 8 nm spacers (see ESI†), but the AuNP-s3nm sample had particles located closer to the surface due to the shorter linker and the shifts in the histogram position were negligible (Fig. S10†). For AuNP-s8nm we observed a number of particles belonging to group 2, but only a few were observed for the sample s15nm. As discussed above, this can be due to the varying charge of the functionalized gold particles in the s8nm, while in s15nm samples the longer DNA guarantees negative charge. This is further verified

by the large number of s15nm particles in group 3 compared to group 4 (Fig. 4a).

Overall, it is evident that in many cases the particles are moving initially with the electric field, but eventually stop responding (Fig. 4, S10b and S13,† groups 3 and 4). Even in the case of the AuNP-s8nm, the collective motion of the particle seems to have continuous flow with the shape of the Gaussian distribution as in the AuNP-s15nm sample, which would be expected for a nanoactuator anchored *via* a string with thermal fluctuations. However, the behavior degrades with the increasing number of voltage switches. The sensitivity of the nanoactuator behavior on a successful linking is well demonstrated by the fact that most of the particles are unmovable and are located near the surface (Fig. S11†). For this reason, the chosen threshold for analysis, *i.e.*, the minimum of 40° shift in the H value, was indeed necessary. Here it should be emphasized that the histograms illustrate overall collective motions of the particles, which have similar behavior at some point during the measurements.

Applying the nanoactuator to study the hairpin-DNA

Finally, we utilized the DNA–AuNP-nanoactuator to study the conformation of the hairpin-DNA. The overall results resemble greatly the above case of plain ssDNA. However, even though the particles have a specific behavior under the electric field, allowing also the division to the four groups, the motion of the hairpin-DNA–AuNPs seems to fluctuate mostly between two distinct values (dotted and dashed vertical lines in Fig. 4b) as the voltage is swept. It is clear from the simulations and H, λ -calibration that these values correspond to the situations where the particle is close to the surface and far away from the surface. As seen in the RA-SPR measurements, without any electric field the hairpin-AuNP is close to the surface, *i.e.*, the hairpin-DNA is in a folded state as shown in Fig. 4c. Applying a high enough electric field leads to the opening of the hairpin by straightening the DNA-strands (Fig. 4d and e). But when pulling the particle back to the surface, the hairpin can relax and folds back (Fig. 4f), and thus we mainly observe quantized fluctuations of the particle position. On the other hand, because we always see particles with both positions, it could be that thermally driven hybridizations and openings of the hairpin happen all the time and we only affect the balance between these two states by applying the electric field.

The controllability of the nanoactuator for both the hairpin-DNA and the ssDNAs was assessed based on the percentage of particles in the groups showing systematic behavior under an electric field, *i.e.*, group 1 and group 2 (Table 1) compared to all of the immobilized particles (no threshold for H value). Combining the two groups, the percentage of controllable particles was about 12% for the hairpin-DNA and 4.6 to 17% in the case of the ssDNA samples. The overall RGB data of all the immobilized particles for all of the samples in Fig. S11† show that most of the particles are located near the surface ($H \approx 0^\circ$) during the measurements, which suggests that the particles, even after the minimization of the number of biotins, are still

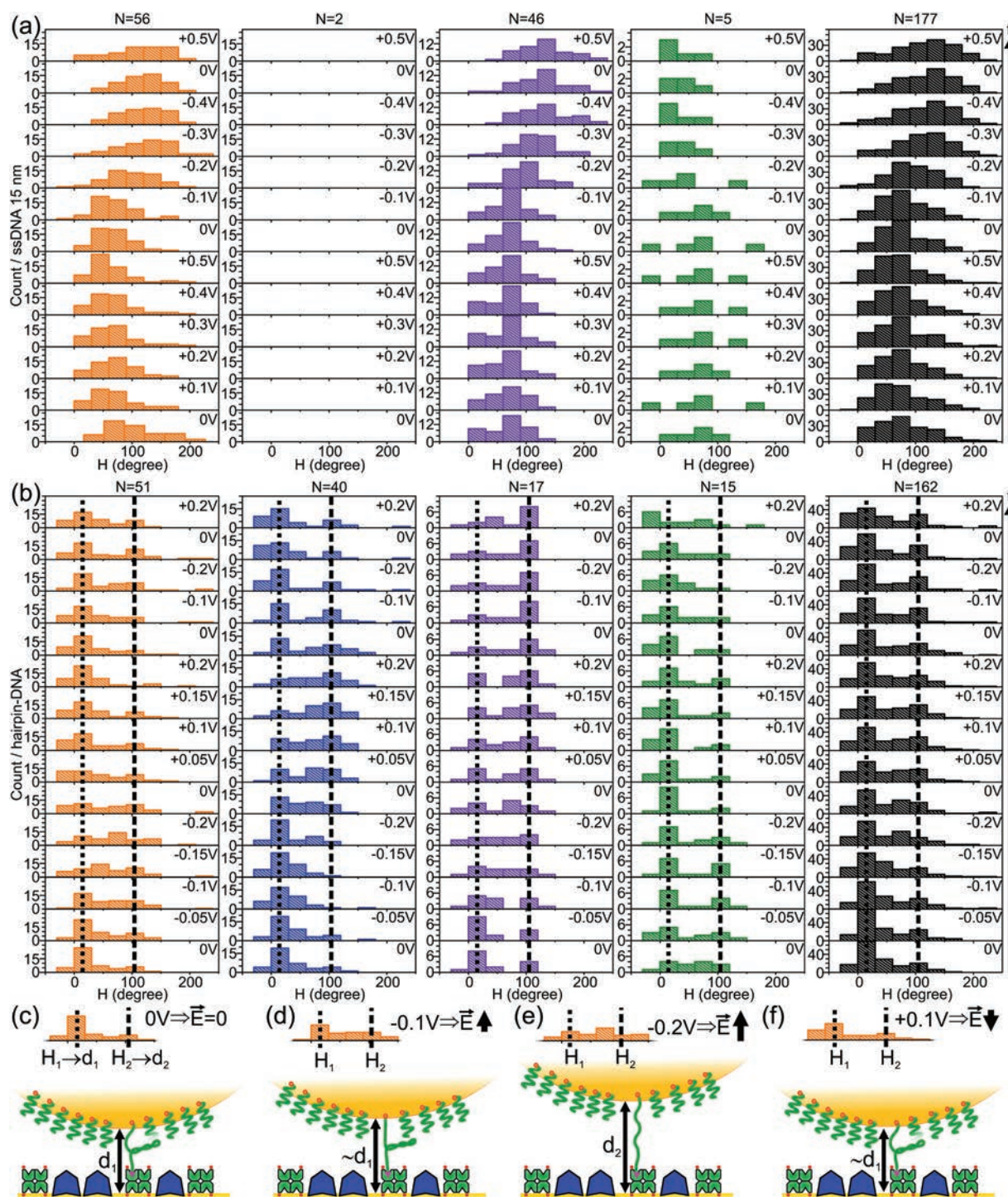


Fig. 4 The histogram data of the color changes of AuNPs bound to the avidin-coated gold surface *via* biotinylated DNAs. (a) The histogram data of AuNPs conjugated with 0.1% of biotinylated 15 nm spacer DNA and passivating DNA. The numbers above the histograms indicate the number of analyzed particles. The orange histograms show particles that move away from the surface with a negative electric field. The blue histograms represent a group of particles that behave opposite to particles in the orange histograms. The violet histograms show particles that slowly move away from the surface and the green histograms show particles that are stuck close to the surface. The black histograms show data of all of the analyzed particles. (b) Similar histogram data as in (a), but for AuNPs with 0.1% of hairpin-DNA and blocking DNA. (c)–(f) Schematic illustration of the opening and folding of the hairpin-DNA, where the hairpin is initially folded when no external electric field is applied. The histogram data in panels (c)–(f) depict the first ($V = 0$ V), third ($V = -0.1$ V), fifth ($V = -0.2$ V) and eighth ($V = +0.1$ V) histograms starting from the bottom in the panel (b). When only a small electric field \vec{E} is applied, the hairpin stays closed and the particle is located close to the surface ($d \approx d_1 \rightarrow H_1$, indicated by the dotted line). By applying a high enough field \vec{E} , the hairpin can be opened and the particle is pushed far away from the surface ($d = d_2 \rightarrow H_2$, indicated by the dashed line). When the particle is pulled towards the surface and let to relax ($d \approx d_1$), the hairpin can fold back.

Table 1 The assessment of the controllability of the DNA–AuNP-nanoactuator

Sample	Fraction in group 1 (%)	Fraction in group 2 (%)
Hairpin-DNA	6.6	5.2
DNA-s15 nm	4.6	0.2
DNA-s8 nm	8.9	8.1

bound to the surface too strongly to be displaced by an electric field.

To further test the possible enhancing effect of even more reduced densities of avidin and biotin, we fabricated samples with only about one or two avidins within the area covered by a single AuNP, to prevent binding *via* multiple avidin–biotin links. These tests confirm the above conclusion that non-specific binding is the most significant factor lowering the yield of the nanoactuator assembly (see ESI†). Lowering the avidin density makes the formation of proper avidin–biotin binding slower and thus the non-specific binding has more time to happen during the AuNP deposition. Thus, with the lowest avidin density there appear to be almost only non-specifically bound particles. On the other hand, the reduction of the biotinylated hairpin-DNA to 0.01% did not produce enough binding ability, as was noticed also in the aggregation tests (discussed above), and virtually all the particles were non-specifically bound. This also indicates that most of the non-functional particles correspond to the non-specifically bound particles.

Study of individual hairpin-DNA–AuNP nanoactuators

Selected hairpin-DNA–AuNPs, which seemed to be moving freely in the large-scale measurements, were subjected for the individual particle measurements. The voltage-dependent LSPR scattering spectra were measured for several movable AuNPs (Fig. 5, S12 and S13†). Fig. 5a and b show spectra of Particle A and Particle B with 0.1% hairpin-DNA, respectively, whereas the particles C and D in Fig. 5c and d have the hairpin-DNA covering the whole particle. As the voltage was swept, it was typically observed that pure hairpin-DNA particles required ± 3 V ($\bar{E} \approx 3.5 \times 10^4$ V m⁻¹) to move, while particles with 0.1% hairpin-DNA needed only ± 0.5 V ($\bar{E} \approx 0.6 \times 10^4$ V m⁻¹). This observation is reasonable, since AuNPs with a larger amount of biotin–DNA likely form more bonds with the avidin-coated surface and, consequently, there are more connecting DNA hairpins to resist the stretching movement. The LSPR scattering spectra changes can be also seen as color changes in the dark field images, as shown in Fig. 5e (negative voltage) and f (positive voltage) for particle A and for particle B in Fig. 5g (negative voltage) and h (positive voltage).

Interestingly, the main LSPR peak positions for particles A and B are typically around 567–585 nm when they are pushed away from the surface by a negative field and the peak shifts to 600–640 nm when pulled by a positive voltage. Based on the FEM-simulations (see Fig. 3f), these peaks would correspond to distances 18 nm (570 nm peak) and 2–5 nm (620 nm peak)

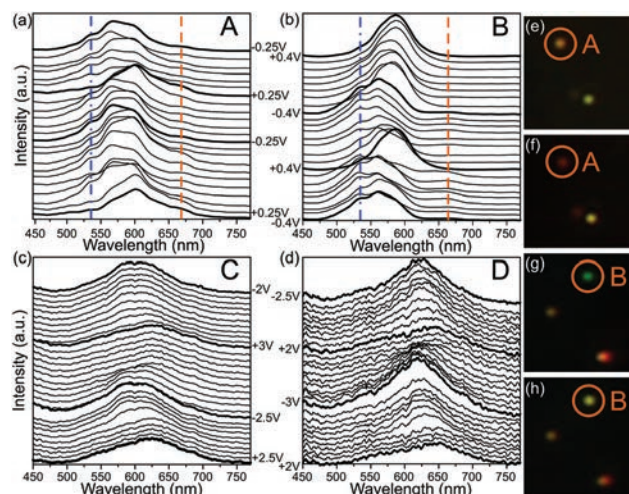


Fig. 5 The LSPR scattering spectra of individual AuNPs bound to the avidin-coated Au-surface *via* biotinylated hairpin-DNAs. (a–d) The LSPR spectra of particles A–D. Particles A and B are coated with a mixture of 0.1% biotin–DNA and 99.9% blocking-DNA, while C and D are coated with biotin–DNA alone. The secondary peaks at 535 nm (blue dash-dot line) and 660 nm (orange dashed line) in figures (a) and (b) are associated with particle position close to the surface, and they are missing in figures (c) and (d). (e, f) Dark field images of particle A under either negative (e) or positive (f) electric field with respect to the gold substrate. (g, h) Dark field images of particle B under either negative (g) or positive (h) electric field with respect to the gold substrate.

above the Au-surface. However, there are also peaks at 535 nm and 660 nm as shown in Fig. 5a and b (blue dot-dashed lines and orange dashed), when the particle is pushed with negative voltage, but, based on the FEM-simulations, these peaks should only be present when the particle is very close to the Au-surface. This indicates that despite the surface passivation, AuNPs still have a possibility to push themselves close to surface between the passivating molecules.

Since the exposure time is relatively long (3 s) and while pushing AuNP away with negative voltage, both the close proximity peaks (530 nm and 660 nm) and the far away peak (580 nm) are present (still the 580 nm peak being the largest), we probably see an average position of the particles A and B with respect to the Au-surface. Seeing this kind of combined spectrum for a single AuNP indicates that the particles are constantly moving up and down in relation to the surface. However, since the observed spectrum is clearly a sum of mainly two particle positions (close proximity and far away), instead of a combination of spectra of all the possible positions, we can deduce that these two positions are the most pronounced ones. This agrees well with the above conclusion of a constant thermally driven hybridization and opening of the hairpin. For some particles, we predominantly only see the 530 nm and the 660 nm peaks, indicating that they are stuck in the vicinity of the surface (Fig. S12c†).

Particles C and D with a larger amount of biotin did not show similar behavior, but they rather showed rigid and better-defined motion of the LSPR peak without fluctuations.

The peak positions for particles C and D are moving between 590 nm and 623 nm and between 620 nm and 643 nm, respectively, when pushed away and pulled towards the surface. For particle C, this would correspond to a motion where a particle is stretched 7 nm and then brought back to a distance of 2.5 nm, which is a bit less than the height of the chimeric avidin. For particle D, the motion would be between 3 nm and 1 nm. These results have several consequences; on the one hand, it is vital to minimize the amount of avidin and passivate the surface, if one wants to achieve full particle motion and the best sensitivity. Increasing the amount of biotin on the surface of AuNPs would mean rigid, well-defined motion, which could be desirable for actuator applications.

Conclusions

In summary, we have fabricated and characterized a DNA and AuNP based nanoactuator utilizing particle–substrate distance dependent plasmonic coupling, and used this nanoactuator for molecular studies under an applied electric field. First, the functionalization of AuNP with different biotinylated DNA strands was carried out using established protocols. We minimized the amount of biotin groups on the AuNP surface by mixing the biotinylated-DNA and a blocking-DNA in a very low ratio of 1:999, which was still enough to cause significant affinity between avidin and biotin–AuNPs as shown by the DLS analysis. We demonstrated using RA-SPR and dark field microscopy that these biotinylated AuNPs can be immobilized selectively to a gold surface functionalized with chimeric avidin and passivated with thiolated PEG or BSA. However, in SPR experiments, the biotin–AuNP binding to the chimeric avidin was not straightforward to show, since the SPR signal shift was typically weak, most probably due to the coupling between the laser-excited surface plasmon polaritons and the LSPR of the gold nanoparticles.

The nanoactuator scheme was used to analyze the motion and dynamics of the hairpin-DNA with respect to the ssDNAs with varying lengths under the influence of the electric field. It was discovered that the ssDNA samples had continuous flow on and off the surface, whereas the hairpin-DNA had a more quantized motion, which is the result of opening and folding of the hairpin-DNA. When analyzing the behavior of the ssDNAs and hairpin-DNA under the E-field, roughly 14–29% of the bound particles did change color during the measurements at least once, and overall 5–17% of the bound particles could be controlled for an extended period. This indicates that even though the number of biotins on AuNPs was optimized, the majority of biotin–AuNPs have still too high affinity towards the avidins on the surface or are bound only non-specifically. To improve the former case, we reduced the density of avidin on the surface and the amount of the biotin–DNAs on the AuNP. It was observed that the reduction of either component can be done only to a certain extent, since the immobilization time of biotin–AuNP increases significantly, which shows as an increased number of non-specifically

bound AuNPs. This indicates that the non-specific binding is the most significant factor lowering the yield of the nanoactuator assembly, and that most of the non-functional particles are not properly assembled actuators, but only non-specifically surface-attached particles, which can be excluded from the analysis.

We were also able to characterize the movement of individual biotinylated hairpin-DNA–AuNPs under electric field manipulation. These studies reveal that the individual particles can have different behaviors under E-field, most probably depending on the amount of attachment points between the Au-surface coated with avidins and the particle containing biotinylated DNA. A small amount of biotins resulted in a situation where the particle's LSPR peak could be moved freely between 565 nm and 640 nm, which corresponds to the situations where hairpin-DNA is fully stretched or the particle is touching the chimeric avidin layer, respectively. Notably, the avidin layer (theoretical thickness of ~3–5 nm) may somewhat limit the sensitivity, which increases significantly when the particle is closer than 5 nm as shown in the simulations. For an optimal system, the avidin layer and the surface passivation could be further tuned, so that the particle would be capable of getting closer to the sample surface but still not to get stuck on it. Some kind of nanopatterned surface could be of value here.

Also, when the biotin amount was lowered, the position of the particles seemed to fluctuate on and off the surface when pushed away with an electric field. Most probably, this was due to thermal motion. When there were larger amounts of biotins per particle, the particles had more rigid motion with no secondary LSPR peak, meaning that the particles firmly attached to the gold surface. These together with the fact that the higher biotinylation density required larger voltages to see any shifts suggests that controlling the amount of biotins on the AuNP surface is a key factor to enable free motion of the AuNP under the influence of the electric field. Based on these results we can conclude that the DNA–AuNP system offers a promising platform for a reversible E-field controlled nano-scale molecular actuator.

Conflicts of interest

There are no conflicts to declare.

Acknowledgements

This work was financially supported by the Academy of Finland through projects 263526, 130900, and 283011 (for J. J. T.), 263540 and 290506 (for V. P. H.) and 263523 (for M. A.). K. T. received funding from Finnish Cultural Foundation. We thank BioNavis for equipment and essential expertise in the SPR analysis and Stephan Block (Freie Universität, Berlin, Germany) for fruitful discussions and advice.

Notes and references

- 1 B. Van Dorst, J. Mehta, K. Bekaert, E. Rouah-Martin, W. De Coen, P. Dubruel, R. Blust and J. Robbens, *Biosens. Bioelectron.*, 2010, **26**, 1178.
- 2 A. S. Ansari and Q. Husain, *Biotechnol. Adv.*, 2012, **30**, 512.
- 3 B. Pérez-López and A. Merkoçi, *Trends Food Sci. Technol.*, 2011, **22**, 625.
- 4 K.-I. Chen, B.-R. Li and Y.-T. Chen, *Nano Today*, 2011, **6**, 131.
- 5 M. Pilo-Pais, A. Watson, S. Demers, T. H. LaBean and G. Finkelstein, *Nano Lett.*, 2014, **14**, 2099.
- 6 J. W. Naughton and M. Sheplak, *Prog. Aeronaut. Sci.*, 2002, **38**, 515.
- 7 K. Fu, S. Chen, J. Zhao and B. G. Willis, *ACS Sens.*, 2016, **1**, 444.
- 8 Y. Ke, T. Meyer, W. M. Shih and G. Bellot, *Nat. Commun.*, 2016, **7**, 10935.
- 9 H. Gu, W. Yang and N. C. Seeman, *J. Am. Chem. Soc.*, 2010, **132**, 4352.
- 10 R. Elghanian, J. J. Storhoff, R. C. Mucic, R. L. Letsinger and C. A. Mirkin, *Science*, 1997, **277**, 1078.
- 11 S. Block, B. J. Fast, A. Lundgren, V. P. Zhdanov and F. Höök, *Nat. Commun.*, 2016, **7**, 12956.
- 12 M. Banchelli, S. Nappini, C. Montis, M. Bonini, P. Canton, D. Berti and P. Baglioni, *Phys. Chem. Chem. Phys.*, 2014, **16**, 10023.
- 13 C. Jiang, M. E. McConney, S. Singamanemi, E. Merrick, Y. Chen, J. Zhao, L. Zhang and V. V. Tsukruk, *Chem. Mater.*, 2006, **18**, 2632.
- 14 K. Tapio, J. Leppiniemi, B. Shen, V. P. Hytönen, W. Fritzsche and J. J. Toppari, *Nano Lett.*, 2016, **16**, 6780.
- 15 A. V. Pinheiro, D. Han, W. M. Shih and H. Yan, *Nat. Nanotechnol.*, 2011, **6**, 763.
- 16 S. R. Paludan and A. G. Bowie, *Immunity*, 2013, **38**, 870.
- 17 M. Zahid, B. Kim, R. Hussain, R. Amin and S. H. Park, *Nanoscale Res. Lett.*, 2013, **8**, 119.
- 18 K. E. Dunn, M. A. Trefzer, S. Johnson and A. M. Tyrrell, *Sci. Rep.*, 2016, **6**, 29581.
- 19 K. Lund, A. J. Manzo, N. Dabby, N. Michelotti, A. Johnson-Buck, J. Nangreave, S. Taylor, R. Pei, M. N. Stojanovic, N. G. Walter, E. Winfree and H. Yan, *Nature*, 2010, **465**, 206.
- 20 P. A. Rasheed and N. Sandhyarani, *Microchim. Acta*, 2017, **184**, 981.
- 21 K. A. Willets and R. P. V. Duyne, *Annu. Rev. Phys. Chem.*, 2007, **58**, 267.
- 22 J. J. Mock, R. T. Hill, A. Degiron, S. Zauscher, A. Chilkoti and D. R. Smith, *Nano Lett.*, 2008, **8**, 2245.
- 23 F. Cannone, G. Chirico, A. R. Bizzarri and S. Cannistraro, *J. Phys. Chem. B*, 2006, **110**, 16491.
- 24 A. W. M. Haining, M. von Essen, S. J. Attwood, V. P. Hytönen and A. d. R. Hernández, *ACS Nano*, 2016, **10**, 6648.
- 25 F. Margadant, L. L. Chew, X. Hu, H. Yu, N. Bate, X. Zhang and M. Sheetz, *PLoS Biol.*, 2011, **9**, e1001223.
- 26 R. J. Russell, P. S. Kerry, D. J. Stevens, D. A. Steinhauer, S. R. Martin, S. J. Gamblin and J. J. Skehel, *Proc. Natl. Acad. Sci. U. S. A.*, 2008, **105**, 17736.
- 27 S.-Y. Chen, J. J. Mock, R. T. Hill, A. Chilkoti, D. R. Smith and A. A. Lazarides, *ACS Nano*, 2010, **11**, 6535.
- 28 M. W. Knight, Y. Wu, J. B. Lassiter, P. Nordlander and N. J. Halas, *Nano Lett.*, 2009, **9**, 2188.
- 29 C. Lumdee, S. Toroghi and P. G. Kik, *ACS Nano*, 2012, **6**, 6301.
- 30 C. L. Du, Y. M. You, K. Johnson, H. L. Hu, X. J. Zhang and Z. X. Shen, *Plasmonics*, 2010, **5**, 105.
- 31 I. Vikhold-Lundin, S. Auer, M. Paakkunainen, J. A. E. Määttä, T. Munter, J. Leppiniemi, V. P. Hytönen and K. Tappura, *Sens. Actuators, B*, 2012, **171–172**, 440.
- 32 J. J. Storhoff, R. Elghanian, R. C. Mucic, C. A. Mirkin and R. L. Letsinger, *J. Am. Chem. Soc.*, 1998, **120**, 1959.
- 33 C. A. Mirkin, R. L. Letsinger, R. C. Mucic and J. J. Storhoff, *Nature*, 1996, **382**, 607.
- 34 H. Liang, J.-P. Tuppurainen, J. Lehtinen, T. Viitala and M. Yliperttula, *Eur. J. Pharm. Sci.*, 2013, **50**, 492.
- 35 K. Niegelhell, S. Leimgruber, T. Grieser, C. Brandl, B. Chernev, R. Schennach, G. Trimmel and S. Spirk, *Langmuir*, 2016, **32**, 1550.
- 36 J. He, M. Lu, X. Zhou, J. R. Cao, K. L. Wang, L. S. Liao, Z. B. Deng, X. M. Ding, X. Y. Hou and S. T. Lee, *Thin Solid Films*, 2000, **363**, 240.
- 37 N. M. Green, *Adv. Protein Chem.*, 1975, **295**, 85.
- 38 N. M. Green, *Methods Enzymol.*, 1990, **184**, 51.
- 39 Y. Uchiho, M. Shimojo, K. Furuya and K. Kajikawa, *J. Phys. Chem. C*, 2010, **114**, 4816.
- 40 T. Akimoto, S. Sasaki, K. Ikebukuro and I. Karube, *Biosens. Bioelectron.*, 2000, **15**, 355.
- 41 X. Hong and E. A. H. Hall, *Analyst*, 2012, **137**, 4712.
- 42 A. Lundgren, B. Agnarsson, R. Zirbs, V. P. Zhdanov, E. Reimhult and F. Höök, *ACS Nano*, 2016, **10**, 9974.
- 43 S. J. Hurst, A. K. Lytton-Jean and C. A. Mirkin, *Anal. Chem.*, 2006, **78**, 8313.
- 44 K. K. Caswell, J. N. Wilson, U. H. F. Bunz and C. J. Murphy, *J. Am. Chem. Soc.*, 2003, **125**, 13914.
- 45 A. Dathe, M. Ziegler, U. Hübner, W. Fritzsche and O. Stranik, *Nano Lett.*, 2016, **16**, 5728.
- 46 C. Lumdee, B. Yun and P. G. Kik, *ACS Photonics*, 2014, **1**, 1224.
- 47 J. D. Driskell, R. J. Lipert and M. D. Porter, *J. Phys. Chem. B*, 2006, **110**, 17444.

